NUMERICAL SIMULATIONS OF GIANT VESICLES IN MORE COMPLEX STOKES FLOWS AND DISCRETIZATION CONSIDERATIONS OF THE BOUNDARY ELEMENT METHOD

by

Charlie Lin

A Dissertation

Submitted to the Faculty of Purdue University

In Partial Fulfillment of the Requirements for the degree of

Doctor of Philosophy

Davidson School of Chemical Engineering

West Lafayette, Indiana

May 2022

THE PURDUE UNIVERSITY GRADUATE SCHOOL
STATEMENT OF COMMITTEE APPROVAL

Dr. Vivek Narsimhan, Chair

Davidson School of Chemical Engineering

Dr. Sangtae Kim

Davidson School of Chemical Engineering

Dr. Osman Basaran

Davidson School of Chemical Engineering

Dr. Hector Gomez

School of Mechanical Engineering

Approved by:

Dr. John Morgan

ACKNOWLEDGMENTS

I would like to thank my advisor, Vivek, who spent many days alongside me designing, redesigning, and troubleshooting my research projects throughout the years. His enthusiasm for physics and prowess in analytical thinking always motivated me even when I was stuck on a problem for weeks on end. As Vivek would put it, we may go through many serpentine or unfruitful paths in research but we will always learn a lot in the process. I would like to thank the members of the committee: Dr. Sangtae Kim, Dr. Osman Basaran, and Dr. Hector Gomez for their suggestions on this work. Additionally, I thank all of my peers from the Purdue PhD program; it has been helpful to bounce off ideas with each other or at least commiserate together.

My parents, Li Lin and Sandy Yuan, have helped me in countless ways throughout my time through the program. Thank you two for the providing the support and stability required for me to complete my PhD. I thank my brother, Danny Lin, for reaching out and sharing new interests with me; effectively pulling my mind out of the anxiety tied to completing a PhD. I also thank the rest of my family for their support throughout. Finally I would like to thank my friends who are scattered across the world but still somehow meet up often enough to play a game or two.

TABLE OF CONTENTS

LIST OF TABLES

LIST OF FIGURES

8

11

ABSTRACT

Quantifying the dynamics and rheology of soft biological suspensions such as red blood cells, vesicles, or capsules is paramount to many biomedical and computational applications. These systems are multiphase flows that can contain a diverse set of deformable cells and rigid bodies with complex wall geometries. For this thesis, we are performing several numerical simulations using boundary element methods (BEM) for biological suspensions in biomedically relevant conditions. Each simulation is devised to answer fundamental questions in modeling these systems.

Part of this thesis centers around the fluid mechanics of giant unilamellar vesicles (GUVs), fluid droplets surrounded by a phospholipid bilayer. GUVs are important to study because they mimic the dynamics of anuclear cells and are commonly used as a basis for artificial cells. The dynamics of vesicles in simple shear or extensional flows have been extensively studied. However the conditions seen in microfluidic devices or industrial processing are not always described by steady shear or extensional flows alone, and require more investigation. In our first study, we investigate the shape stability of osmotically deflated vesicles in a general linear flow (i.e., linear combinations of extensional and rotational flows). We modeled the vesicles as a droplet with an incompressible interface with a bending resistance. We simulated a range of flow types from purely shear to purely extensional at viscosity ratios ranging from 0.01 to 5.0 and reduced volumes (measured asphericity, higher is more spherical) from 0.60 to 0.70. The vesicle's viscosity ratio appears to play a minimal role in describing its shape and stability for many mixed flows, even in cases when significant flows are present in the vesicle interior. We find in these cases that the bending critical capillary number for shape instabilities collapse onto similar values if the capillary number is scaled by an effective extensional rate. These results contrast with droplet studies where both viscosity ratio and flow type have significant effects on breakup. Our simulations suggest that if the flow type is not close to pure shear flow, one can accurately quantify the shape and stability of vesicles using the results from an equiviscous vesicle in pure extension. Only when the flow type is nearly shear flow, do we start to see deviations in the observations discussed above. In

this situation, the vesicle's stationary shape develops a shape deviation, which introduces a stabilizing effect and makes the critical capillary number depend on the viscosity ratio.

Continuing with our research on single vesicle dynamics, we have performed simulations and experiments on vesicles in large amplitude oscillatory extensional (LAOE) flows. By using LAOE we can probe the non-linear extension and compression of vesicles and how these types of deformation affect dilute suspension microstructure in time-dependent flows through contractions, expansions, or other complex geometries. Our numerical and experimental results for vesicles of reduced volumes from 0.80 to 0.95 have shown there to be three general dynamical regimes differentiated by the amount of deformation that occurs in each half cycle. We have termed the regimes: symmetrical, reorienting, and pulsating in reference to the type of deformation that occurs. We find the deformation of the quasispherical vesicles in the microfluidic experiments and boundary element simulations to be in quantitative agreement. The distinct dynamics observed in each regime result from a competition between the flow frequency, flow time scale, and membrane deformation timescale. Using the numerical results, we calculate the particle coefficient of stresslet and quantify the nonlinear relationship between average vesicle stress and strain rate. We additionally present some results on the dynamics of tubular vesicles in LAOE, showing how the experiments suggest the vesicles undergo a shape transformation over several strain rate cycles. Broadly, our work provides new information regarding the transient dynamics of vesicles in time-dependent flows that directly informs bulk suspension rheology.

Our most recent project deals with the accuracy of discretized double layer integrals for Stokes flow in the boundary element method. In the fluid mechanics literature, the chosen parameterization, meshing procedure, and singularity handling are often selected arbitrarily or based on a convergence study where the number of elements is decreased until the relative error is sufficiently low. A practical study on the importance of each of these parameters to the accurate calculation of physically relevant results, such as the particle stresslet, could alleviate some of the guesswork required. The analytical formulas for the eigenfunctions/eigenvalues of the double layer operator of an ellipsoidal particle in a quadratic flow were recently published [1], providing an analytical basis for testing boundary element method discretization accuracy. We use these solutions to examine the local and

global errors produced by changing the interpolation order of the geometry and the double-layer density. The results show that the local errors can be significant even when the global errors are small, prompting additional study on the distribution of local errors. Interestingly, we find that increasing the interpolation orders for the geometry and the double layer density does not always guarantee smaller errors. Depending on the nature of the meshing near high curvature regions, the number of high aspect ratio elements, and the flatness of the particle geometry, a piecewise-constant density can exhibit lower errors than piecewise-linear density, and there can be little benefit from using curved triangular elements. Overall, this study provides practical insights on how to appropriately discretize and parameterize three-dimensional (3D) boundary-element simulations for elongated particles with prolate-like and oblate-like geometries.

1. INTRODUCTION

The physics of cells has been of central interest in many fields. These systems have sizes in the range of 1 to 10 μm, allowing them to be visible by optical microscopy. The membranes acting as the boundary of cells are particularly interesting, as these structures modulate the interactions between the cell and external variables. It is not yet possible to empty the contents of a cell and study the membrane independently. If such a process were developed, studying such a system would still be complicated by the presence of membrane proteins, ion channels, and other lipid species. In the fluid dynamics literature, researchers use simplified systems and models for these cell-like systems. Of particular focus in fluids research are the dynamics of these systems in microhydrodynamic settings, like the microcirculation of the body or flow in microfluidic devices. Recent innovations and discoveries have renewed the community's interest in examining these systems. For example, several groups have designed microfluidic devices to separate suspensions of blood without the need for centrifugation [2], [3]. Other groups have worked on ideas such as designing devices that can measure single cell properties at a high throughput to screen for diseases [4]–[6]. Many models and numerical frameworks have been proposed for capsule and vesicle dynamics alongside with advances in experimental methods [7]–[9]. The many advancements and open questions in the field motivates the research in this thesis on numerical simulations of giant vesicles.

1.1 Vesicle dynamics

Vesicles consist of a droplet enclosed by a phospholipid bilayer membrane of thickness ≈ 5 nm, as imaged in Fig. 1.1. For part of this thesis, we examine the dynamics of giant unilamellar vesicles (GUVs), which are vesicles with a diameter of around 10 μm. GUVs are similar to common anuclear cells in both size and composition, which is why they have been used as a model system to study the structure, mechanics, and function of phospholipid bilayers [7], [10]. In recent years, GUVs have been used in a wide array of applications such as bioinspired microreactors [11], [12] or platforms for rapid gene expression [13], [14]. Therefore for using GUVs as a model system and in applications, precise characterization of vesicle dynamics in fluid flow is of fundamental importance.
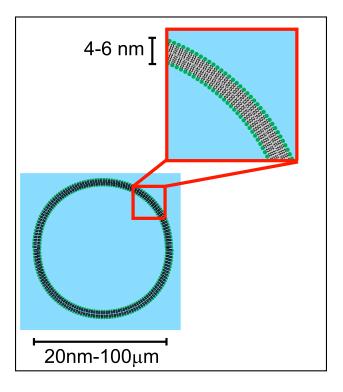
Figure 1.1. Diagram of a lipid vesicle. Adapted from MDougM, Public domain, via Wikimedia Commons

The lipid membrane of a vesicle can be approximated as an elastic, two-dimensional, fluid interface at the length scale of GUVs [15]. Due to the elastic membrane of a vesicle, the dynamics of these systems are different from those of droplets. Researchers commonly assume that the lipid membrane flows freely [16]. The elastic deformation of the membrane can be described by surface dilation and bending [15]. The bending modulus of vesicles can be measured by membrane aspiration or thermal fluctuation analysis [16], [17]. For the spherical vesicle case, that occurs during swelling for example, only the dilation needs to be taken into account as bending is not possible. On the other hand for osmotically deflated vesicles, the resistance to bending deformations is on the order of $2 - 50k_BT$ while the stretching energy is very large. [17]. The large stretching energy and the fact that the number of lipids in the membrane is constant, makes it reasonable to assume that the membrane is incompressible, preventing any surface dilation [16]. These deflated vesicles can have conformations similar to ones seen for anuclear cells, such as the biconcave shape

of red blood cells. The osmotically deflated vesicle system is therefore a good model system for studying the dynamics of bendable, cell-like particles.

With constant surface area and volume, the configurations of vesicles can be described by the minimization of the bending energy theory introduced by Helfrich in the seventies [15], [18]. Theoretical work alongside experiments in the nineties used this model to analyze the equilibrium shapes of vesicles, as reviewed by Seifert [19]. More recent experimental, theoretical, and computational research on vesicle dynamics in flow have largely focused on vesicle dynamics in steady shear flows [16]. Prior studies have observed three dynamical regimes: tumbling, vacillating-breathing, and tank-treading; of which the tumbling and tank-treading regimes have been observed for red blood cells [16]. The dynamic observed depends on the imposed shear rate, amount of osmotic deflation, and the ratio between the inner and outer fluid viscosity [20]–[25]. The phase diagrams of the dynamical regimes in shear flow have been analyzed over a number of studies, and the theory agrees well with experiments and simulations [22], [26]–[28]. Knowledge of vesicle dynamics has been essential for interpreting the behavior of similar cell-like systems and the bulk rheological response for dilute vesicle suspensions. For example, we now know that the tank-treading to tumbling behavior of vesicles directly affects the bulk viscosity of the suspension [29].

Extensional flows, simple linear flows that effectively stretch or compress a deflated vesicle, are another important flow type to understand vesicle dynamics in. These flow types are commonly encountered in microfluidic devices that use contractions or expansions, porous media, and other complex channel geometries. Examining vesicle dynamics in these flow types has been essential to improving our understanding of how vesicles and other cell-like particles stretch and compress in biological systems or microfluidic devices. In a steady extensional flow, it is known that highly deflated tubular vesicles deform into a symmetric dumbbell shape [30]–[33]. On the other hand, moderately deflated vesicles transition to an asymmetric dumbbell shape above a critical flow strength [33]–[35]. For both highly and moderated deflated vesicles, a tether forms such that the vesicle can be stretched far from its initial quiescent shape [36].

In this thesis, we examine the shape stability of vesicles in extensional flows with a vorticity component (mixed flows) and vesicle dynamics in large amplitude oscillatory extension.

While the shape stability of vesicles in extensional flows is well studied in the literature, it is unclear how adding a rotational component to the external flow affects the stability. Note that, unlike for the droplet case, vesicles do not experience breakup or large deformations in shear flows. On the other hand, our study on vesicle in oscillatory extensional flow addresses the literature gap on time-dependent vesicle dynamics. Understanding these time-dependent dynamics are important for systems like *in vivo* capillaries and complex microfluidic devices that have many bifurcations and sharp directional changes that routinely encounter time-dependent pulsatile flows. From this view, there is a need for comprehensive studies on how microscopic stretching and compression of vesicles in complex, time-dependent oscillatory flows will affect their shape and bulk rheology.

1.2 Modelling vesicles

Here we will briefly show how one can model a GUV system at the continuum level as a droplet with a two-dimensional incompressible fluid membrane. At the length scale of a cell ($\sim$ 10 microns), the Reynold's number (Re) is generally very small. We can model the system with the assumption of negligible Reynold's number, allowing us to model the fluids with the Stokes equations:

$$\frac{\partial \rho}{\partial t} + \nabla \cdot (\rho \boldsymbol{v}) = 0, \quad \nabla \cdot \boldsymbol{\sigma} = 0 \tag{1.1}$$

where ρ is the density, $\boldsymbol{v}$ is the velocity and $\boldsymbol{\sigma}$ is the stress tensor. We assume that the vesicle maintains a constant volume over an experimental timeframe of 10 to 15 minutes[9]. Researchers also commonly assume the inner and outer fluids of a vesicle or red blood cell are Newtonian. Assuming the inner fluid is poroelastic would be more accurate for cells, as that would take into account the cytoskeleton. However adding poroelasticity complicates the model significantly, and using a Newtonian inner fluid assumption produces results comparable to those seen in experiments [8]. Assuming the fluid is Newtonian, we get a set of linear equations for the mass and momentum balances:

$$\nabla \cdot \boldsymbol{v} = 0, \quad \nabla p = \mu \nabla^2 \boldsymbol{v} \tag{1.2}$$

The vesicle system is subject to continuity of velocity and a traction balance across the interface. At the timescales and strain rates used in previous studies, membrane dilatation is negligible [17], [37]. Vesicles are also known to have negligible shear rigidity as they do not have a cytoskeletal network or an actin cortex. We can therefore use a simplified version of the Helfrich model [15] for the membrane:

$$\mathbb{H} = \oint \frac{\kappa}{2}(2H)^2 dA + \oint \sigma dA. \tag{1.3}$$

In Eq. (1.3), $\mathbb{H}$ represents the elastic energy of the vesicle membrane, κ is the membrane bending modulus, H is the mean curvature, and σ is the surface tension. The surface tension is a spatially varying Lagrange multiplier that ensures local area conservation on the interface:

$$\nabla_s \cdot \boldsymbol{u} = 0, \tag{1.4}$$

where $\nabla_s = (\boldsymbol{I} - \boldsymbol{nn}) \cdot \nabla$. Here we neglect contributions from thermal fluctuations, spontaneous curvature, and bilayer friction [19], [38].

The first variation of Eq. (1.3) with respect to the interface can be calculated to produce the membrane traction from the bending resistance. The same procedure can be performed for the surface tension term to produce the following traction balance:

$$[[\boldsymbol{f}]] = [[\boldsymbol{T} \cdot \boldsymbol{n}]] = \boldsymbol{f_t} + \boldsymbol{f_b}$$
$$\boldsymbol{f_t} = (2H\sigma\boldsymbol{n} - \nabla_s\sigma)$$
$$\boldsymbol{f_b} = \kappa(4KH - 4H^3 - 2\nabla_s^2 H)\boldsymbol{n} \tag{1.5}$$

where $[[\boldsymbol{f}]]$ is the jump in viscous traction across the interface which can be decomposed to the bending ($\boldsymbol{f_b}$) and tension ($\boldsymbol{f_t}$) contributions, $\boldsymbol{n}$ is the outward-pointing unit normal vector, and K is the Gaussian curvature of the interface. The mean curvature H is defined to be one for the unit sphere. We now have a set of equations (Eq. (1.2)) for the inner and outer fluids with a hydrodynamic traction balance boundary condition.

1.3   Simulating vesicles with the boundary element method

The boundary element method is a Green's function method, some of the main benefits of which include a reduction in dimensionality and a straightforward implementation of deformable boundaries. The equations from the previous section can be solved directly by several other methods ranging from front-tracking to finite-element-based methods [39]–[42]. For the volume-based methods, we would discretize the system into volume elements such as tetrahedrons. However as the equations are linear, we can use Green's functions to simplify the system. Firstly, we identify two of the free-space Green's functions for Stokes flow, the Stokeslet and stresslet:

$$G_{ij}(\boldsymbol{x}, \boldsymbol{x_0}) = \frac{\delta_{ij}}{r} + \frac{\hat{x}_i \hat{x}_j}{r^3} \tag{1.6}$$

$$T_{ijk}(\boldsymbol{x}, \boldsymbol{x_0}) = -6\frac{\hat{x}_i \hat{x}_j \hat{x}_k}{r^5} \tag{1.7}$$

Where $r = |\hat{\boldsymbol{x}}|$, $\hat{\boldsymbol{x}} = \boldsymbol{x} - \boldsymbol{x_0}$, and $\boldsymbol{x_0}$ is the source point. Repeated indices are assumed to be summed over. $\boldsymbol{G}$ is the solution for Stokes flow from a point force and $\boldsymbol{T}$ is the corresponding solution for the stress tensor. Now to derive the boundary integral, we start from the Lorentz reciprocal identity:

$$\nabla \cdot (\boldsymbol{v}' \cdot \boldsymbol{\sigma} - \boldsymbol{v} \cdot \boldsymbol{\sigma}') = 0 \tag{1.8}$$

where (v', σ') and (v, σ) are two velocity and stress fields that satisfy the Stokes equations. We identify the primed flow as that resulting from a point force with strength $\boldsymbol{g}$ located at the point $\boldsymbol{x_0}$ such that:

$$\boldsymbol{v}'_i(\boldsymbol{x}) = \frac{1}{8\pi\mu}G_{ij}(\boldsymbol{x}, \boldsymbol{x_0})g_j \quad \boldsymbol{\sigma}'_{ik}(\boldsymbol{x}) = \frac{1}{8\pi}T_{ijk}(\boldsymbol{x}, \boldsymbol{x_0})g_j \tag{1.9}$$

Substituting in the primed components and discarding the arbitrary constant $\boldsymbol{g}$:

$$\frac{\partial}{\partial x_j}[G_{ij}(\boldsymbol{x}, \boldsymbol{x_0})\sigma_{ik}(\boldsymbol{x}) - \mu v_i(\boldsymbol{x})T_{ijk}(\boldsymbol{x}, \boldsymbol{x_0})] = 0 \tag{1.10}$$

21
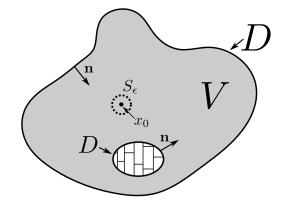
Figure 1.2. Arbitrary control volume V and closed surface D. Normal vectors $\boldsymbol{n}$ all point into the control volume. Interior $\boldsymbol{x}_0$ point with small surrounding surface S_ϵ.

Now we proceed to convert the expression into an integral form by considering an arbitrary control volume V bounded by the closed surface D, as shown in Fig. 1.2. We define the interior side as that in the control volume and the exterior side as everything else. The normal vector is defined to be pointing into the interior side. We want a formulation to solve for either the tractions or velocities on D, therefore we need to do a limiting procedure for $\boldsymbol{x}_0$ from the interior or exterior to the surface D. For $\boldsymbol{x}_0$ outside of V, Eq. (1.10) is regular over the control volume so we can integrate over V and use the divergence theorem to convert to a surface integral. Thus for points $\boldsymbol{x}_0$ exterior to V the boundary integral is:

$$\int_D [G_{ij}(\boldsymbol{x}, \boldsymbol{x_0})\sigma_{ik}(\boldsymbol{x}) - \mu v_i(\boldsymbol{x})T_{ijk}(\boldsymbol{x}, \boldsymbol{x_0})]n_k(\boldsymbol{x})\, dS(\boldsymbol{x}) = 0 \tag{1.11}$$

For points inside V, we use a limiting routine to integrate over the volume $V - V_\epsilon$ where V_ϵ is a sphere of radius ϵ around $\boldsymbol{x}_0$. Using the divergence theorem and taking the limit as $\epsilon \to 0$, we obtain the boundary integral form for interior points:

$$v_j(\boldsymbol{x_0}) = -\frac{1}{8\pi\mu}\int_D \sigma_{ik}(\boldsymbol{x})n_k(\boldsymbol{x})G_{ij}(\boldsymbol{x}, \boldsymbol{x_0})\, dS(\boldsymbol{x}) + \frac{1}{8\pi}\int_D v_i(\boldsymbol{x})T_{ijk}(\boldsymbol{x}, \boldsymbol{x_0})n_k(\boldsymbol{x})\, dS(\boldsymbol{x})$$

$$\tag{1.12}$$

In Eq. (1.12), we identify the first integral on the right-hand side as the single layer potential and the second integral as the double layer potential. Note that the single layer potential

varies continuously across the boundary D while the double layer potential experiences a jump. If D has a continuously varying normal vector and velocity, we deduce the limit of the double layer potential as $\boldsymbol{x}_0$ approaches D as the following identity:

$$\lim_{\boldsymbol{x}_0 \to D} \int_D v_i(\boldsymbol{x}) T_{ijk}(\boldsymbol{x}, \boldsymbol{x}_0) n_k(\boldsymbol{x}) \, dS(\boldsymbol{x}) = \pm 4\pi v_j(\boldsymbol{x}_0) + \int_D^{PV} v_i(\boldsymbol{x}) T_{ijk}(\boldsymbol{x}, \boldsymbol{x}_0) n_k(\boldsymbol{x}) \, dS(\boldsymbol{x})$$

(1.13)

where the plus sign applies for interior flows and the minus for exterior flows. The superscript PV denotes the principal value when $\boldsymbol{x}_0$ is on D. Substituting the proper form of Eq. (1.13) into Eq. (1.11) or Eq. (1.12), we find the formulation for $\boldsymbol{x}_0$ on D

$$v_j(\boldsymbol{x}_0) = -\frac{1}{4\pi\mu} \int_D \sigma_{ik}(\boldsymbol{x}) n_k(\boldsymbol{x}) G_{ij}(\boldsymbol{x}, \boldsymbol{x}_0) \, dS(\boldsymbol{x}) + \frac{1}{4\pi} \int_D v_i(\boldsymbol{x}) T_{ijk}(\boldsymbol{x}, \boldsymbol{x}_0) n_k(\boldsymbol{x}) \, dS(\boldsymbol{x})$$

(1.14)
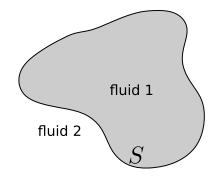
Figure 1.3. Sketch of arbitrary interface between two fluids. Normal vector always points towards the selected control volume.

Many of the systems of interest have constitutive equations defined as surface force jumps at the interface. Therefore we commonly use an altered version of the boundary integral equations that are more accessible for interfacial boundary conditions, and are defined with respect to the force jump across the interface and the viscosity ratio between the interior and exterior fluids. A sketch of the configuration is shown in Fig. 1.3, where we define two fluids separated by an interface S. Starting with fluid 1 as the control volume, we choose a

source point inside of fluid 1. We use the interior form of the boundary integral (BI) equation (Eq. (1.12)) and get

$$v_j^{(1)}(\boldsymbol{x}_0) = -\frac{1}{8\pi\mu_1} \int_S f_i^{(1)}(\boldsymbol{x}) G_{ij}(\boldsymbol{x}, \boldsymbol{x}_0) \, dS(\boldsymbol{x}) + \frac{1}{8\pi} \int_S v_i(\boldsymbol{x}) T_{ijk}(\boldsymbol{x}, \boldsymbol{x_0}) n_k(\boldsymbol{x}) \, dS(\boldsymbol{x}) \quad (1.15)$$

where the superscript (1) corresponds to the interior fluid values and $\boldsymbol{f}$ is the traction $\boldsymbol{\sigma} \cdot \boldsymbol{n}$, such that $\boldsymbol{f}^{(1)}$ is the traction over side 1 of the interface. For the same source point but fluid 2 as the control volume, we use the exterior BI (Eq. (1.11))

$$\int_S f_i^{(2)} G_{ij}(\boldsymbol{x}, \boldsymbol{x}_0) \, dS(\boldsymbol{x}) - \mu_2 \int_S v_i(\boldsymbol{x}) T_{ijk}(\boldsymbol{x}, \boldsymbol{x_0}) n_k(\boldsymbol{x}) \, dS(\boldsymbol{x}) = 0 \quad (1.16)$$

Combining these two equations, we get the desired form for velocity in fluid 1:

$$v_j^{(1)}(\boldsymbol{x}_0) = -\frac{1}{8\pi\mu_1} \int_S [[f_i(\boldsymbol{x})]] G_{ij}(\boldsymbol{x}, \boldsymbol{x}_0) \, dS(\boldsymbol{x}) + \frac{1-\lambda}{8\pi} \int_S v_i(\boldsymbol{x}) T_{ijk}(\boldsymbol{x}, \boldsymbol{x_0}) n_k(\boldsymbol{x}) \, dS(\boldsymbol{x}) \quad (1.17)$$

where $\lambda = \mu_1/\mu_2$ and $[[\boldsymbol{f}]]$ is the surface force jump.

The same process can be carried out for the velocity in fluid 2, obtaining the equation

$$v_j^{(2)}(\boldsymbol{x}_0) = -\frac{1}{8\pi\mu_1\lambda} \int_S [[f_i(\boldsymbol{x})]] G_{ij}(\boldsymbol{x}, \boldsymbol{x}_0) \, dS(\boldsymbol{x}) + \frac{1-\lambda}{8\pi\lambda} \int_S v_i(\boldsymbol{x}) T_{ijk}(\boldsymbol{x}, \boldsymbol{x_0}) n_k(\boldsymbol{x}) \, dS(\boldsymbol{x})$$

$$(1.18)$$

Then by having the point $\boldsymbol{x}_0$ approach the interface from either fluid 1 or fluid 2, we find both Eq. (1.17) and Eq. (1.18) reduce to

$$v_j(\boldsymbol{x}_0) = -\frac{1}{(4\pi\mu_1)(\lambda+1)} \int_S [[f_i(\boldsymbol{x})]] G_{ij}(\boldsymbol{x}, \boldsymbol{x}_0) \, dS(\boldsymbol{x}) + \frac{(1-\lambda)}{4\pi(1+\lambda)} \int_S^{PV} v_i(\boldsymbol{x}) T_{ijk}(\boldsymbol{x}, \boldsymbol{x}_0) n_k(\boldsymbol{x}) \, dS(\boldsymbol{x})$$

$$(1.19)$$

This is the formulation that will be used for simulating vesicles. We could use the formulation from Eq. (1.5) for $[[\boldsymbol{f}]]$, however the bending traction requires us to calculate a Laplace-Beltrami operator on the curvature. To avoid high order numerical differentiation, we apply

the virtual work principal and perform a finite difference scheme on the energy term for interface changes. The hydrodynamic force on the surface at a location β would thus be

$$[[\boldsymbol{f}]]_\beta = \frac{1}{A_\beta} \frac{\partial W}{\partial \boldsymbol{x}_\beta}. \tag{1.20}$$

Where W is the surface energy functional, which is the Helfrich energy from Eq. (1.3). A_β is the local surface area at the point β.

With the boundary integral formulation, the Stokes flow can be computed using a surface mesh rather than a volume mesh, potentially reducing computational complexity. The surface can be discretized into elements, with some commonly used ones being quadrilaterals, three node flat triangles, or six node curved triangles [43]. In our simulations, we use an unstructured mesh consisting entirely of triangles. The surface is put in the parametric description to allow the same shape functions to be used over each local element. The positions and density distributions on the surfaces are generally interpolated from the nodal values (except for a piece-wise constant density distribution) as

$$x_i = \sum_{n=1}^{\text{nodes}} \phi_n \hat{x}_i^n \tag{1.21}$$

where $\hat{\boldsymbol{x}}^n$ are the nodal vector values and ϕ_n are the nodal shape functions. We approximate the curvature of the surface by using a Loop subdivision surface as done in Spann, *et al* for vesicles and first presented for thin-shell finite-element analysis by Cirak, *et al.* [35], [44]. Elements that contain the point $\boldsymbol{x}_0$ or are close to the source point will be singular or nearly singular, respectively. Several methods have been proposed in the literature to handle the singularity, we use the Duffy transformation and singularity subtraction [45], [46]. For time integration, we use a semi-implicit procedure that is equivalent to the one in [47].

2. VESICLE DYNAMICS IN MIXED FLOWS

2.1 Summary

The dynamics of vesicles in simple shear or extensional flows have been extensively studied, but the conditions where vesicles experience more complex flow types, such as those seen in microfluidic devices or industrial processing conditions, warrants greater investigation. In this study, we used the boundary element method to investigate the shape stability of deflated vesicles in a general linear flow (i.e., linear combinations of extensional and rotational flows). We modeled the vesicles as a droplet with an incompressible interface with a bending resistance. We simulated a range of flow types from purely shear to extensional at viscosity ratios ranging from 0.01 to 5.0 and reduced volumes from 0.60 to 0.70. The vesicle's viscosity ratio appears to play a minimal role in describing its shape and stability for many mixed flows, even in cases when significant flows are present in the vesicle interior. We find in these cases the critical capillary number for shape instabilities collapse onto similar values if the capillary number is scaled by an effective extensional rate. These results contrast with droplet studies where viscosity ratio and flow type both have significant effects on breakup. Our simulations suggest that if the flow type is not close to pure shear flow, one can accurately quantify the shape and stability of vesicles using the results from an equiviscous vesicle in pure extension. When the flow type is nearly shear flow, we start to see deviations in the observations discussed above. In this situation, the vesicle's stationary shape develops a shape deviation, which introduces a stabilizing effect and makes the critical capillary number depend on the viscosity ratio.

2.2 Introduction

Vesicles are a paradigmatic model system for studying the dynamics of cellular systems. Part of the popularity of vesicles originates from their ease of manufacture through electroformation and their large size that can be easily tracked by optical microscopy [49], [50].

The giant unilamellar vesicle (GUV) system is also similar in both size and composition to common anuclear cells. GUVs have been used to describe the motion of red blood cells [29], [51], such as their tank-treading/tumbling/vacillating-breathing behavior in shear flow [29], [52]. From a more functional viewpoint, vesicles are vital components of countless biological processes including cellular digestion [53], cell signaling [54], or exocytosis [55]. Vesicles have also been directly applied to engineering applications such as biocompatible drug delivery [56], [57] or micro-reactors for miniaturization studies [11], [58]. Further motivation for vesicle research originates from the inability of droplet studies alone to describe all of the possible mechanics of vesicles/cells. Some of the differences include the possibility of non-spherical vesicle shapes at global equilibrium [59] and soft, long-wavelength membrane fluctuations [50]. These numerous applications have prompted the biophysics community to be highly interested in studies examining the dynamics of vesicles.

Of interest is vesicle dynamics in external flows like those observed in microfluidic devices or biological systems. Previous research on vesicles in purely extensional flows include the work by Kanstler, *et al.* who experimentally observed that highly deflated, high aspect ratio vesicles extend out into dumbbell-like shapes at extension rates above a critical value [60]. For intermediate-aspect-ratio vesicles, Spjut and Muller observed vesicles transitioning into an asymmetrical dumbbell shape at extension rates above a critical value [34], [61]. Following these results, the Shaqfeh group has done several computational and theoretical studies on the stability and transitional shapes observed from vesicles in extensional flow [31], [32], [35], [47]. Some of the main conclusions from these studies include the negligible dependence of the critical extension rate on the viscosity ratio between the vesicle and the solution, and the importance of the steady-state shape on shape transitions under tension.

At the time of writing, few studies have examined deflated vesicles in general linear flows (i.e., linear combinations of rotational and extensional flows), even though the flow fields a vesicle will experience in complex geometries will not be perfectly shear or extensional. In such flows, determining the stability characteristics of vesicles is essential for manipulating vesicle dynamics.

In this paper, we use numerical simulations to probe the stability of deflated vesicles in a general linear flow field. There have been other experimental and theoretical studies exam-

ining vesicles in such flows, but they have focused on the motion of nearly spherical vesicles, characterizing the phase boundaries between tank-treading, tumbling, and the transitional regimes [28], [29], [62]. We note that studies on droplets in mixed flows have shown that the slender-drop and small deformation theories are close approximations of experimental results for critical extension rate, deformation, and orientation [63], [64]. But the stability of vesicles in such flows is qualitatively different from those observed for droplets. For example, droplets are known to breakup readily in a wide range of flow types, but this does not appear to be the case for vesicles, which appear to be quite stable in nearly shear flows. Furthermore, internal viscosity appears to play a significant role in droplet breakup, but the simulations in this paper do not show such an effect for vesicles, even when significant internal flows are present. We will describe our simulation method, present our stability results and explain our findings in the sections that follow.

2.3 Model and Methods

2.3.1 Governing Equations

We model our system as a droplet surrounded by a two-dimensional incompressible fluid with a bending resistance. At the length scale of a GUV ($a \sim 10\mu m$) with deformation rates at $\dot{\epsilon} \sim 1s^{-1}$, the inner and outer fluids of the system are effectively very viscous with negligible inertial effects. This allows us to model the velocity field inside and outside the vesicle using the Stokes equations.

$$\nabla \cdot \boldsymbol{u} = 0, \quad \nabla p = \mu \nabla^2 \boldsymbol{u} \tag{2.1}$$

In the above equation, $\boldsymbol{u}$ is fluid velocity, p is the pressure, and μ is the fluid viscosity (μ_{in} for the inner fluid and μ_{out} for the outer fluid). The system is subject to continuity of velocity across the interface and a force balance across the phospholipid bilayer. The short timescales and low deformation rates used in previous studies makes membrane dilatation negligible [17], [37]. Vesicles are also known to have negligible shear rigidity as they do not

have a cytoskeletal network or an actin cortex. We therefore choose to use the Helfrich model [15], a commonly used model that takes these factors into account.

$$\mathbb{H} = \oint \frac{\kappa}{2}(2H)^2 dA + \oint \sigma dA \tag{2.2}$$

In Eq. (2.2), $\mathbb{H}$ represents the elastic energy of the vesicle membrane. κ is the membrane bending modulus, H is the mean curvature, and σ is the surface tension. The surface tension is a spatially varying Lagrange multiplier that ensures local area conservation. Previous literature has shown that local area conservation leads to good global area incompressibility [65], [66]. The surface tension enforces $\nabla_s \cdot \boldsymbol{u} = 0$ on the interface, where $\nabla_s = (\boldsymbol{I} - \boldsymbol{nn}) \cdot \nabla$. We note that the original Helfrich model includes spontaneous curvature, a parameter to describe a membrane's curvature preference when the sides of the bilayer are chemically different. While vesicles *in-vivo* may have multiple lipid components or chemical differences between the inner and outer fluids [18], [67], [68], experimental studies have focused on single component vesicles with only a viscosity difference between the fluids, prompting a negligible spontaneous curvature. We have additionally neglected any contributions from thermal fluctuations, membrane viscosity, and bilayer friction [19], [38].

At mechanical equilibrium, the force balance at the membrane surface becomes:

$$[[\boldsymbol{f}]] = [[\boldsymbol{T} \cdot \boldsymbol{n}]] = \boldsymbol{f_t} + \boldsymbol{f_b} = (2H\sigma\boldsymbol{n} - \nabla_s\sigma) + (\kappa(4KH - 4H^3 - 2\nabla_s^2 H)\boldsymbol{n}) \tag{2.3}$$

$[[\boldsymbol{f}]]$ is the jump in viscous traction across the interface which can be decomposed to the bending $(\boldsymbol{f_b})$ and tension $(\boldsymbol{f_t})$ contributions, where $\boldsymbol{n}$ is the outward-pointing unit normal vector, and K is the Gaussian curvature of the interface. The mean curvature H is defined to be 1 for the unit sphere.

The vesicle is placed in an external, linear flow field described by $\boldsymbol{u}^\infty = \nabla\boldsymbol{u}^\infty \cdot \boldsymbol{x}$. We define it as:

$$\nabla\boldsymbol{u}^\infty = \frac{\dot{\epsilon}}{2}\begin{bmatrix} \alpha + 1 & 1 - \alpha & 0 \\ \alpha - 1 & -1 - \alpha & 0 \\ 0 & 0 & 0 \end{bmatrix} \tag{2.4}$$

where $\dot{\epsilon}$ is the deformation rate and α is a flow parameter that controls the flow type the vesicle experiences. The value $\alpha = 1$ corresponds to planar extensional flow, $\alpha = 0$ is shear flow, and $\alpha = -1$ is pure rotation. We additionally define an exit streamline as the eigenvector corresponding to the principal eigenvalue:

$$\boldsymbol{b} = (\frac{-1 - \sqrt{\alpha}}{-1 + \sqrt{\alpha}}, -1)\, \alpha \neq 1 \tag{2.5}$$

The membrane area (A) is kept constant by the incompressiblity constraint while the low permeability of the membrane allows us to assume that the volume (V) of the vesicle is constant during the timescale of experiments (minutes). Therefore, we non-dimensionalize distances by the equivalent radius $a = \sqrt{A/(4\pi)}$, time scales by $\dot{\epsilon}^{-1}$, velocities by $\dot{\epsilon}a$, stresses by $\mu_{out}\dot{\epsilon}$, and surface tensions by $\mu_{out}\dot{\epsilon}a$. We obtain four dimensionless groups of interest from the non-dimensionalization:

$$\mathrm{Ca} \equiv \frac{\mu_{out}\dot{\epsilon}a^3}{\kappa}, \quad \lambda \equiv \frac{\mu_{in}}{\mu_{out}}, \quad \nu \equiv \frac{3V}{4\pi a^3}, \quad \alpha \tag{2.6}$$

The capillary number (Ca) compares the bending timescale to flow timescale. Therefore, a high Ca would mean the vesicle shape is dominated by the external flow. The viscosity ratio (λ) is the ratio of inner and outer fluid viscosity. As cellular systems such as RBCs commonly have a more viscous inner fluid, the parameter can be tuned to more closely model the system of choice. The reduced volume (ν) is a measure of the asphericity of the vesicle, or a measure of its osmotic deflation. For example, a reduced volume of 1 would be a perfect sphere, while a value of 0.2 would be highly deflated. One can experimentally alter the reduced volume of a vesicle by introducing an osmotic shock such as adding sucrose to the outer fluid. The flow parameter α was described earlier, and it describes what type of mixed flow the vesicle will experience (pure rotation to pure extension).

Applying this non-dimensionalization, the force balance becomes:

$$[[\boldsymbol{T} \cdot \boldsymbol{n}]] = \boldsymbol{f_t} + \mathrm{Ca}^{-1}\boldsymbol{f_b} \tag{2.7}$$

2.3.2 Boundary Integral Formulation

The Stokes flow assumption allows us to use the boundary integral (ie, Green's function) formulation to simulate the vesicle. We recast the Stokes equations into a boundary integral form:

$$\frac{1+\lambda}{2}u_j(\boldsymbol{x_0}) = u_j^\infty(\boldsymbol{x_0}) - \frac{1}{8\pi}\int_S G_{ij}(\boldsymbol{x},\boldsymbol{x_0})[[f_i]](\boldsymbol{x})dA(\boldsymbol{x}) + \frac{1-\lambda}{8\pi}\int_S T_{ijk}(\boldsymbol{x},\boldsymbol{x_0})u_i(\boldsymbol{x})n_k(\boldsymbol{x})dA(\boldsymbol{x})$$

(2.8)

where u_i^∞ is the external velocity field and $[[f_i]]$ is the jump in viscous traction across the interface, given by Eq. (2.7). The kernels $G_{ij}(\boldsymbol{x},\boldsymbol{x_0})$ and $T_{ijk}(\boldsymbol{x},\boldsymbol{x_0})$ are the Stokeslet (point force) and stresslet (point dipole) solutions to Stokes flow:

$$G_{ij}(\boldsymbol{x},\boldsymbol{x}_0) = \frac{\delta_{ij}}{r} + \frac{\tilde{x}_i\tilde{x}_j}{r^3}$$

(2.9)

$$T_{ijk}(\boldsymbol{x},\boldsymbol{x}_0) = -6\frac{\tilde{x}_i\tilde{x}_j\tilde{x}_k}{r^5}$$

(2.10)

where $\tilde{\boldsymbol{x}} = \boldsymbol{x} - \boldsymbol{x}_0$ and $r = |\tilde{\boldsymbol{x}}|$. Repeated indices are assumed to be summed in the above equations. These equations are also subject to the membrane incompressibility constraint:

$$\nabla_s \cdot \boldsymbol{u} = 0$$

(2.11)

Our simulations use code extended from Spann, *et al.* [35]. The simulation procedure begins by discretizing the vesicle surface into an unstructured mesh of at least 5120 triangular elements. We solve for the velocity, pressure, and surface tension at each mesh point by using the predictor-corrector scheme from [69]. For computing the bending forces, we first approximate the curvature with Loop subdivision [35] and then apply the virtual work principle on the Helfrich energy functional [35]. After solving for the velocity at each mesh point, we translate the vertices by their normal velocity. The tangential velocity component is replaced by a mesh relaxation scheme similar to the one mentioned in [70]. Finally, we enforce the constant volume constraint by performing an affine transformation on the vesicle shape. This process is repeated until the desired amount of time has been simulated.

2.3.3 Vesicle Shape Stability
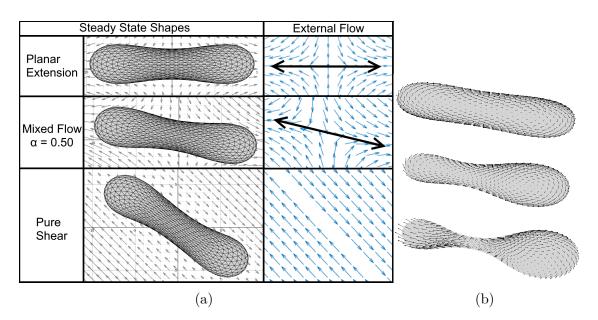
Figure 2.1. (a) steady state vesicle shapes and the corresponding external velocities. The arrows correspond to the exit streamline. (b) simulated asymmetrical instability and surface velocities.

In this study, we examine the stability of a vesicle under a steady, linear flow field. When a vesicle is deflated (reduced volume $0.58 < \nu < 0.75$), a vesicle under pure extension will transition to an asymmetric dumbbell above a critical capillary number (Fig. 2.1). The shape instabilities we examine in mixed flows will look similar to this process, although there will now be internal flows inside the vesicle due to the imposed vorticity. The asymmetric dumbbell deformation is assumed to grow indefinitely, suggesting breakup, but could also lead to additional stationary shapes. The origin of the asymmetric dumbbell instability is outlined in Narsimhan et al., [31] but briefly, it arises due to the Laplace pressure induced in the pinched side of the vesicle, which drives flow toward the expanded side. Since the surface tension of the membrane is a function of the flow, this effect only occurs above a critical flow strength. To avoid highly deformed meshes and large capillary numbers, we decided to limit our simulations to the range of $\nu = 0.60$ to 0.70. We note that the history of the flow field, such as sudden increase in flow strength, could also affect vesicle stability, but topic is outside the scope of the paper and will be examined in a future manuscript.

The simulation procedure begins by first obtaining a vesicle at steady-state, which is accomplished by simulating a prolate spheroidal mesh in external flow until the normal velocities at the vertices approach zero. This method differs from previous spectral simulations, where they discarded the asymmetric contributions of the shape to obtain the equilibrium shape [47]. We then apply a small sinusoidal perturbation to the steady-state mesh, and determine the conditions under which this perturbation will grow. Experimentally, this perturbation would occur spontaneously due to additional factors such as thermal fluctuations or minor flow perturbations. This perturbation is necessary for the simulation because while our simulation does not automatically enforce symmetry, the minor asymmetries present in the finite mesh representation of the vesicle will not spontaneously start the instability for capillary numbers close to the critical value. The perturbation is defined as:

$$r(z) = r_0(z) + \beta \sin(2\pi z / z_{max}) \tag{2.12}$$

Where r is the distance from the interface to the major axis of the vesicle shape, and β a small number, usually of order 0.01 times the original radius r_0. Visually, this perturbation makes one side of the vesicle slightly larger than the other (Fig. 2.1). Above a critical capillary number, the perturbation will grow, while below the critical capillary number the perturbation will return to its steady configuration.

We note that the growth rate of the instability becomes increasingly small as the capillary number is near its critical value. This effect is significant because one typically has to simulate for long periods of time to visualize the instability at this transition. We decided to use a more robust method for determining the stability of a simulation by tracking the growth of the asymmetric perturbation. Previous simulations that tested vesicle stability in uniaxial extension were able to extract the Legendre polynomial representation of the vesicle shape and check the growth rate of the odd modes [35], [69]. Our simulations of vesicles in mixed flows will not be radially symmetric, but we can do the same analysis for a $z = 0$ slice of the vesicle shape (i.e., the plane where flow occurs).

Our procedure consists of first projecting all the vertices onto the $z = 0$ plane and then using a concave hull algorithm [71] to select the vertices enclosing the projection. We
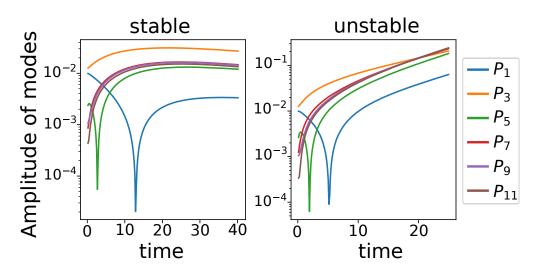
Figure 2.2. Odd Legendre polynomials for a stable and unstable simulation. The stable (unstable) simulation decrease (increase) exponentially after some transient initial effects. Mixed and extensional flows show qualitatively similar results for this analysis. The dips in the coefficients are some transient behavior and were also seen in Spann, *et al.* [35].

record the distances from the vertices to the vesicle's major axis, re-scale the points so that the endpoints of the major axis are at ± 1, and fit the shape to Legendre polynomials up to order 32 using the least squares method. If the resultant coefficients for odd order polynomials consistently increase with time, we determine that the sinusoidal perturbation grows, eventually leading to the asymmetric instability. The even polynomial coefficients are constant until the shape becomes significantly deformed. This method allows us to determine the stability with fewer timesteps. An example of the odd Legendre coefficients is shown in Fig. 2.2.

2.4 Results and Discussion

The shape stability of a vesicle in pure planar extensional flow ($\alpha = 1$) has been studied extensively by Kantsler et al. and Dahl et al. in experiments [34], [60], as well as in computational works by Shaqfeh and co-workers [35], [69]. We benchmarked our simulations with the latter two studies and have been able to replicate their stability phase diagrams. This study focuses on mixed flows with an extensionally dominated component ($0 < \alpha < 1$), which has not been addressed up until this point. Fig. 2.3 shows the stability boundary for vesicles in such flows over several reduced volumes ν and viscosity ratios λ. The critical capillary number diverges with a power-law behavior (exponent roughly 0.6) as the flow type approaches pure shear (i.e., $\alpha \to 0$), leading to no asymmetrical dumbbell deformations for purely shear flows. We note that this behavior is quite different than those observed for droplets, which can readily break up in shear flow if its interior viscosity is not too large [63], [72].

Another interesting finding from the graphs is the dependence of vesicle stability on its viscosity ratio (λ). In previous studies under pure extension ($\alpha = 1$), Narsimhan et al. showed that viscosity ratio plays an inconsequential role in vesicle shape stability, since the vesicle experiences negligible flow in its interior due to membrane incompressibility [31]. The latter statement is not true in mixed flows, since external vorticity leads to substantial circulation in the vesicle interior. Yet, viscosity ratio has a negligible effect on vesicle stability over a wide range of mixed flows, with a deviation occurring close to the pure shear flow
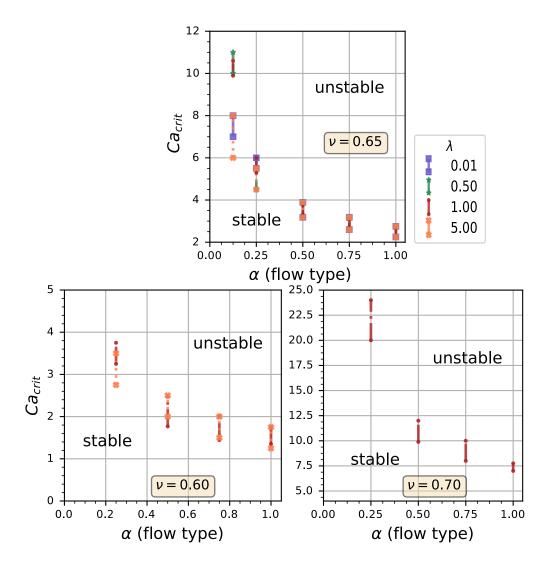
Figure 2.3. Predicted stability boundaries for several reduced volumes ν and viscosity ratios λ. Several of the boundaries overlap exactly. All viscosity ratios were simulated for a reduced volume of 0.65. Simulations of viscosity ratios of 1.0, and 5.0 are shown for a reduced volume of 0.60. The boundaries for the reduced volume 0.70 runs are larger due to higher Ca requiring longer simulation times.
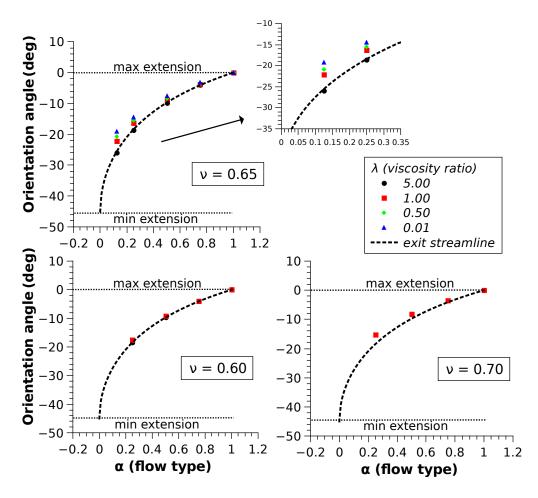
Figure 2.4. Orientation angle of vesicle simulations compared to the exit streamline for vesicles near the stability boundary. Inset focuses on the low alpha regime for $\nu = 0.65$.

($\alpha = 0$) limit. This observation is in contrast to what is observed for droplet suspensions where the internal fluid plays a significant role in break up [64].

To explain the power law dependence of vesicle stability with flow type, we begin with some observations. Firstly, all unstable vesicles we simulated have been in the tank-treading regime. We tracked the orientation angle of the vesicles over time and found all of them stay constant after reaching their steady-state orientation. One can simulate the tumbling and vacillating-breathing regimes by further increasing the viscosity ratio or decreasing α. The majority of the relevant stability boundary will be in the tank-treading regime however, as the rotation timescale for the VB/TU regimes will likely be significantly smaller than the inverse growth rate of the asymmetrical instability, leading to no perceived shape instability.
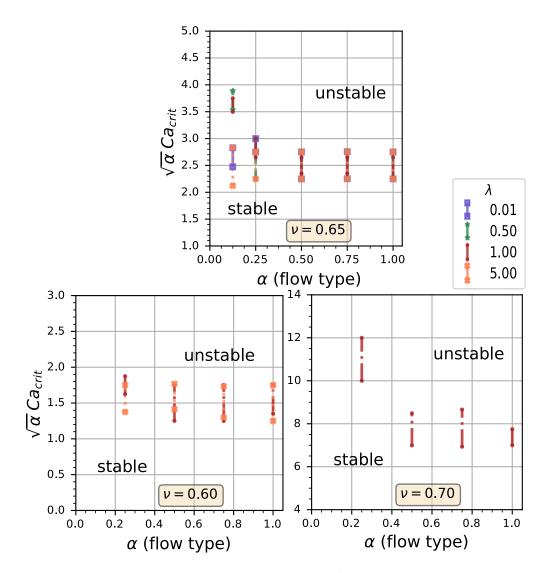
Figure 2.5. Rescaled stability boundaries by $\sqrt{\alpha}$, corresponding to the effective extension along the exit streamline.

Note that the results for $\lambda = 5.0$ suggest that the critical viscosity ratio for the TT-TU transition is affected by the flow type. We have not examined this effect in this study and may examine it in future work.

Secondly, the orientation of the tank-treading vesicles determines the effective extension it experiences. We define the effective extension as:

$$\dot{\epsilon}_{\text{eff}} = \boldsymbol{c} \cdot \nabla \boldsymbol{u}^{\infty} \cdot \boldsymbol{c} = \dot{\epsilon}(\frac{1+\alpha}{2}) \cos(2\theta); \quad 0 < \theta < \pi \tag{2.13}$$

where θ is the orientation angle of the vesicle and $\boldsymbol{c}$ is the major axis of the ellipsoidal vesicle. The vesicle will experience maximum extension when aligned with the x-axis ($\theta = 0$ř) and a minimum extension when aligned at $\theta = -45°$. We can re-define our capillary number based on this effective extension rate

$$\text{Ca}_{\text{eff}} = (\frac{1+\alpha}{2}) \cos(2\theta)\text{Ca}, \tag{2.14}$$

but this representation requires the orientation angle, which is not known *a priori*. Instead, we observe from Fig. 2.4 that the vesicles align closely with the exit streamline of the mixed flow (i.e, the eigenvector of Eq. (2.4) with a positive eigenvalue) for flow types not close to shear flow. The inclination angle differs by at most 4 degrees from the exit streamline for $\alpha \geq 0.250$, suggesting that $\boldsymbol{c} \approx \boldsymbol{b}$. This observation and the approximate power law exponent of roughly 0.60, motivates us to reexamine our data by scaling the capillary number by the effective extension rate along the exit streamline, which is $\sqrt{\alpha}\dot{\epsilon}$. The resultant dimensionless parameter corresponds to the effective capillary number along the exit streamline:

$$\text{Ca}_s = \sqrt{\alpha}\text{Ca}. \tag{2.15}$$

Once applying this scaling in Fig. 2.5, we observe that most of the stability boundary becomes invariant with flow type. These results suggest that the stability of vesicles of any viscosity ratio can be explained by the purely extensional case and a scaled deformation rate if the flow type is $\alpha \geq 0.500$. The stability boundary only begins to diverge from a purely effective extensional effect at close to pure shear flow ($\alpha = 0$).

39

This simple geometric argument for deflated vesicles is remarkable, since it is well known that droplets do not always align well with the flow principal axis. Significant differences in droplet orientation angle have been observed in several experiments, (e.g., Stone, Bentley and Leal, etc. [64], [73]) and helps explain why the stability boundary's dependence on flow type and viscosity ratio has a much more complicated relationship for droplets than the geometric arguments listed above. We note that for vesicles, the orientation angle can deviate greatly from the exit streamline, but this effect only appears important when its shape is quasi-spherical ($\nu > 0.80$), or when the flow type is nearly shear flow. A good reference for studies in the quasi-spherical regimes is in Mishbah and Zhao and Shaqfeh [20], [22], [65], and a good reference for low reduced volume vesicles/cells in shear flow is Keller and Skalak [74]. In our study, the asymmetric dumbbell instabilities occur at reduced volumes $0.58 < \nu < 0.75$ and the flow types significantly away from pure shear, which allows one to make the simple geometry arguments listed above.

In the last part of this section, we will make a few more statements that illuminate the physics of the shape instabilities in mixed flows. In previous studies, researchers found the asymmetric dumbbell shapes arise from a competition between bending forces that try to stabilize the vesicle, and membrane tension that tries to destabilize the vesicle. The first effect is primarily due to geometry (i.e., curvature of the membrane), while the latter effect is coupled through the flow. For more information on vesicle stability in mixed flows, we decided to measure the steady-state vesicle geometry and tensions near the stability boundary.

To begin our analysis, we focus on the moderate to high α regime ($\alpha \geq 0.500$). Let us examine two vesicles with $\mathrm{Ca}_s = 3.00$, $\nu = 0.65$, and $\lambda = 1$: one is in pure extension $\alpha = 1$, and the other is in a mixed flow at $\alpha = 0.5$. Although both vesicles will experience the same effective extension, the vorticity will be noticeably different, leading to different flow patterns in and around the vesicle. How do these flow patterns affect the vesicle shape? We plot the shapes of the two vesicles overlaying each other in Fig. 2.6(a). Overall, the shapes are almost identical, suggesting that the internal circulation induced by vorticity does not appreciably alter vesicle shape at moderate flow parameter α. Vesicles of the same shape have the exact same bending forces, therefore the stabilizing force for the instability will be the same.
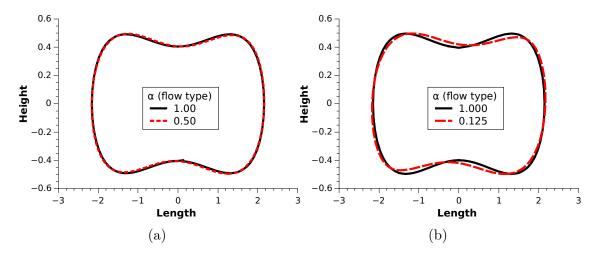
Figure 2.6. Comparing the stationary vesicle shape for vesicles in a purely extensional flow to those seen in mixed flows. Both plots have the parameters: $\lambda = 1.00$ and $Ca_s = 3.00$. The $\alpha = 0.500$ flow (a) results in a stationary shape that closely follows the extensional case. The $\alpha = 0.125$ stationary shape (b) deviates significantly from the extensional case. The y-axis scaling for (b) has been increased to make the shape deviation more noticeable.

We plotted the maximum tension profile along the major axis of the vesicle of the same case in Fig. 2.7. From that figure we see that the tension profile is also invariant for $\alpha \geq 0.500$ at the same scaled capillary number. Overall, the tension profile is similar for most flow types except near shear flow ($\alpha \leq 0.25$). From Fig. 2.7, we also observe that the tension profile is independent of viscosity ratio for $\alpha \geq 0.500$. These results suggest that the internal flows in the vesicle do not play a significant role in modifying the tension on the membrane, most likely because such flows are primarily rotational and hence do not stretch the material elements in the membrane appreciably. With both the membrane bending and tension contributions invariant at the same scaled capillary number for moderate alpha values, we conclude that the vorticity has no significant effect in this regime. Additionally, the stability is independent of the flows internal to the vesicle, and hence does not depend on λ.
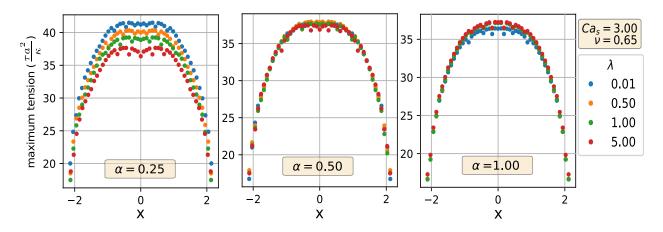
Figure 2.7. Maximum tension values along the major axis of the vesicle stationary shape. Note these are the tensions non-dimensionalized by the bending modulus, equivalent to σCa. Tension is maximized on the z = 0 plane of the vesicle in the planar flow.

When vesicles approach pure shear flow ($\alpha = 0$), we notice that flow type and viscosity ratio start having significant consequences on its stability. To understand the role of these parameters in this regime, we examine the vesicle's shape and orientation. In Fig. 2.4, we observe that that vesicles with higher viscosity ratios align more closely with the exit streamline than those with lower viscosity ratios. This orientation effect leads to the more viscous vesicles experiencing a lower effective extension (Fig. 2.4), which would make one naively conclude that such vesicles would become more stable in flow. This observation is not
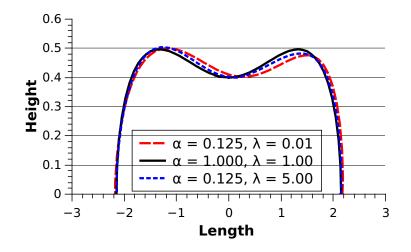
Figure 2.8. Upper half of vesicle stationary shape comparison for $\mathrm{Ca}_s = 2.25$, showing the effect of viscosity ratio. The figure shows the stationary shape for $\alpha = 0.125$ deviating from the purely extensional shape (solid line). The increased viscosity ratio vesicle ($\lambda = 5.00$) shows less deviation than the decreased viscosity ratio case ($\lambda = 0.01$).
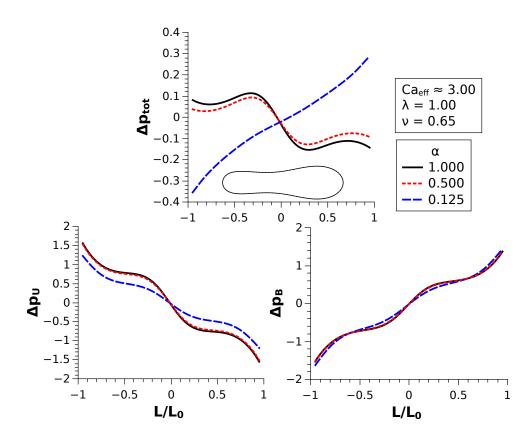
Figure 2.9. Difference in pressure profiles between the stationary and perturbed configurations along the major axis of the vesicle. Ca_{eff} is defined in Eq. (2.14). Ca_{eff} is approximately 3.00 because the orientation angle of the vesicles is not known *a priori*. The exact Ca_{eff} for the $\alpha = [0.125, 0.500, 1.00]$ are $[2.982, 3.006, 3.000]$ respectively. Note that $Ca_{eff} \approx Ca_s$ for the $\alpha = 0.500$ & 1.000 simulations. Inset: exaggerated perturbed shape for reference.

borne by our simulations. Indeed, if one looks at Fig. 2.5, we instead observe the viscosity ratio $\lambda = 5.0$ vesicle has a lower critical capillary number (i.e., more unstable) than an equi-viscous $\lambda = 1$ vesicle. The origin of this counter-intuitive observation is likely due to a change in shape. We see in Fig. 2.6(b) that the shape near shear flow starts developing small, off-center deviations resulting in an "S"-like shape, as is seen for prolate vesicles in shear flow [65]. We emphasize that the vesicle is no longer symmetrical here. The "S"-like shapes are less prominent in higher viscosity ratio vesicles (Fig. 2.8), and it appears that when such shape deviations are absent, the stability trend follows the same trends as $\alpha \geq 0.500$ cases.

However, the shape deviation seen in Fig. 2.6 is a relatively small change, and it does not change drastically even with large differences in viscosity ratio (Fig. 2.8). To probe the

cause for increased vesicle stability for low α flows, we need to examine the driving force that increases the sinusoidal perturbation by pushing the internal fluid from the smaller to larger ends. We decided to calculate the pressure profile along the major axis of the vesicle as it is a good indicator of the internal fluid flow. The pressure at a point x_0 inside of the vesicle can be calculated using Green's functions:

$$p(\boldsymbol{x_0}) = \frac{-1}{8\pi\lambda} \oint P_i(\boldsymbol{x_0}, \boldsymbol{x})[[f_i]](\boldsymbol{x})dS(\boldsymbol{x}) + \frac{1-\lambda}{8\pi\lambda}\mu_{ext} \oint u_i(\boldsymbol{x})\Pi_{ij}(\boldsymbol{x_0}, \boldsymbol{x})n_j(\boldsymbol{x})dS(\boldsymbol{x}) \quad (2.16)$$

$$P_i = \frac{2\hat{x}_i}{r^3}; \quad \Pi_{ij} = 4(-\frac{\delta_{ik}}{r^3} + 3\frac{\hat{x}_i\hat{x}_j}{r^5}) \quad (2.17)$$

where $\hat{\boldsymbol{x}} = \boldsymbol{x_0} - \boldsymbol{x}$. We proceed as in Zhao and Shaqfeh [69] and decompose the pressure as $p = p_B + p_U$, where p_B is the contribution from bending while p_U is from the external flow. We calculate p_B by solving Eq. (2.8) with $u^\infty = 0$ and then calculate the resultant pressure profile. This profile will include a non-zero tension that minimizes the area divergence of the bending forces. p_U is calculated similarly by setting $\boldsymbol{f}_b = 0$ such that $[[\boldsymbol{f}]] = \boldsymbol{f}_s$ and is determined by the external flow only.

We use the pressure profiles to examine vesicles at the same effective extension Eq. (2.14) but different flow types. We keep the effective extension constant rather than the scaled capillary number (Eq. (2.15)) because our simulations have shown that vesicles in close to shear flows do not always align with the exit streamline. We simulate at $\alpha = [0.125, 0.500, 1.000]$, $\nu = 0.65$, $\lambda = 1.00$, and an effective capillary number (Eq. (2.14)) of 3.00. These parameters result in an "S"-like stationary shape at $\alpha = 0.125$ but a symmetric shape at $\alpha = 0.500$ and 1.000. To determine how a shape perturbation affects the internal pressure profile, we examine the pressure difference between the perturbed and stationary configurations. The perturbed pressure profile is measured at times $\sim 0.1/\dot{\epsilon}$ after perturbation to allow transient effects to dissipate and allow the profile to approximate that of the most unstable mode. For an unstable parameter set, we expect the total pressure ($p = p_B + p_U$) difference profile to give an internal flow that increases the perturbation — in other words, be positive on the
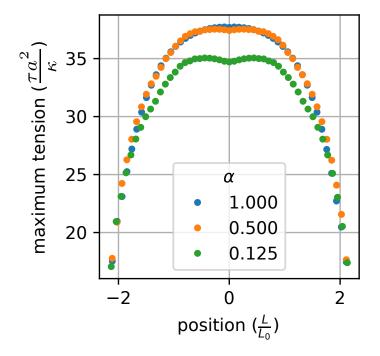
Figure 2.10. Stationary shape maximum tension profile for the pressure difference simulations. Note also non-dimensionalized by bending modulus (see Fig. 2.7). $\mathrm{Ca_{eff}} \approx 3.00$, $\lambda = 1.00$, $\nu = 0.65$

left half of the vesicle and negative on the right for the schematic in Fig. 2.9. We observe for all simulations that the bending contributions p_B are stabilizing while the flow contributions p_U are destabilizing, which is as expected.

Our calculations show that the pressure difference profiles for $\alpha = 0.5$ and $\alpha = 1.0$ vesicles are very similar, which is further confirmation that flow types not close to shear can be explained by the previously proposed scaling. For the close to shear flow case ($\alpha = 0.125$) however, the total pressure profile shows a stable configuration, suggesting an increased stability at the same effective capillary number. The increased external flow vorticity here results in a decreased destabilizing external flow contribution and a slightly altered bending contribution. One can see from Fig. 2.10 that the tension profile for $\alpha = 0.125$ shows lower values, suggesting that the altered external flow contribution originates from this decreased tension since $\Delta p_U \sim \sigma \Delta H$ [31]. It is interesting that the stabilizing effect from the shape deviations or their interaction with the sinusoidal perturbation is due to changes in flow forces rather than bending forces. This indicates that if such "S"-like shapes exist for other soft membrane systems like red blood cells, a similar mechanism may occur to describe their stability in flow, even if the membrane mechanics are more closely dominated by shear elasticity than bending. This shape deviation may also be a major factor in why red blood cells and other similar cellular systems have not been observed to breakup in shear flows even with large strain rates. It would be interesting to test these conjectures through simulations and experiments.

2.5   Conclusions

We have used a boundary element method to evaluate the stability of deflated vesicles in general linear flows. Our simulations agree with previous literature results for planar extensional flow. After introducing the rotational flow component, we observe that most of the mixed flow phase space can be explained by a scaled extensional rate — i.e., a scaled capillary number $\mathrm{Ca}_s = \sqrt{\alpha}\mathrm{Ca}$, where α is the flow parameter defined in Eq. (2.4) and Ca is a bending capillary number. For $\alpha \geq 0.500$, vesicles at the same scaled capillary number Ca_s have nearly the same shape and tension profile for the simulated viscosity ratios (0.01 to 5.00)

and reduced volumes (0.60 to 0.70). This is because the vesicles all align very closely with the exiting streamline, and the vesicle's internal flows do not stretch the material elements in the membrane appreciably. In this regime, one can accurately quantify the shape and stability of vesicles for a wide range of flow types and viscosity ratios using the results from an equiviscous vesicle under pure extension [31].

For flows close to pure shear flow ($\alpha \leq 0.25$), we observe that vesicle stability depends significantly on flow type and viscosity ratio, with the critical capillary number diverging at pure shear flow ($\alpha = 0$). In this flow regime, vesicles develop an "S"-like shape and exhibit lower tensions at similar effective extension rates. We note that the presence of such "S"-like shapes depend on the internal viscosity of the vesicle and only occur if the viscosity ratio is not too large, which explains why this parameter plays a crucial role in this regime. It will be interesting to know if such ideas hold for other soft membrane systems like red blood cells, where the membrane mechanics are more closely dominated by shear contributions rather than bending.

2.6   Acknowledgments

3. VESICLE DYNAMICS IN LARGE AMPLITUDE OSCILLATORY EXTENSIONAL FLOW

3.1   Summary

Although the behavior of fluid-filled vesicles in steady flows has been extensively studied, far less is understood regarding the shape dynamics of vesicles in time-dependent oscillatory flows. Here, we investigate the nonlinear dynamics of vesicles in large amplitude oscillatory extensional (LAOE) flows using both experiments and boundary integral (BI) simulations. Our results characterize the transient membrane deformations, dynamical regimes, and stress response of vesicles in LAOE in terms of reduced volume (vesicle asphericity), capillary number (Ca, dimensionless flow strength), and Deborah number (De, dimensionless flow frequency). Results from single vesicle experiments are found to be in good agreement with BI simulations across a wide range of parameters. Our results reveal three distinct dynamical regimes based on vesicle deformation: pulsating, reorienting, and symmetrical regimes. We construct phase diagrams characterizing the transition of vesicle shapes between pulsating, reorienting, and symmetrical regimes within the two- dimensional Pipkin space defined by De and Ca. Contrary to observations on clean Newtonian droplets, vesicles do not reach a maximum length twice per strain rate cycle in the reorienting and pulsating regimes. The distinct dynamics observed in each regime result from a competition between the flow frequency, flow time scale, and membrane deformation timescale. By calculating the particle stresslet, we quantify the nonlinear relationship between average vesicle stress and strain rate. Additionally, we present results on tubular vesicles that undergo shape transformation over several strain cycles. Broadly, our work provides new information regarding the transient dynamics of vesicles in time-dependent flows that directly informs bulk suspension rheology.

3.2 Introduction

In recent years, fluid-filled vesicles have been used in a wide array of technological applications ranging from food products to bioinspired microreactors, and reagent delivery applications in functional materials [76]. Moreover, giant vesicles are widely regarded as a model membrane system in various biophysical and biochemical processes [7], [10]. In these applications, precise characterization of the membrane shape dynamics in response to a fluid flow is of fundamental importance. Despite the increasing prevalence of vesicles in biophysics and materials science, we lack a complete understanding of how time-dependent flows influence the membrane shape dynamics and overall rheological response of vesicle suspensions [16], [29]. Lipid vesicles consist of a small amount of fluid enclosed by a bilayer membrane of thickness ≈ 5 nm. This molecularly thin membrane enables intriguing morphological dynamics for vesicles, including complex conformations in linear flows [23], [33], [34], [48], non-linear stretching behavior, and heterogeneous relaxation following deformation [36], [77], [78].

Recent advances in experiments, computations, and theory have largely focused on vesicle dynamics in steady shear flows [16]. These studies have revealed three dynamical regimes: tumbling, trembling, and tank-treading. Relevant research in shear flow includes investigation of the hydrodynamic lift of a single vesicle near a wall [79]–[81], pair interactions between two vesicles [30], [82], the amplification of thermal fluctuations in the transition regime between tumbling and tank treading [83]–[85], and characterization of tank-treading, vacillating-breathing (trembling), and tumbling motion with increasing viscosity ratio between the interior and the exterior of the vesicle [20]–[25]. The phase diagrams of the dynamical regimes in simple shear flow have been well analyzed over a number of studies, and the theory agrees well with experiments and simulations [22], [26]–[28] Knowledge of single vesicle dynamics has been essential for interpreting the bulk rheological response for dilute vesicle suspensions. For instance, it is now known that the tank-treading to tumbling behavior of vesicles directly affects the bulk viscosity of the suspension, where tumbling results in a higher bulk viscosity with the minimum bulk viscosity occurring at the tank-treading to tumbling transition [29].

Compared to the vast body of experiments in shear flows, vesicle dynamics in hyperbolic flows even for the canonical case of steady elongational flow are more challenging to understand. In extensional flow, fluid elements separate exponentially in time [86], and it is generally not possible to observe a single vesicle in flow for long periods of time in the absence of feedback controllers. Automation in flow control techniques using sophisticated feedback algorithms has recently enabled the precise characterization of vesicle dynamics in elongational flows [87]–[91]. In a steady extensional flow, it is known that highly deflated tubular vesicles undergo a conformation change to a symmetric dumbbell shape [30]–[33] while moderately deflated vesicles transition to an asymmetric dumbbell shape [33], [34]. Precise control over the center-of-mass position of single vesicles led to detailed studies of the transient and steady-state stretching dynamics of membranes [33], and direct observation of the double-mode relaxation following high deformation [36]. Prior work in unsteady flows has been limited to a one-time reversal of elongational flow and reported membrane wrinkling shapes for quasi-spherical vesicles [92].

Extensional flows are commonly encountered in microfluidic devices that utilise contractions or expansions, porous media, and other complex channel geometries. Moreover, *in vivo* capillaries and complex microfluidic devices that have many bifurcations and sharp directional changes routinely encounter time-dependent pulsatile flows. The biomedical community has created several biomimetic capillary designs that contain several rows of bifurcations and contractions with small angle zigzags in between, resulting in improved flow control and lower fluid flow resistance [93], [94]. In general, elastic particles traversing through these fluidic systems experience spatially dependent external flows and will not reach a steady-state conformation. From this view, there is a need for comprehensive studies on how microscopic stretching and compression of vesicles in complex, time-dependent oscillatory flows will affect their shape and bulk rheology.

Recently, the shape dynamics of elastic capsules were studied numerically in large amplitude oscillatory extensional (LAOE) flow [95]. However, the non-equilibrium stretching and compression dynamics of lipid vesicles in LAOE flows is largely unexplored. Vesicle dynamics are strongly governed by membrane bending elasticity; therefore, we anticipate that vesicles will exhibit qualitatively different behavior than capsules in time-dependent

51

extensional flow. In this paper, we study the dynamics of single vesicles in LAOE using a combination of microfluidic experiments and boundary integral (BI) simulations. LAOE experiments are performed using the Stokes trap [87]–[90], which is a new method for controlling the center-of-mass position, orientation and trajectories of freely suspended single and multiple vesicles using only fluid flow. We find that single vesicles experience periodic cycles of compression and extension in LAOE with membrane dynamics governed by the dimensionless flow strength Capillary number (Ca), reduced volume (measure of vesicle asphericity, ν) and flow frequency Deborah number (De). Experimental results are compared to BI simulations without thermal fluctuations, and our results show that BI simulations accurately capture the dynamics of single quasi-spherical vesicles over a wide range of parameters. In addition, we identify three distinct dynamical regimes for vesicle dynamics, including the pulsating, reorienting, and symmetrical regimes, based on the amount of deformation occurring in each half cycle of the LAOE flow. The qualitatively different dynamics observed in each regime results due to a competition between the flow frequency, flow time scale, and membrane deformation timescale. We further construct precise phase diagrams characterizing the transition of vesicle shapes between pulsating, reorienting, symmetrical regimes. We find that the relationship between average vesicle stress and strain rate is nonlinear, which is discussed in the context of bulk suspension rheology. Finally, we present results on the shape dynamics of long tubular vesicles in LAOE which exhibit markedly different behavior in flow compared to their quasi-spherical analogues. Taken together, our results provide new insights into the direct observation of membrane dynamics during time-dependent oscillatory flows, which opens new avenues for understanding bulk suspension rheology in unsteady flows.

3.3 Methods

3.3.1 Vesicle preparation

A mixture of 1,2-dioleoyl-sn-glycero-3-phosphocholine (DOPC, Avanti Polar Lipids) and 0.12 mol% of 1,2-dioleoyl-sn-glycero-3-phosphoethanolamine-N-(lissamine rhodamine B sulfonyl) (DOPE-Rh, Avanti Polar Lipids) is used to generate giant unilamellar vesicles (GUVs)
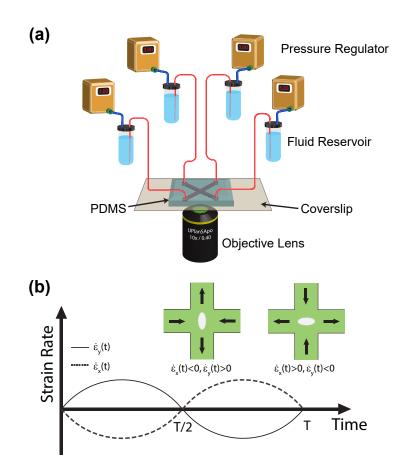
Figure 3.1. Stokes trap for studying vesicle dynamics in large amplitude oscillatory extensional (LAOE) flow. (a) Schematic of the experimental setup used to generate planar extensional flow. Inlet/outlet channels in the microfluidic device are connected to fluidic reservoirs containing the vesicle suspension and pressurized by regulators controlled by a custom LabVIEW program, thereby generating pressure-driven flow in the cross-slot. (b) Schematic of the sinusoidal strain rate input function for one full cycle. Inset: schematics showing the oscillatory extensional flow profile in the microfluidic cross-slot device during the first half $(0 < t < T/2)$, and second half period $(T/2 < t < T)$ of the cycle.

with the electroformation process described by [96]. For electroformation of GUVs, a stock lipid solution in chloroform is prepared with 25 mg/mL DOPC and 0.04 mg/mL DOPE-Rh for fluorescent imaging. Next, 10 μL of the lipid solution in chloroform is spread on a conductive indium tin oxide (ITO) coated glass slide (resistance 5 Ω, 25×50×1.1 mm, Delta Technologies) and dried under vacuum overnight. The pair of ITO slides are sandwiched together using a 1.5 mm Teflon spacer, forming a chamber with a volume of $\approx$ 2.4 mL and coupled to a function generator (Agilent 33220 A). The electroformation chamber is filled with a mixture of 100 mM sucrose solution (Sigma-Aldrich), and glycerol-water is added to achieve a total viscosity of 0.030 Pa-s measured using a benchtop viscometer (Brookfield) at 22°C. An alternating current (AC) electric field of 2 V/mm is then applied at 10 Hz for 120 min at room temperature (22°C). Under these conditions, DOPC lipid remains in the fluid phase [24]. Most of the vesicles prepared by this method are quasi-spherical and unilamellar with few defects in the size range of 5–25 μm in radius.

3.3.2 Stokes trap for large amplitude oscillatory extension

It is challenging to observe vesicle dynamics in time-dependent extensional flow for long periods of time while simultaneously imposing precisely controlled flow rates. To achieve this, we used the Stokes trap [87], [89] to precisely position the center-of-mass of single vesicles near the center of a cross-slot microfluidic device for long times using model predictive control (Fig. 3.1a). Briefly, the centroid of a single vesicle is determined in real-time using image processing and fluorescence microscopy and is communicated to the controller. The controller determines the optimal flow rates through four-channels of the device to maintain a fixed vesicle position with desired strain rate. The flow rates are then applied through four independent pressure regulators (Elveflow). During this process, the device operates at a net positive pressure so that each of the four ports can act as inlet or outlet. This whole procedure requires $\approx$ 30 ms in a single cycle, as previously described [87], [97], [98]. In this

work, a sinusoidal strain rate input is imposed (Fig. 3.1b) while simultaneously trapping a single vesicle such that:

$$\dot{\epsilon}_x(t) = -\dot{\epsilon}_0 \sin\left(\frac{2\pi}{T}t\right) \tag{3.1}$$

$$\dot{\epsilon}_y(t) = \dot{\epsilon}_0 \sin\left(\frac{2\pi}{T}t\right) \tag{3.2}$$

where T is the period of the sinusoidal cycle and $\dot{\epsilon}_0$ is the maximum strain rate in one cycle. During the first half-cycle for $0 < t < T/2$, the x-axis is the compressional axis and y-axis is the elongational axis ($\dot{\epsilon}_x(t) < 0, \dot{\epsilon}_y(t) > 0$), and the fluid is delivered from the two horizontal inlets of the microfluidic device by the pressure regulators (Fig. 3.1b). During the second half-cycle for $T/2 < t < T$, the direction of flow reverses, and fluid is delivered by the two vertical ports in the cross-slot device as shown in Fig. 3.1b. We note that during vesicle trapping, the correctional pressure required for controlling the vesicle's position is small compared to the magnitude of the base pressure used to generate the oscillatory extensional flow [87]. Thus, the strain rate is well defined during the LAOE cycle, which is determined as a function of the input pressure using particle tracking velocimetry (PTV) as previously described [33]. We also determined the characteristic response time for actuating fluid flow in the microfluidic device in response to a step change in pressure. For an extreme change in pressure from 0 to 4 psi (strain rate jump from 0 to $\sim 30~s^{-1}$), the rise time and settling time are $\sim$20 ms and $\sim$300 ms respectively (Fig. S1). However, the maximum value of pressure used in our experiments is 0.4 psi, which is continuously varied with small incremental changes during the LAOE cycle, for which we generally expect much smaller characteristic response times. Nevertheless, the lowest cycle time T in our experiments is 2 seconds which is much larger than the maximum characteristic response time for actuating flow in the device corresponding to a step input pressure.

For all experiments, single vesicles are first trapped and imaged for 10–30 s under zero flow conditions to allow for equilibration, followed by LAOE flow for at least 2 strain rate cycles. During the equilibration step, the vesicle reduced volume ν and equivalent radius

a are determined, as previously described [33], [34]. Reduced volume ν is a dimensionless quantity that measures the amount of osmotic deflation, and is described as:

$$\nu = \frac{3V\sqrt{4\pi}}{A^{3/2}} \tag{3.3}$$

where V and A are the vesicle volume and surface area, respectively. The equivalent radius a of the vesicle is obtained as $a = \sqrt{A/4\pi}$. Specifically, ν is a measure of vesicle asphericity such that $\nu = 1$ represents a perfectly spherical shape. For the experiments in Sections 3.4.1, 3.4.2, 3.4.4 and 3.4.5, the typical range of reduced volume is $0.75 < \nu < 1$, while vesicles in Section 3.4.6 have $\nu < 0.75$.

The maximum strain rate $\dot{\epsilon}_0$ experienced by a vesicle in a half-cycle is non-dimensionalized to define a capillary number $\mathrm{Ca} = \mu_{out}\dot{\epsilon}_0 a^3/\kappa$ where μ_{out} is the suspending medium viscosity, a is the equivalent vesicle radius, and κ is the membrane bending modulus. Prior to vesicle experiments in LAOE flow, we determined the average bending modulus of nearly spherical vesicles to be $\kappa = (22.3 \pm 0.5)k_B T$ using contour fluctuation spectroscopy [33]t Similarly, the cycle period is rendered dimensionless by the bending time scale to define the Deborah number $\mathrm{De} = \mu_{out} a^3/\kappa T$. Single vesicle experiments are generally performed in the range $10 < \mathrm{Ca} < 1000$ and $0.1 < \mathrm{De} < 100$ by adjusting the input pressures and strain rate cycle periods. Only vesicles near the center plane of the microchannel (with respect to the z-direction) are considered during experiments. Single vesicle trajectories are analyzed using a custom MATLAB program that allows for determination of the vesicle deformation parameter in flow.

3.3.3 Numerical methods

Governing equations and non-dimensionalization

The system is modeled as a droplet surrounded by a two-dimensional incompressible membrane with a bending resistance. At the length scale of a GUV ($a \approx 10~\mu$m) with a strain rate at $\dot{\epsilon} \approx 1~s^{-1}$ the Reynolds number is $\mathrm{Re} = \dot{\epsilon}\rho a^2/\mu \approx 10^{-4}$, allowing us to model the inner and outer velocity fields using the Stokes equations. Due to the nature of the

time-dependent flow, it is also important to check the Womersley number to assess whether the time-dependent Stokes equations are required. At a flow frequency of $\omega = 10 \ s^{-1}$, the Womersley number is $\alpha = \sqrt{\omega \rho a^2 / \mu} \approx 0.03$. In this work, the flow frequencies are $\omega < 10$ s^{-1}, therefore the time-dependent Stokes equations are not necessary. The Stokes equations are:

$$\nabla \cdot \boldsymbol{u} = 0, \quad \nabla p = \mu \nabla^2 \boldsymbol{u}. \tag{3.4}$$

where $\boldsymbol{u}$ is fluid velocity, p is the pressure, and μ is the fluid viscosity (μ_{in} for the inner fluid and μ_{out} for the outer fluid). The system is subject to continuity of velocity across the interface and a traction balance across the phospholipid bilayer. The short timescales and low deformation rates used in previous studies makes membrane dilatation negligible [17], [37]. Vesicles are also known to have negligible shear rigidity as they do not have a cytoskeletal network or an actin cortex. We therefore use the Helfrich model [15] for the membrane:

$$\mathbb{H} = \oint \frac{\kappa}{2} (2H)^2 dA + \oint \sigma dA. \tag{3.5}$$

In Eq. (3.5), $\mathbb{H}$ represents the elastic energy of the vesicle membrane, κ is the membrane bending modulus, H is the mean curvature, and σ is the surface tension. The surface tension is a spatially varying Lagrange multiplier that ensures local area conservation. The surface tension enforces $\nabla_s \cdot \boldsymbol{u} = 0$ on the interface, where $\nabla_s = (\boldsymbol{I} - \boldsymbol{nn}) \cdot \nabla$. We note that the original Helfrich model includes spontaneous curvature, a parameter to describe a membrane's curvature preference when the sides of the bilayer are chemically different. Although biological vesicles may have multiple lipid components or chemical differences between the inner and outer fluids [18], [67], [68], our experiments focus on simple vesicles with only a viscosity difference between the inner and outer fluids, prompting a negligible spontaneous curvature. We further neglect contributions from thermal fluctuations, membrane viscosity, and bilayer friction [19], [38].

The force balance at the membrane surface is:

$$[[\boldsymbol{f}]] = [[\boldsymbol{T} \cdot \boldsymbol{n}]] = \boldsymbol{f}_t + \boldsymbol{f}_b \tag{3.6}$$

$$\boldsymbol{f}_t = (2H\sigma\boldsymbol{n} - \nabla_s\sigma) \tag{3.7}$$

$$\boldsymbol{f}_b = \kappa(4KH - 4H^3 - 2\nabla_s^2 H)\boldsymbol{n} \tag{3.8}$$

where $[[\boldsymbol{f}]]$ is the jump in viscous traction across the interface which can be decomposed to the bending ($\boldsymbol{f}_b$) and tension ($\boldsymbol{f}_t$) contributions, $\boldsymbol{n}$ is the outward-pointing unit normal vector, and K is the Gaussian curvature of the interface. The mean curvature H is defined to be one for the unit sphere.

The vesicle is placed in a time-dependent extensional flow field described by $\boldsymbol{u}^\infty = \nabla\boldsymbol{u}^\infty \cdot \boldsymbol{x}$ and defined as:

$$\nabla\boldsymbol{u}^\infty = \dot{\epsilon}_0 \begin{bmatrix} -\sin(2\pi\omega t) & 0 & 0 \\ 0 & \sin(2\pi\omega t) & 0 \\ 0 & 0 & 0 \end{bmatrix} \tag{3.9}$$

where ω is the frequency of the oscillatory flow and $\dot{\epsilon}_0$ is the maximum strain rate.

The membrane area (A) is maintained constant by the incompressibility constraint while the low permeability of the membrane allows us to assume that the volume (V) of the vesicle is constant during the timescale of experiments (minutes). Therefore, we non-dimensionalize distances by the equivalent radius $a = \sqrt{A/(4\pi)}$, time scales by $\kappa/a^3\mu_{out}$, velocities by $\kappa/a^2\mu_{out}$, stresses by κ/a^3, and surface tensions by κ/a^2. We obtain four relevant dimensionless groups from the non-dimensionalization:

$$\text{Ca} \equiv \frac{\mu_{out}\dot{\epsilon}_0 a^3}{\kappa}, \quad \text{De} \equiv \frac{\omega a^3 \mu_{out}}{\kappa}$$

$$\lambda \equiv \frac{\mu_{in}}{\mu_{out}}, \quad \nu \equiv \frac{3V}{4\pi a^3} \tag{3.10}$$

These parameters were previously described in Section 3.3.2 and are elaborated upon here. The base capillary number (Ca) compares the viscous stress to the bending stress and corresponds to the non-dimensionalized, maximum extension rate experienced by the vesicle during the flow cycle. De is the flow frequency non-dimensionalized by the bending timescale.

When De $\gg 1$, the fluid flow will have a short cycle time compared to the membrane's bending time. The viscosity ratio (λ) is the ratio of inner and outer fluid viscosities. Cellular systems such as red blood cells (RBCs) commonly have a more viscous inner fluid, and this parameter can be tuned to more closely model the system of choice. The reduced volume (ν) is a measure of the asphericity of the vesicle, corresponding to its osmotic deflation. For example, a reduced volume of $\nu = 1$ corresponds to a perfectly spherical vesicle shape, while a value of $\nu = 0.2$ would be highly deflated. One can experimentally alter the reduced volume of a vesicle by introducing an osmotic pressure difference between the inner and outer membranes, for example by adding sucrose to the outer fluid.

Applying this non-dimensionalization, the external velocity gradient becomes:

$$\nabla \boldsymbol{u}^\infty = \mathrm{Ca} \begin{bmatrix} -\sin(2\pi \mathrm{De}\, t) & 0 & 0 \\ 0 & \sin(2\pi \mathrm{De}\, t) & 0 \\ 0 & 0 & 0 \end{bmatrix} \tag{3.11}$$

where all parameters are assumed to be non-dimensional from this point forward.

Boundary integral formulation

The Stokes flow assumption enables the use of the boundary integral (Green's function) formulation to simulate vesicle shape dynamics. The Stokes equations are recast into a boundary integral form:

$$\begin{aligned} \frac{1+\lambda}{2} u_j(\boldsymbol{x_0}) &= u_j^\infty(\boldsymbol{x_0}) - \frac{1}{8\pi} \int_S G_{ij}(\boldsymbol{x}, \boldsymbol{x_0})[[f_i]](\boldsymbol{x}) dA(\boldsymbol{x}) \\ &+ \frac{1-\lambda}{8\pi} \int_S T_{ijk}(\boldsymbol{x}, \boldsymbol{x_0}) u_i(\boldsymbol{x}) n_k(\boldsymbol{x}) dA(\boldsymbol{x}) \end{aligned} \tag{3.12}$$

where u_i^∞ is the external velocity field, $\boldsymbol{x_0}$ is the singularity point, and $[[f_i]]$ is the jump in viscous traction across the interface, given in Eq. (3.8). The kernels $G_{ij}(\boldsymbol{x}, \boldsymbol{x_0})$ and $T_{ijk}(\boldsymbol{x}, \boldsymbol{x_0})$ are the Stokeslet (point force) and stresslet (point dipole) solutions to Stokes flow:

$$G_{ij}(\boldsymbol{x}, \boldsymbol{x}_0) = \frac{\delta_{ij}}{r} + \frac{\tilde{x}_i \tilde{x}_j}{r^3} \tag{3.13}$$

$$T_{ijk}(\boldsymbol{x}, \boldsymbol{x}_0) = -6\frac{\tilde{x}_i\tilde{x}_j\tilde{x}_k}{r^5} \tag{3.14}$$

where $\tilde{\boldsymbol{x}} = \boldsymbol{x} - \boldsymbol{x}_0$ and $r = |\tilde{\boldsymbol{x}}|$. Repeated indices are assumed to be summed in the above equations. These equations are also subject to the membrane incompressibility constraint:

$$\nabla_s \cdot \boldsymbol{u} = 0 \tag{3.15}$$

Implementation details

Implementation details for the simulations are similar to prior work [48]. Here, we re-iterate how some aspects are handled and highlight a few key differences. We solve the BEM system with the general minimal residual method (GMRES) in parallel using PETSc over the message passing interface (MPI). The curvature of the surface is approximated by a subdivision surface [35], [44]. Integrals over the triangular elements are evaluated using Gaussian quadrature, where singular elements are handled by using the Duffy quadrature rule for singular kernels [99]. We use a timestepping procedure that is equivalent to the one in [47]. The surface incompressbility constraint is enforced by the Lagrange multiplier σ, which is locally determined with each timestep. The constant volume constraint is inherently enforced by the Stokes flow assumption for the inner and outer fluids, but the timestepping procedure used for the surface positions can still give a slight drift in volume over long times ([47]). We use a scaling procedure with an arbitrary relaxation parameter of 0.1 that limits the scaling such that the correction is not immediately applied but rather applied over several timesteps to keep the volume consistent. Graphs showing the surface area and volume error are shown in the supplementary information (Fig. S11). These errors oscillate and the maximum surface area errors are below 0.1% while the maximum volume errors are below 0.2%.

For meshing the vesicle, we start with an icosahedron and subdivide the mesh into 1280 elements for a quasi-spherical vesicle; 5120 elements for the tubular vesicles. In the following sections, we analyze the deformation parameter of the vesicles; we found the 1280 element mesh to be sufficiently accurate capturing this information. A figure comparing the deformation parameter over several flow cycles for the 1280 element mesh and a 9680 element

mesh is in the supplementary materials (Fig. S12). We tested mesh sizes from 720 elements to 9680 elements and found no significant difference in the deformation parameter over the flow cycles between them. However, the 1280 element mesh used does not accurately resolve the wrinkling dynamics. Our implementation does not take into account thermal fluctuations, making it unlikely the simulations would accurately predict the wrinkling dynamics even with smaller element sizes. Therefore, we chose to use lower element meshes to reduce computation time.

To form the initial vesicle shape for our simulations, we use a scaling transformation on the subdivided icosahedron to deform the mesh into a prolate spheroid with the desired reduced volume ν, followed by relaxing the mesh to its equilibrium (no flow) configuration. In this way, the vesicle has a prolate spheroid-like shape at the start of any cycle. It is possible to start with an oblate spheroid or any arbitrary ellipsoid-like shape, but it has been shown that the global minimum energy state for a vesicle with reduced volume greater than 0.652 is of the prolate shape family[19]. After forming the initial vesicle shape, vesicle dynamics are simulated in oscillatory flow with a timestep of 10^{-3} strain units.

The majority of the analysis in this study is focused on vesicle behavior that has reached a steady limit cycle in time-dependent flow, such that the dynamics are the same regardless of the number of additional strain rate cycles. The startup dynamics have been simulated but are not elaborated on in this paper. We simulate vesicles of reduced volumes between $0.60 < \nu < 0.90$ and viscosity ratios $\lambda = 0.1, 1.0$, and 10 for flows with capillary numbers $1 < \text{Ca} < 80$ and Deborah numbers $1 < \text{De} < 10$. Significantly higher capillary numbers (Ca $\gtrsim 200$) become numerically intractable as the timestep needed for convergence in our implementation becomes prohibitively small. Higher and lower De can be simulated, but the current range of values is sufficient for comparison to the majority of experimental conditions for GUVs in microfluidic devices.

We define the parameter:

$$\text{Ca}_x(t) \equiv -\text{Ca}\sin(2\pi\text{De} \cdot t) \tag{3.16}$$

which represents the time-dependent capillary number in the x-direction. This will be the measure used for the instantaneous strain rate. We also define a deformation parameter:

$$D \equiv \frac{l_x - l_y}{l_x + l_y} \tag{3.17}$$

where l_x and l_y are the x- and y-axis lengths of the vesicle respectively, or the length of the axes of the equivalent ellipsoid. In the experiments, l_x and l_y are computed from the vesicle microscopy movies using a custom image processing algorithm as described in [98] and [33]. For the simulations, the lengths of the vesicle in the x- and y-axes are computed. The deformation parameter (D) provides a measure of vesicle shape distortion. For D values near zero, the vesicle shape projected in the x-y plane will be circular. Positive values of $D \approx 0.50$ correspond to prolate spheroid like shapes along the x-axis, while negative values correspond to the same shapes along the y-axis.

3.4 Results and Discussion

3.4.1 Dynamical regimes
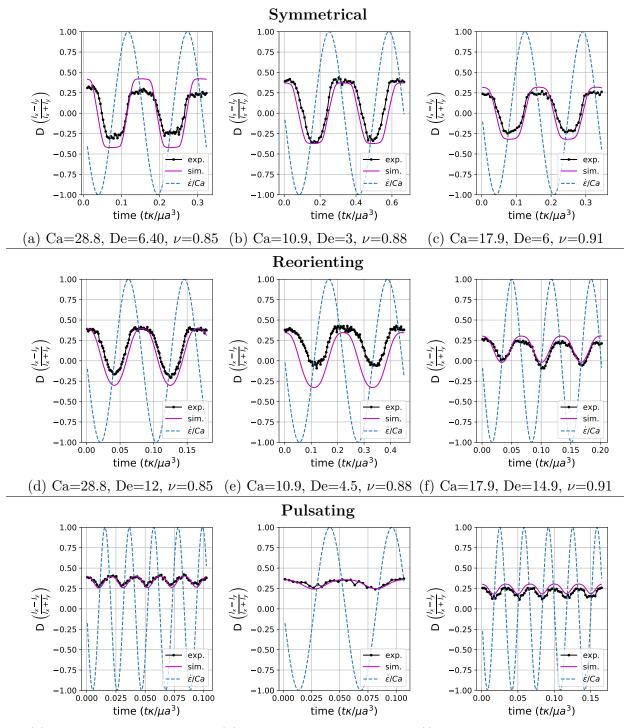
Experiments were performed in the range of approximately $10 < \text{Ca} < 1000$ and $0.5 < \text{De} < 100$, whereas the majority of the simulations are in the range of $1 < \text{Ca} < 40$ and $1 < \text{De} < 10$. Simulations were performed for several vesicles matching the conditions in the experiments, as discussed in the following section (Fig. 3.2, Fig. 3.3 and Fig. 3.4). It is possible to perform additional simulations at $\text{Ca} \approx 100$, but current results suggest that the vesicle dynamics do not significantly change at higher Ca for quasi-spherical vesicles.

We observe three dynamical regimes of vesicle dynamics based on the ratio between Capillary number and Deborah number. We refer to these regimes as symmetrical, reorienting, and pulsating. The transitions between these regimes are continuous — in other words, there is no bifurcation between the regimes in the sense that the dynamics change suddenly. We define the regimes based on the deformation characteristics of vesicles in each case: symmetrical when the vesicle deforms to the same length in both orientations, pulsating when the vesicle's major axis stays along the same orientation, reorienting for the region between

symmetrical and pulsating where the vesicle major axis changes orientation but does not deform to the same maximum length in both directions. Vesicles in all three regimes can experience significant non-linear stress responses. Snapshots of vesicle shapes from simulations and experiments for each of these regimes over a full strain rate cycle are shown in Fig. 3.5 and Fig. 3.6.

We quantitatively compare the simulations and experiments by plotting the deformation parameter D (defined in Eq. (3.17)) and instantaneous strain rate Ca_x (defined in Eq. (3.16)) as a function of time, as shown in Figs. 3.2 and 3.3. Experimental trajectories are generally limited to 2–4 strain rate cycles due to the photobleaching of the vesicle membrane during fluorescence imaging experiments. Observing vesicle deformation over more strain rate cycles is experimentally feasible, however, we generally opted to observe dynamics under different experimental parameters (Ca, De) for the *same vesicle* in a series of subsequent experiments. For the numerical data, we simulated vesicle dynamics over at least 10 strain rate cycles.
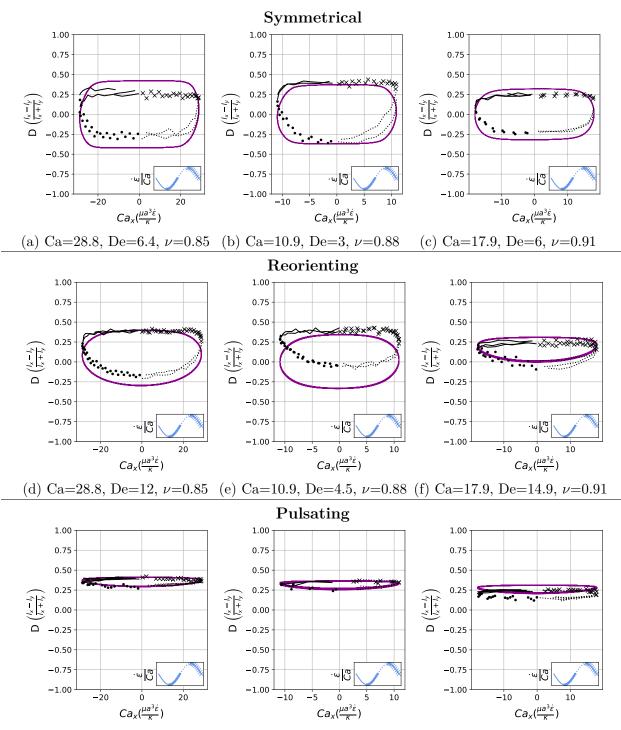
Symmetrical regime:

Starting with the symmetrical regimes results, we find the symmetrical regime occurs under flow conditions where the vesicle deformation timescale is shorter or exactly equal to half of a strain rate cycle. Based on our simulations, this occurs approximately when Ca $\geq$ 3.33 De for a vesicle with a reduced volume $\nu = 0.80$. Our experiments and simulations show that vesicle dynamics in the symmetrical regime are described by two common characteristics (Fig. 3.4). First, the vesicle reaches approximately the same maximum length twice during one strain rate cycle, regardless of Ca. The observation of a maximum length is reasonable for quasi-spherical vesicles, as it has been shown that vesicles with $\nu > 0.75$ have a stable steady-state shape at infinite Ca, regardless of viscosity ratio [31]. Second, vesicle membranes exhibit transient wrinkling when vesicles are exposed to the compressional cycle of the oscillatory extensional flow. The transient wrinkling behavior is examined later in this section. These features are illustrated in Fig. 3.4, where a characteristic time series of images of vesicle shape in LAOE is qualitatively compared to the equivalent numerical simulation. In general, vesicle shapes determined from experiments are in good agreement with those determined

63

Symmetrical

(a) Ca=28.8, De=6.40, ν=0.85 (b) Ca=10.9, De=3, ν=0.88 (c) Ca=17.9, De=6, ν=0.91

Reorienting

(d) Ca=28.8, De=12, ν=0.85 (e) Ca=10.9, De=4.5, ν=0.88 (f) Ca=17.9, De=14.9, ν=0.91

Pulsating

(g) Ca=28.8, De=48, ν=0.85 (h) Ca=10.9, De=18.2, ν=0.88 (i) Ca=17.9, De=29.9, ν=0.91

Figure 3.2. Transient deformation parameter D for vesicle dynamics in time-dependent LAOE from experiments and simulations. All vesicles have a viscosity ratio of $\lambda = 1.0$. The $\dot{\epsilon}/\text{Ca}$ line is the instantaneous strain rate of the external flow along the x-axis. A negative $\dot{\epsilon}/\text{Ca}$ value is compression along the x-axis.

Figure 3.3. Lissajous-type curves of the deformation parameter D versus the dimensionless instantaneous strain rate. All vesicles have a viscosity ratio of $\lambda = 1.0$. Black data points are experimental data; purple data points show numerical data. The oscillatory strain rate cycle is separated into four parts that have been noted with different markers, as shown in the legend in the bottom right hand corner.
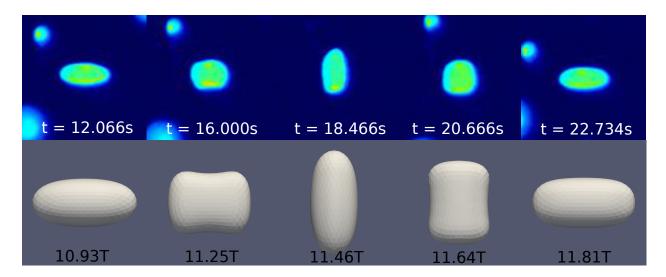
Figure 3.4. Comparison of the experimental and simulation vesicle shapes in the symmetrical regime over one flow cycle at the same conditions of Ca = 10.9, De = 3.0, ν = 0.88, λ = 1.00. The times in the figure are in seconds for the experimental video. Shapes from the simulations at the same non-dimensional cycle times are shown below. T is the non-dimensional period, defined as $T = 1/$De.

from numerical simulations. Turning to the deformation parameter plots (Fig. 3.2 and Fig. 3.3), we see the simulations and experiments agree well at the majority of the tested parameters. Some of the experimental datasets show fluctuations in the deformation over the strain rate cycles and disagreement between the simulations on the maximum deformation. These discrepancies likely occur due to challenges in imaging a three-dimensional object in a two-dimensional plane and because the experiments are limited to a few strain rate cycles. Nevertheless, we generally observe good agreement between simulations and experiments in terms of the deformation parameter in transient flows.

Transient wrinkling dynamics were first reported by [92] for a single cycle of suddenly reversed extensional flow and subsequently elaborated upon by [100]. Wrinkling behavior is caused by a negative surface tension created during vesicle compression. Moreover, a critical compression rate exists below which thermal fluctuations dominate the observed wrinkling. In our work, we study vesicle dynamics in an extensional flow with smoothly varying sinusoidal strain rate dependence, rather than an abrupt step-function reversal of compressional/extensional axes. We observe qualitatively the same membrane wrinkling

features as those reported in prior work. In the experiments, we observe some wrinkling in the majority of the videos; it is unclear if this is from thermal fluctuations or the negative surface tension. In the simulations, we only observe significant wrinkling in the symmetrical regime. Our simulations do not take into account thermal fluctuations, therefore we hypothesize that the critical wrinkling strain rate required for a given flow frequency is only reached in the symmetrical regime. Additional experimental snapshots of vesicles showing wrinkling dynamics are included in the supplementary materials (Fig. S2, Fig. S3, Fig. S4 and Fig. S5).

Reorienting regime:

At lower Ca/De ratios (when Ca $\approx$ 2De for $\nu = 0.80$), the vesicle's major axis for orient along the x- and y-axes during the flow cycle, but the stretching along these axes will no longer be equal. The creates a deformation parameter that is negative during part of the cycle, but whose mean value is non-zero (Fig. 3.2d). We notes that prior work on droplets in oscillatory extensional flow do not observe this behavior, as only symmetrical deformation (i.e., equal deformation in the x- and y- orientations) has been reported regardless of flow strength and oscillatory frequency [101], [102] Single polymers in LAOE also deform symmetrically between the two half cycles for the range of Weissenberg and Deborah numbers studied in prior work [98]. The phenomenon of asymmetric stretching of vesicles along the two axes arises due to the enclosed membrane for fluid-filled vesicles. In particular, we posit that the asymmetrical deformation occurs because the energetically preferred shape for quasi-spherical vesicles at equilibrium is a prolate dumbbell [19]. By deforming in this asymmetrical manner, the vesicle shape deviates less from the equilibrium shape over the strain rate cycle than it would if it deformed symmetrically.
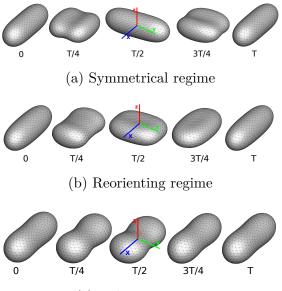
Pulsating regime:

At even lower Ca/De, the vesicle no longer reorients and simply pulsates along one axis during LAOE. We refer to this dynamical regime as the pulsating regime, which approximately occurs when Ca $\leq$ 2De for $\nu = 0.80$. Note that the strain in the pulsating regime is

67

not necessarily infinitesimal. As shown in Fig. 3.2g, the deformation parameter curve illustrates that vesicles are generally oriented along the x-axis and can deform significantly in this regime. It is possible to probe the small amplitude oscillatory extension regime by keeping the De constant and reducing the Ca. In the small amplitude regime, vesicles do not deform appreciably, and the Lissajous curve approaches a constant value, thereby informing on the linear viscoelastic rheology of vesicle suspensions. Similar behavior occurs when increasing the De and keeping Ca constant at small values. In this case, the membrane does not have appreciable time to reorient during the time at which the strain rate changes.

3.4.2 Quasi-spherical initial shape and orientation

The simulations discussed up to this point (including results in Fig. 3.5 and Fig. 3.2) were performed using a prolate-like initial shape, because it is the global equilibrium shape for reduced volumes $\nu \geq 0.652$ [19]. These results suggest that the unequal stretching observed in the pulsating and reorienting regimes occurs during the steady limit cycle, for this particular initial shape. However, there are other local minimum energy shapes for vesicles, such as the oblate shape family. To determine whether the pulsating and reorienting regimes are possible with a different initial condition, we performed simulations using an oblate shape such that the initial deformation parameter was set to zero. We examined this initial condition because vesicle shape is isotropic in the x-y plane, where an image obtained through optical microscopy would show a circle. The oblate initial condition simulations test if the anisotropic deformations will still occur if the vesicle starts with a shape isotropic in the x-y plane rather than an initially anisotropic shape. Simulation results for the oblate initial condition are plotted in Fig. 3.7, which shows that vesicle dynamics during the steady limit cycle for the oblate initial condition (Fig. 3.7a) are the same as that observed from the prolate-like initial condition (Fig. 3.7b). We repeated these simulations at several other capillary numbers and Deborah numbers, observing no change in the dynamics.

We additionally examined different starting orientations of the prolate initial shape. Aligning the prolate vesicle with the y-axis instead of the x-axis does not change the dynamics significantly. The symmetrical regime remains unchanged, while the pulsating and

(a) Symmetrical regime

(b) Reorienting regime

(c) Pulsating regime

Figure 3.5. Snapshots of vesicle shapes from simulations over a flow cycle for the three dynamical regimes. The values under the figures are fractions of a strain rate period defined as $T = 1/\mathrm{De}$.
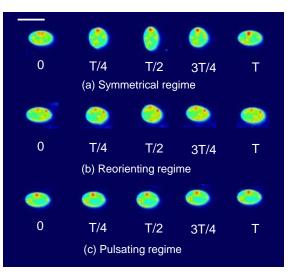
Figure 3.6. Snapshots of vesicle shapes from experiments over a flow cycle for the three dynamical regimes. The values under the figures are fractions of cycle time T in seconds. Scale bar is 20 μm. False color is applied to the grayscale images for enhancing the resolution.

(a) oblate initial   (b) prolate initial
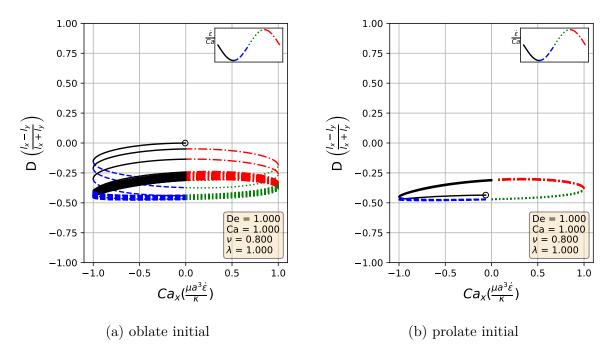
Figure 3.7. Lissajous type deformation parameter curves from an oblate shape initial condition and a prolate shape initial condition. Top right legend indicates color coding for the strain rate cycle. The black circle marks the deformation parameter of the initial shape.

reorienting regimes preferentially stretch along the y-axis instead of the x-axis. The observed dynamics change when aligning the prolate vesicle along the z-axis — i.e., orthogonal to the flow plane. At lower ratios of Ca/De, the vesicle deforms symmetrically while maintaining the major axis orientation along the z-axis. At higher ratios of Ca/De, the dynamics become the same as those observed in the symmetrical regime with other starting orientations. We also simulated vesicles at other out-of-plane orientations and found they can maintain their orientation at low ratios of Ca/De over 15 flow cycles. Simulation videos files of vesicle dynamics starting from the z-axis orientation and angled at 70 degrees between the x- and z-axes are included in the supplementary materials (movies 8–10).

Experimentally, we have not observed any of the dynamics suggested by the simulations with alternative starting orientations. It is unclear if these orientations are unstable to perturbation or if the experimental methods limit the possible orientations of the vesicles. One would need to use a microscopy method that can obtain z-axis information to better understand the effect of starting orientation.

3.4.3   LAOE analysis considerations

In regards to application of LAOE for vesicle analysis, we note that it may be possible to extract some material properties of the vesicle by LAOE analysis. One could fit the deformation parameter over time of an experimental run to that of a simulation to approximate an unknown parameter, such as the reduced volume or capillary number. There are significant error margins when approximating experimental parameters, such as reduced volume, so confirmation with LAOE could be beneficial. We have not tested the feasibility or accuracy of such a process in this study however.

3.4.4   Quasi-spherical phase diagrams

By comparing the deformation parameter results for each simulation, we can plot a phase diagram of different dynamical regimes observed during oscillatory flows. Which regime a vesicle experiences can be quantitatively determined by assessing the minimum and maximum deformation parameter over a cycle. If both the minimum and maximum deformation

71
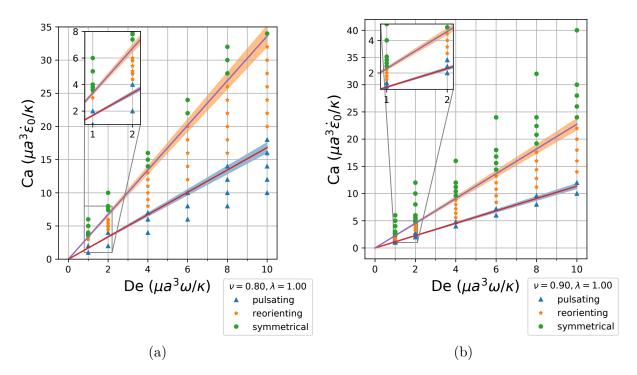
Figure 3.8. Phase diagrams for the low to medium to high deformation regimes for vesicles of reduced volume $\nu = 0.80$ and $\nu = 0.90$. Lines in the diagrams are from the semi-analytical theory presented near the end of Section 3.4.1. Due to uncertainty in determining the D_o value, a 5% error has been included on the lines.

parameter are positive, the vesicle dynamics are classified as the pulsating regime, reflecting that the vesicle does not change orientation. If the vesicle has a positive maximum D and a negative minimum D, we check if the differences in magnitudes are within a threshold value of 0.01. Should they be within 0.01 of each other, the vesicle is in the symmetrical regime, since the vesicle reaches the same maximum length twice a cycle. This threshold value was chosen heuristically to reflect the discretization accuracy. If the magnitudes are not within this threshold value, vesicle dynamics are classified as the reorienting regime. Results from this analysis is plotted in Fig. 3.8

The phase boundaries appear to be mostly linear, suggesting that the dynamics result from a simple interaction between the flow frequency and the strain rate, $\mathrm{Ca}/\mathrm{De} = \dot{\epsilon}_0/\omega$. Here, we derive the phase boundaries in the limit of a quasispherical vesicle [22]. For small excess area ($\Delta = 4\pi(\nu^{-2/3} - 1) \ll 1$), the vesicle shape is characterized by a perturbation

series in terms of spherical harmonics [22]. In a planar extensional flow, there are only two modes excited for the leading order correction to the vesicle shape. When one solves for the deformation parameter as defined in Eq. (3.17), one obtains

$$
\begin{aligned}
D(t) = (L_\infty - 1) \\
\left(1 - 2\left(1 + \left(\frac{1+A_o}{1-A_o}\right)\exp\left(\frac{60}{\pi(32+23\lambda)}\frac{\mathrm{Ca}}{\mathrm{De}}\frac{1}{L_\infty - 1}[\cos(2\pi\mathrm{De}\ t) - 1]\right)\right)^{-1}\right),
\end{aligned}
\tag{3.18}
$$

where parameters $L_\infty = 1 + \sqrt{15/8}\left(\nu^{-2/3} - 1\right)^{1/2}$ and $A_o = (\nu^{-1/3}l_x^{\max}/2 - 1)/(L_\infty - 1)$; $l_x^{\max}$ is the maximum x-axis length of the vesicle. For the detailed derivation of these results, one can refer to the supporting information.

Following the definitions of the phase boundaries discussed previously, we can derive the two phase boundaries in the limit of $A_0 \ll 1$, i.e. $\ln\left(\frac{1+A_o}{1-A_o}\right) \approx \frac{1}{(L_\infty - 1)}\ln\left(\frac{1+D_o}{1-D_o}\right)$,

$$
\frac{\mathrm{Ca}}{\mathrm{De}} = \frac{\pi(32+23\lambda)}{120}\log\left(\frac{1+D_o}{1-D_o}\right) \quad \text{for pulsating/reorienting phases,} \tag{3.19}
$$

$$
\frac{\mathrm{Ca}}{\mathrm{De}} = \frac{\pi(32+23\lambda)}{60}\log\left(\frac{1+D_o}{1-D_o}\right) \quad \text{for reorienting/symmetrical phases} \tag{3.20}
$$

In the above equations, D_0 is the maximum deformation parameter during the LAOE cycle. Note that the value of D_o is determined by our numerical runs at the highest Ca and De numbers. Based on the quasispherical vesicle theory, the deformation phase boundaries depend on the viscosity ratio, where the factor $(23\lambda + 32)^{-1}$ is related to the relaxation time of the quasi-spherical vesicle [22]. Fig. 3.8a shows the phase boundaries are accurately calculated by using Eq. (3.19) and Eq. (3.20) when the reduced volume is $\nu = 0.8$. Increasing ν from 0.80 to 0.90 shifts the phase boundaries downwards, but maintains a similar linear relation (Fig. 3.8b). We also simulated viscosity ratio $\lambda = 10$ and found that higher viscosity ratios shift the boundaries to higher capillary numbers. We include the dynamics evolution of l_x and l_y (simulations vs. analytical solutions) and $\lambda = 10$ results in the supplementary materials for brevity.

(a) Symmetrical regime

(b) Reorienting regime

(c) Pulsating regime
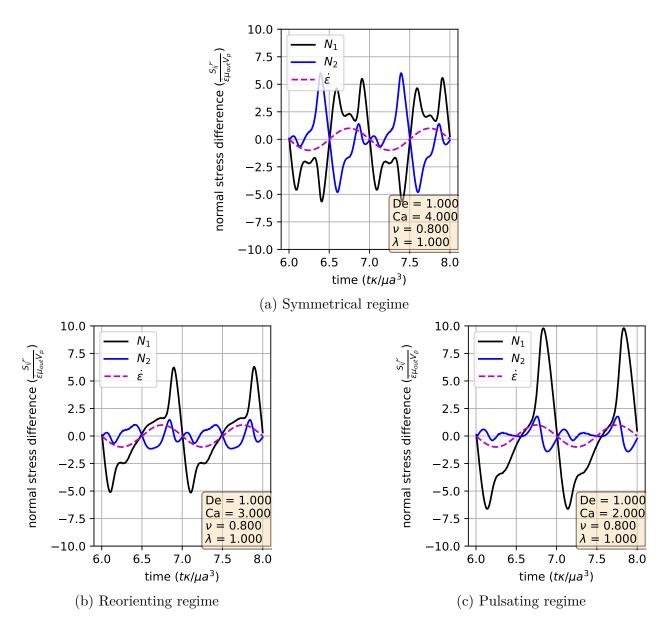
Figure 3.9. Normal stress differences versus time for simulations in the pulsating, reorienting, and symmetrical regimes. Data over two strain rate cycles is plotted. The $\dot{\epsilon}$/Ca dotted line is the strain rate of the external flow; it is used to show the directionality of the flow. Parameters used are included in the figure legends.

3.4.5 Stress response and dilute suspension rheology

For dilute vesicle suspensions where the macroscopic length scale is large in comparison to the size of the vesicles, the extra stress (the bulk stress contribution from the particles) is the product of the number density of particles and the particle stresslet: $\sigma_{ij}^P = n\, \tilde{S}_{ij}^P$. Using the boundary integral formulation, we calculate the particle stresslet [43]:

$$\tilde{S}_{ij}^P = \int_D \frac{1}{2}([[f_i]]x_j + [[f_j]]x_i)\, dS - \int_D (1-\lambda)\mu_{\text{out}}(v_i n_j + v_j n_j)\, dS \tag{3.21}$$

where $[[\boldsymbol{f}]]$ is the surface traction, λ is the viscosity ratio, μ_{out} is the outer viscosity, $\boldsymbol{v}$ is the velocity, and $\boldsymbol{n}$ is the normal vector. We define the dimensionless particle coefficient of stresslet as:

$$S_{ij} = \frac{\tilde{S}_{ij}^P}{\dot{\epsilon}\mu_{\text{out}} V_p} \tag{3.22}$$

where V_p is the vesicle volume and $\dot{\epsilon}$ is the strain rate. Similarly the normal stress differences are defined as:

$$N_1 = S_{xx} - S_{yy} \tag{3.23}$$

$$N_2 = S_{yy} - S_{zz} \tag{3.24}$$

Comparing the normal stress differences to the strain rate, we can derive the rheological characteristics of a dilute vesicle suspension, such as the effective viscosity and bulk normal stresses [103]. For extensional flow rheology, a key quantity of interest is the extensional viscosity of a solution. Extensional viscosity is often characterized using a quantity known as a Trouton ratio (ratio of extensional to shear viscosity), which for a planar extensional flow is a multiple of N_1. For a planar flow, the extensional viscosity is

$$\eta_E = \frac{\sigma_{11} - \sigma_{22}}{\dot{\epsilon}}. \tag{3.25}$$

The planar Trouton ratio is

$$\frac{\eta_E}{\eta} = 4 + \phi * N_1, \tag{3.26}$$

where ϕ is the volume fraction of vesicles in the suspensions, and N_1 is the first normal stress difference. Our simulations have focused on rather large deformations of the vesicle shape, therefore the stress response analysis will reflect the non-linear viscoelasticity.

We examine the stress response for a vesicle that starts off oriented along the x-axis. To link the single vesicle stress response to the expected bulk response for a suspension of randomly oriented vesicles, one needs to average over all possible orientations. Therefore the following results would instead be indicative of a suspension of vesicles all initially oriented along the x-axis. However in the symmetrical regime, all of the starting orientations we tested lead to the same dynamics for the limit cycle behavior. It is possible that the bulk stress response in the symmetrical regime at the limit cycle does not depend on starting orientation. In the pulsating and reorienting regimes on the other hand, the stable orientations depend on several parameters that we have not examined in detail in this study; as reported in Section 3.4.2.

Using the definitions of the particle stresslet and normal stress differences, we determine the vesicle stress as a function of time in extensional flow. In Fig. 3.9, we show the stress response over two cycles for three sets of parameters; one from each of the three dynamical regimes discussed before. A linearly viscoelastic material will show purely sinusoidal normal stress differences for this type of plot, as there is a simple linear relation between the strain rate and the stress. On the other hand, for non-linear viscoelasticity, the normal stress differences will display more complex behaviors.

Fig. 3.9 shows that vesicle dynamics in the three regimes (symmetrical, reorienting, and pulsating) have non-linear characteristics. To analyze these stress responses, we re-plot the data from Fig. 3.9 into a Lissajous-type form with the instantaneous strain rate (Ca_x) on the x-axis and the stress response on the y-axis (Fig. 3.10). For this type of plot, a purely viscous material would display a straight line, whereas a purely elastic material would produce an elliptical curve. For example, the first and second normal stress difference for Newtonian

76

flow around a rigid sphere corresponds to the lines: $N_1 = 10 \cdot \mathrm{Ca}_x/\mathrm{Ca}$ and $N_2 = -5 \cdot \mathrm{Ca}_x/\mathrm{Ca}$. Here, we focus on N_1 because it is related to the extensional viscosity of the solution (Trouton ratio). We also discuss the N_2 stress differences for completeness.

In the symmetrical regime (Fig. 3.10a), we observe that N_1 is symmetric across the origin and that the lines for increasing and decreasing strain rate are nearly the same for $-2 < \mathrm{Ca}_x < 2$. On the other hand, N_2 differs significantly depending on the directionality of the flow. The N_1 curve is mostly linear in the region $-2 < \mathrm{Ca}_x < 2$ and is approximately equal to zero when the strain rate is zero, suggesting that the vesicle contributes a purely viscous response in that region. We further examine this region in more detail by comparing the vesicle deformation to the stress response. From the simulation video and the Lissajous-type deformation parameter curve (Fig. 3.3), we know that the vesicle retains a prolate spheroid like shape and only changes marginally for the $-2 < \mathrm{Ca}_x < 2$ region. The relatively small amount of deformation that occurs in the $-2 < \mathrm{Ca}_x < 2$ region suggests that the vesicle acts like a rigid particle there, explaining the close to linear stress response for N_1 in the region. In the other strain rate regions, the stress differences shift rapidly in accordance to the vesicle's large deformations and reorientation.

In the reorienting and pulsating regimes (Figs. 3.10b and 3.10c), the N_1 curves are no longer symmetric across the origin, and the stress responses for increasing and decreasing strain rate are distinct. The maximum N_1 response is larger in magnitude than the minimum for both regimes; this is likely due to the unequal amounts of deformation between the two strain rate period halves (Fig. 3.3). For this analysis, qualitative differences between the shape of the reorienting and pulsating regime curves correspond to the extent of asymmetry in the N_1 response. Moreover, we observe vesicles in the pulsating regime can have a non-zero normal stress difference when the time-dependent strain rate is zero, as seen in Fig. 3.10c.

For a more quantitative analysis, we decomposed the stress responses into a Fourier series. A similar decomposition was performed by [104] to analytically examine the stress over vesicles over all orientations in small amplitude oscillatory shear with a background constant shear rate under the quasi-spherical assumption. This decomposition is commonly applied to large amplitude oscillatory shear (LAOS) experiments and is known as Fourier transform (FT) rheology. FT rheology is commonly performed using oscillatory shear flows

(a) Symmetrical regime

(b) Reorienting regime

(c) Pulsating regime
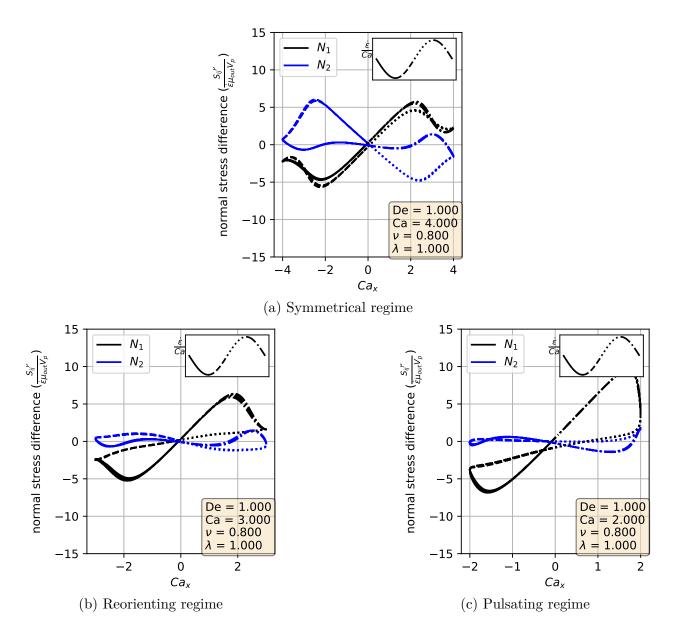
Figure 3.10. Lissajous-type normal stress difference versus strain rate (Ca_x) curves for simulations in the pulsating, reorienting, and symmetrical regimes. The strain rate cycle is separated into four periods demarcated by the line formatting. Parameters used are included in the figure legends.

on polymeric liquids to probe the shear stress response in the non-linear regime [105], [106]. The computation is straightforward and relies on taking the Fourier transform of the N_1 or N_2 stress difference:

$$f(k) = \int_{-\infty}^{\infty} N_{1,2}(t)e^{-2\pi itk} \, dt, \tag{3.27}$$

In this way, the periodic stress signal is transformed into frequency space. Because the external flow field is sinusoidal, the strain rate ($\dot{\epsilon}$) and strain (ϵ) are proportional to sine and cosine functions. Therefore, the Fourier transformed data provide a description of how the stress depends on different orders of the strain and strain rate. If the stress response was purely linear order, the Fourier transformation would show a single peak at the first mode. A non-linear stress response would have additional peaks at higher modes.

The Fourier decompositions for both N_1 and N_2 are shown in Fig. 3.11, where it is clear that all three regimes show higher order behavior. For all regimes, we observe the expected behavior of the linear order mode being the highest amplitude with the higher order modes decreasing monotonically for N_1. On the other hand, the highest amplitude mode for N_2 is not the linear order mode, with the highest generally being the second or third mode. Comparing the N_1 decompositions between the dynamical regimes, we observe that the symmetrical regime does not have even order modes, whereas the reorienting and pulsating regimes have even higher order modes. This change in FT rheology is consistent with the phase boundary defined in Section 3.4.1, and this transition can be used instead of the deformation parameter analysis to demarcate the phase boundary.

In large amplitude oscillatory shear (LAOS), the typical macroscopic stress response shows that the stress is an odd function of the direction of shearing[105]. Such a restriction is not necessarily expected in an extensional flow, but would be related to whether the microstructure of the fluid stretches symmetrically during these flows. In the symmetrical regime, both the vesicle stress response and deformation are time symmetric, leading to only odd order Fourier modes. The time symmetry does not hold for the reorienting or pulsating regimes, allowing for even order modes. Based on the currently available results, we do not expect droplets to have even order Fourier modes in LAOE, regardless of flow rate or flow frequency [102]. Broadly speaking, our results show that membrane-bound vesicles are an

(a) Symmetrical regime

(b) Reorienting regime

(c) Pulsating regime
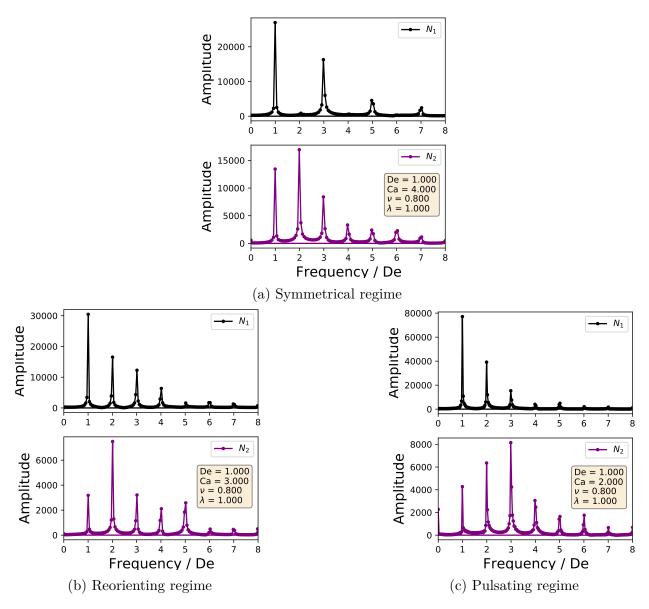
Figure 3.11. Fourier decompositions of the stress responses for indicative parameter sets in each of the dynamical regimes.

interesting example of how anisotropic microstructural deformations can lead to complex rheology.
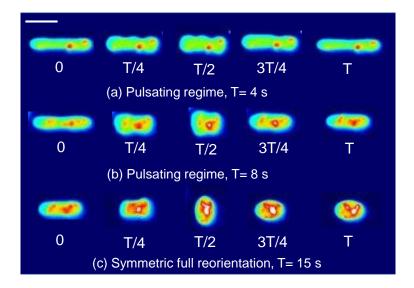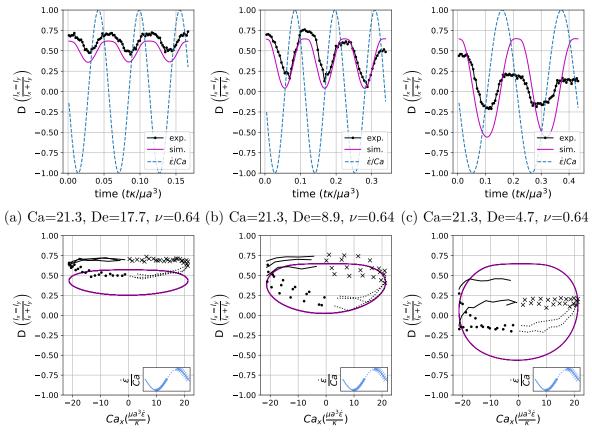
Figure 3.12. Dynamics of a tubular vesicle with reduced volume $\nu = 0.64\pm0.02$ in LAOE. (a) Snapshots showing pulsating dynamics of a vesicle over one sinusoidal strain rate input cycle with time period $T = 4$ s at $Ca = 21.3$ and $De = 17.7$. (b) Snapshots showing pulsating dynamics with wrinkles of a vesicle over one sinusoidal strain rate input cycle with time period $T = 8$ s at $Ca = 21.3$ and $De = 8.9$. (c) Snapshots showing change in 2D shape of a vesicle over one flow cycle with time period $T = 15$ s at $Ca = 21.3$ and $De = 4.7$. Scale bar is 20 μm. False coloring is applied to the grayscale images for resolution enhancement.

(a) Ca=21.3, De=17.7, ν=0.64 (b) Ca=21.3, De=8.9, ν=0.64 (c) Ca=21.3, De=4.7, ν=0.64

(d) Ca=21.3, De=17.7, ν=0.64 (e) Ca=21.3, De=8.9, ν=0.64 (f) Ca=21.3, De=4.7, ν=0.64

Figure 3.13. Experimental and simulation single vesicle Lissajous curves and deformation plots for $\nu = 0.64$.

3.4.6 Transient dynamics of tubular vesicles in large amplitude oscillatory extension

We also investigated the transient dynamics of tubular vesicles in large amplitude oscillatory extension (Fig. 3.12). In general, we find that tubular vesicles undergo wrinkling/buckling instabilities during the compression phase of the flow cycle similar to quasi-spherical vesicles. However, we occasionally observe buckling instabilities that induce unexpected shape changes. In these situations, the vesicle's initial, tubular shape is not recovered at the end of the flow cycle.

Fig. 3.12a shows experimental snapshots of a tubular vesicle with reduced volume $\nu = 0.64 \pm 0.02$ exposed to a sinusoidal strain rate at Ca $= 21.3$ and De $= 17.7$. In this situation, the vesicle exhibits pulsating motion along the x-axis with buckles during the compressional

part of the flow cycle. The vesicle's starting, tubular shape is recovered at the end of the LAOE cycle. To further demonstrate this behavior, we construct single vesicle Lissajous curves (Fig. 3.13(d)) defined as plot of deformation parameter as a function of Ca, and deformation parameter as a function of time (Fig. 3.13(a)). These plots show the vesicle reaches the same value of deformation parameter $D \approx 0.7$ at the end of each of the three repeated flow cycles, implying that the vesicle conformation is fully recovered after deformation. There is decent agreement in the qualitative dynamics between the simulations and experiments in this region, but the simulated deformation parameters appear to be lower than the ones measures experimentally.

When the same vesicle is exposed to a flow cycle at a lower frequency (De = 8.9), the membrane has more time to deform in response to the flow. Here, the vesicle undergoes pulsating motion with wrinkles (Fig. 3.12b) and we observe appreciable deformation along y axis in both the simulations and experiments, as shown in Fig. 3.13b,e. Surprisingly, the experimental results show the vesicle deformation parameter reducing with each subsequent LAOE cycle. The deformation at the end of first cycle is $D \approx 0.7$ and it decreases to $D \approx 0.6$ at the end of second cycle, and further to $D \approx 0.5$ at the end of third cycle. Experimentally, it seems that the vesicle conformation changes over each LAOE cycle while our simulations predict no change over the strain rate cycles. By the end of third repeated cycle, we experimentally observe that the 2D shape of vesicle appears to be more spheroidal than tubular. Interestingly, the vesicle did not recover its original tubular shape even when relaxed for ≈ 2 min. It is noteworthy that we did not observe any reduction in deformation parameter at the higher flow frequency discussed previously (De = 17.7). These observations suggest that for a given Ca, there appears to be a critical De below which the change occurs.

Finally, the same vesicle is exposed to LAOE flow cycle with an even lower frequency (De = 4.7). We observe that the vesicle undergoes full reorientation from the x axis to y axis, undergoes a wrinkling instability during compression and the initial spheroidal shape changes to a more spherical shape at the end of the first periodic cycle (Fig. 3.12c). The deformation behavior seen experimentally during the second repeated cycle is symmetric and follows similar dynamics as those observed for quasi-spherical vesicles. This behavior is more apparent in Fig. 3.13c,f which shows a slight reduction in deformation at the end

83

of first cycle. We observe a large difference in deformation between the simulations and experiments at these parameters. Where the simulations predict the vesicle stretching to $D \approx 0.63$, the experiments only reach $D \approx 0.25$. Additionally, the simulations show that the vesicle does not deform symmetrically at these parameters, reaching $D \approx -0.5$ and $D \approx 0.6$. The experiments were performed sequentially from the higher to lower De on the same vesicle in the experiments, and it seems that the gradual change in vesicle deformation carried over from the previous experiments.

In summary, the experimental data in Fig. 3.12 and Fig. 3.13 shows that the maximum deformation of tubular vesicles may decrease in repeated LAOE cycles and the initial tubular shape may not be recovered. In contrast, the quasi-spherical vesicles always recover a prolate shape following repeated LAOE deformation cycles. We conjecture that the observation of shape transition from prolate tubular to oblate spheroid during LAOE deformation in Fig. 3.12b,c can be explained in the context of the area-difference elasticity model [19]. Briefly, the negative membrane tension on the vesicle membrane during the compressional phase of LAOE flow leads to a decrease in area per lipid which reduces the preferred monolayer area difference [107], [108]. The decrease in monolayer area difference triggers the shape transition from a prolate tubular shape to an oblate spheroid in accordance with the ADE model [19], [109]. This hypothesis is consistent with prior observations where the prolate to oblate transition was triggered by chemical modification of the ambient environment of vesicles [110]. Resolving what exactly is occurring during compressional flow requires additional experiments, likely with 3D confocal microscopy to obtain the full three dimensional vesicle shape.

Additional experimental data on dynamics of highly deflated vesicles ($\nu = 0.35$) is included in the Supplementary Information (Fig. S6 and Fig. S7).

In steady extensional flow with De $= 0$, the critical capillary number required to trigger dumbbell shape transition is a function of reduced volume and the comprehensive phase diagram in Ca $- \nu$ space has been reported in an earlier work [33]. The dumbbell-like shape has also been observed in simulations of a reduced volume $\nu = 0.60$ vesicle in a steady shear flow [111]. Fig. 3.14 qualitatively demonstrates how oscillatory extensional flow alters these shape instabilities. At De $= 1.2$, we observe that the critical capillary number Ca required to
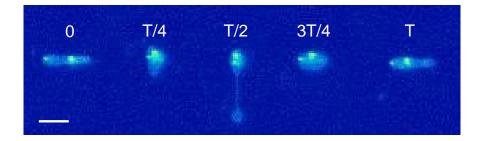
Figure 3.14. Asymmetric dumbbell formation in a vesicle with reduced volume $\nu = 0.69$ exposed to LAOE flow at Ca = 52.5 and De = 1.2. Scale bar is 10 μm.

induce asymmetric dumbbell is much higher compared to steady extensional flow at De = 0. For instance, the critical Ca required to generate asymmetric dumbbell in steady extension for $\nu = 0.69$ is ≈ 5.3 [33]. However, in LAOE flow at De = 1.2, the transition to dumbbell shape occurs at Ca = 52.5 which is approximately ten times higher than the critical Ca for steady flow. This observation can be rationalized by considering the competition between flow cycle time T and inverse of the predicted growth rate of asymmetric instability from linear stability analysis [32]. Briefly, the presence of flow oscillations (De > 0) prevents any instability formation which requires a time scale larger than cycle time T. Thus, a large Ca is needed to reduce the time scale of instability sufficiently to observe the dumbbell formation within the flow cycle time T. While it is possible to explore the phase diagram describing conformation change to asymmetric/symmetric dumbbell on Ca $-$ De space for the entire range of reduced volumes using the Stokes trap, the parameter space is vast and it remains a ripe area for future numerical simulations.

3.5 Conclusions

In this work, we examined the dynamics of vesicles in large amplitude oscillatory extensional (LAOE) flow using both experiments and numerical simulations. The experiments were carried out using the Stokes trap experimental technique while the simulations were done with the boundary element method. For quasi-spherical vesicles, the simulations are found to capture the transient wrinkling dynamics as well as the overall vesicle shapes from

experiments. We have identified three dynamical regimes based on their deformation characteristics and named them the symmetrical, reorienting, and pulsating regimes. Based on these results, we generated a phase diagram in capillary number and Deborah number space for the dynamical regimes; our data suggest that the phase boundaries are linear. The unique deformation observed in the pulsating and reorienting regimes also has interesting effects on the stress response in that the time symmetry of the stress does not hold. Additional analysis of the stress response and confirmation by experimental studies is required for a better idea of the dynamics. Finally, we presented results on highly deflated tubular vesicles which shows that lower reduced volume vesicles tend to undergo a shape change following repeated LAOE deformation. From a broad perspective, we have shown through experiments and simulations that the vesicle system shows interesting dynamics in extensional oscillatory flows. We have also shown how microstructural changes from extensional and compression of a cell-like suspension can affect the overall rheology. Similar dynamics might be observed in other cell-like systems such as red blood cells or single-celled organisms, prompting additional study into time dependent flows for these systems.

3.6   Acknowledgements

4. SURFACE DISCRETIZATION CONSIDERATIONS FOR THE BOUNDARY ELEMENT METHOD APPLIED TO THREE DIMENSIONAL ELLIPSOIDAL PARTICLES IN STOKES FLOW

4.1 Summary

The boundary-element method has often been used for simulating particle motion in Stokes flow, yet there is a scarcity of quantitative studies examining local errors induced by meshing highly elongated particles. In this paper, we study the eigenvalues and eigenfunctions of the double-layer operator for an ellipsoid in an external linear or quadratic flow. We examine the local and global errors induced by changing the interpolation order of the geometry (flat or curved triangular elements) and the interpolation order of the double-layer density (piecewise-constant or piecewise-linear over each element). Our results show that local errors can be quite large even when the global errors are small, prompting us to examine the distribution of local errors for each parameterization. Interestingly, we find that increasing the interpolation orders for the geometry and the double layer density does not always guarantee smaller errors. Depending on the nature of the meshing near high curvature regions, the number of high aspect ratio elements, and the flatness of the particle geometry, a piecewise-constant density can exhibit lower errors than piecewise-linear density, and there can be little benefit from using curved triangular elements. Overall, this study provides practical insights on how to appropriately discretize and parameterize three-dimensional (3D) boundary-element simulations for elongated particles with prolate-like and oblate-like geometries.

4.2 Introduction

There has been recent interest in high fidelity fluid dynamic simulations of systems such as red blood cell flow in capillaries, the sedimentation of many micron-sized particles, or complex microfluidic flows [8], [70], [113]–[116]. In the fluids literature, the boundary-element method (BEM) is often used for these types of problems in the Stokes flow regime. For problems with a low surface area to fluid volume ratio, the boundary-element method benefits from a reduction in dimensionality that potentially improves computational efficiency by reducing the number of unknowns. The BEM is also very efficient for systems with a deformable boundary, as the same deforming boundary is modeled by a surface mesh to solve the interior and exterior flow problems. This is in contrast to other methods, for instance the immersed boundary method that requires both a surface mesh to track the deforming boundary and a volume mesh for evaluating flow variables. Due to the mentioned benefits and other considerations, researchers have used the BEM for several complex particulate flows. Several groups have used boundary integral methods for single particle and large-scale suspensions of rigid particles and developed scalabe algorithms for these systems [117]–[119]. Boundary integral methods are also often used for droplet dynamics [120]–[122]. Additionally, a significant portion of continuum level red blood cell, capsule, and vesicle simulations employ boundary integral methods [8], [9], [123], [124], where researchers have developed large scale and fast implementations [118], [125], [126]

The prevalent use of the BEM for modelling microfluidics motivates studying the numerical errors of these systems. Mathematical analysis has been done on the convergence of the boundary-element method and for evaluating singular and nearly singular integrals [127]–[129]. In each of the applications mentioned, there is a requirement to perform error analysis on the implementation to ensure proper results from simulations. Generally, a significant portion of the error in these simulations comes from the discretization of the domain [43]. Some discretization methods used in the literature include spectral methods [130], [131], isogeometric methods that directly use a mesh from computer-aided development (CAD) [132], [133], and the most common method is parametric interpolation over a discrete mesh [43]. For the parametric interpolation method, commonly a convergence test is performed by in-

creasing the overall number of elements until the error measure drops below a threshold [8], [132]. In most of the mentioned studies a global parameter, such as particle translational velocity, was the parameter of interest. It has been shown that the boundary-element method produces accurate results even at relatively coarse discretizations for these parameters [43]. On the other hand, the discretization properties with regard to local errors have not been tested as widely. The local errors would be important for problems that require accurate resolution of local dynamics, such as resolving the tractions between closely spaced particles.

There are heuristic methods available for controlling discretization errors, such as concentrating mesh points around regions of high boundary curvature or where the solution is expected to show strong variations [43]. Additionally several groups have devised boundary-element implementations for Stokes flow with quadratic or higher order parameterizations of both densities and the geometry [132], [134]. It is still unclear if these higher order methods improve the numerical accuracy or efficiency significantly enough over lower order parameterizations to warrant the additional programming required. Some previous studies have analyzed errors in comparison to analytical solutions, but they have been limited to spherical, 2D, or resistance matrix values [135], [136]. For 3D problems, the study by Chan, Beris, and Advani examined several sources of error in the BEM for closely spaced spheroidal particles [137]. Some of their results for discretization error include the findings that BEM benefits significantly from quadratic geometric interpolation for spherical geometries and that local traction calculations converge with mesh refinement. They also found that the local traction solutions can perform very poorly in comparison to the global metrics, such as the particle rotational velocity.

It may be appropriate for the ultimate paragraph of the introduction to include some personal reflections on the honoree, Prof. R. (Bob) Byron Bird. In 1982, one of the co-authors of this contribution (Sangtae Kim) was recruited by the legendary "BSL transport phenomena trio" of Professors Bird, Stewart and Lightfoot to continue the legacy of transport phenomena at the University of Wisconsin. The initial thought of joining a different campus in warmer climes was trumped by a personal letter from Bob Bird containing the words "we need you!" What followed were many snowy years in Madison filled with great memories and the opportunity to forge a unique identity within transport phenomena in Stokes

flows of particulate systems. Over the years, the emphasis in this line of research evolved towards computational biology and computer-aided drug discovery. But recent forays back to particulate Stokes flow (of ellipsoidal particles) were motivated in part by the continuing correspondence with Professor Bird. In this study, we expanded our understanding of the discretization of 3D Stokes flow problems for the Boundary Element Method (BEM), focusing on high aspect ratio particles where meshing errors are more pronounced. Studying these high aspect ratio particle system is important for understanding the dynamics of needle- or disc-shaped particles. The analytical formulas for the eigenfunctions/eigenvalues of the double layer operator of an ellipsoidal particle in a quadratic flow were recently published in Physics of Fluids for the celebration of Professor Bird's 95th birthday [1]. The formulas provide a new basis for testing boundary-element method discretization effects on accuracy. Comparing against the analytical solution, we will investigate the local and global error properties for the BEM implemented with the collocation method and parametric interpolation over a triangular mesh.

4.3   Methods

4.3.1   Boundary integral formulation and definition of double layer operator

The steady Stokes flow of an incompressible Newtonian fluid can be formulated as

$$\nabla \cdot \boldsymbol{v} = 0 \tag{4.1}$$

$$\nabla p = \mu \nabla^2 \boldsymbol{v}, \tag{4.2}$$

where $\boldsymbol{v}$ is the velocity, p is the pressure, and μ is the viscosity. These equations are linear, therefore we can re-write the velocity field as an integral equation in terms of Green's functions. First, we identify two of the free-space Green's functions for Stokes flow, the Stokeslet and Stresslet:

$$G_{ij}(\boldsymbol{x}, \boldsymbol{x_0}) = \frac{\delta_{ij}}{r} + \frac{\hat{x}_i \hat{x}_j}{r^3} \tag{4.3}$$

$$T_{ijk}(\boldsymbol{x}, \boldsymbol{x_0}) = -6 \frac{\hat{x}_i \hat{x}_j \hat{x}_k}{r^5} \tag{4.4}$$

where $r = |\hat{\boldsymbol{x}}|, \hat{\boldsymbol{x}} = \boldsymbol{x} - \boldsymbol{x}_0$, and $\boldsymbol{x}_0$ is the source point. Repeated indices are assumed to be summed over. $\boldsymbol{G}$ is the solution for Stokes flow from a point force and $\boldsymbol{T}$ is the corresponding solution for the stress tensor. Performing a standard derivation based on the Lorentz's reciprocal theorem [43], we write the integral equation that describes the velocity field inside, outside, and on a prescribed surface D:

$$C(\boldsymbol{x}_0)v_j(\boldsymbol{x}_0) = -\frac{1}{8\pi\mu} \int_D \sigma_{ik}(\boldsymbol{x})n_k(\boldsymbol{x})G_{ij}(\boldsymbol{x},\boldsymbol{x}_0)\,dS(\boldsymbol{x}) + \frac{1}{8\pi} \int_D v_i(\boldsymbol{x})T_{ijk}(\boldsymbol{x},\boldsymbol{x}_0)n_k(\boldsymbol{x})\,dS(\boldsymbol{x}).$$

(4.5)

In the above equation, D is a prescribed surface, n_i is the outward pointing normal vector, and σ_{ij} is the stress tensor for Stokes flow. The coefficient $C(\boldsymbol{x}_0) = 1$ if $\boldsymbol{x}_0$ is inside the surface, $C(\boldsymbol{x}_0) = 0$ if $\boldsymbol{x}_0$ is outside the surface, and $C(\boldsymbol{x}_0) = 1/2$ if $\boldsymbol{x}_0$ lies on the surface (provided the surface is sufficiently smooth). The first integral of Eq. (4.5) is identified as the single layer integral while the second is the double layer integral. In this paper, we will examine the double layer operator:

$$(\mathcal{K}\boldsymbol{q})(\boldsymbol{x}_0) = \frac{1}{4\pi} \int_D q_i(\boldsymbol{x})T_{ijk}(\boldsymbol{x},\boldsymbol{x}_0)n_k(\boldsymbol{x})\,dS(\boldsymbol{x}).$$

(4.6)

Physically, this operator represents the flow created by a distribution of point dipoles on surface D with density $\boldsymbol{q}(\boldsymbol{x})$. For a closed surface like an ellipsoid, the flow field created by $\mathcal{K}\boldsymbol{q}$ decays to zero far away from the surface, has continuous traction across the surface, and experiences a velocity jump across the surface. As one approaches the surface D, the operator satisfies:

$$\lim_{\epsilon \to 0}(\mathcal{K}\boldsymbol{q})(\boldsymbol{x}_0 \pm \epsilon\boldsymbol{n}) = (\mathcal{K}\boldsymbol{q})(\boldsymbol{x}_0) \pm \boldsymbol{q}(\boldsymbol{x}_0); \quad \boldsymbol{x}_0 \in D$$
$$= \frac{1}{4\pi} \int_D^{PV} q_i(\boldsymbol{x})T_{ijk}(\boldsymbol{x},\boldsymbol{x}_0)n_k(\boldsymbol{x})\,dS(\boldsymbol{x}) \pm \boldsymbol{q}(\boldsymbol{x}_0).$$

(4.7)

91

Note that whenever we calculate the double layer operator at position $\boldsymbol{x}_0 \in D$, we compute the principal value of the surface integral (PV). The information above will be useful in describing the eigenspectrum of the operator $\mathcal{K}$ as discussed in the next section.

An accurate numerical representation of the double layer operator is vital in many applications. For example, the boundary integral formulation for rigid particles can be recast in terms of $\mathcal{K}$ only [138], [139], which is advantageous numerically because it forms a Fredholm integral equation of the second kind and hence does not face issues with ill-posedness [46]. This paper will discuss analytical solutions to the eigenvalues/eigenvectors of the double layer operator, and quantify errors that arise when numerically discretizing the double layer operator.

4.3.2 Analytical eigenvalues and eigenfunctions of double layer operator

For a given surface D, the double layer operator $\mathcal{K}$ in Eq. (4.6) has an infinite number of eigenvalues λ and eigenfunctions $\boldsymbol{\psi}(\boldsymbol{x})$. These eigensolutions cannot be evaluated analytically for a general shape. However, analytical solutions are available for ellipsoids undergoing rigid body motion, motion in a rate-of-strain field, and motion in a general quadratic flow field [1]. We will summarize the results in the literature in the next subsections. In general, one analytically determines the eigenvalues and eigenfunctions by solving the flow around a prescribed surface subject to the conditions of (a) zero velocity far from the surface, (b) continuity of traction across the surface, and (c) a prescribed velocity jump across the surface. For each eigenfunction/eigenvalue pair $(\boldsymbol{\psi}, \lambda)$, the velocity jump satisfies:

$$\boldsymbol{v}^{(o)} = \mathcal{K}\boldsymbol{\psi} + \boldsymbol{\psi} = (\lambda + 1)\boldsymbol{\psi} \tag{4.8}$$

$$\boldsymbol{v}^{(i)} = \mathcal{K}\boldsymbol{\psi} - \boldsymbol{\psi} = (\lambda - 1)\boldsymbol{\psi} \tag{4.9}$$

where $\boldsymbol{v}^{(0)}$ is the flow field as the particle surface is approached from the outside, and $\boldsymbol{v}^{(i)}$ is the flow field as the particle surface is approached from the inside. Thus, if one determines the conditions under which the outer and inner velocities are collinear, one can determine

the eigenvalues λ and eigenfunctions $\boldsymbol{\psi}$. The eigenvalues range within the real interval $\lambda \in [-1, 1]$ [46].

Rigid Body Motion

For any surface D, the rigid body motions $\boldsymbol{v}^{RBM} = \{\boldsymbol{V}, \boldsymbol{\Omega} \times \boldsymbol{x}\}$ are eigenfunctions of the double layer operator. The corresponding eigenvalue is $\lambda = -1$:

$$(\mathcal{K}\boldsymbol{v}^{RBM})(\boldsymbol{x}_0) = \frac{1}{4\pi} \int_D^{PV} v_i^{RBM}(\boldsymbol{x}) T_{ijk}(\boldsymbol{x}, \boldsymbol{x}_0) n_k(\boldsymbol{x}) \, dS(\boldsymbol{x}) = -\boldsymbol{v}^{RBM}(\boldsymbol{x}_0), \qquad (4.10)$$

The Torque-Free Ellipsoid in a Constant Rate-of-Strain Field

There are five eigenfunction/eigenvalue pairs for a torque-free ellipsoid in a constant rate-of-strain field $\boldsymbol{v}^\infty = \boldsymbol{E}^\infty \cdot \boldsymbol{x}$. We decompose the field into off-diagonal and diagonal ambient fields. These two problems are solved and analyzed separately, with the simpler off-diagonal case discussed first.

For the off-diagonal rate-of-strain fields, we decompose $\boldsymbol{E}^\infty$ into

$$\boldsymbol{E}^\infty = \boldsymbol{E}^{(12)} + \boldsymbol{E}^{(13)} + \boldsymbol{E}^{(23)},$$

$$\boldsymbol{E}^{(12)} = \begin{pmatrix} 0 & E_{12} & 0 \\ E_{12} & 0 & 0 \\ 0 & 0 & 0 \end{pmatrix}, \boldsymbol{E}^{(13)} = \begin{pmatrix} 0 & 0 & E_{13} \\ 0 & 0 & 0 \\ E_{13} & 0 & 0 \end{pmatrix}, \boldsymbol{E}^{(23)} = \begin{pmatrix} 0 & 0 & 0 \\ 0 & 0 & E_{23} \\ 0 & E_{23} & 0 \end{pmatrix}, \quad (4.11)$$

Each of these components gives rise to an eigenvector/eigenvalue pair. To determine the eigenvectors driven by E_{12}, E_{13}, or E_{23}, we solve for the disturbance velocity field inside and outside a torque-free ellipsoid with continuous traction across the surface. The eigenvector is related to the jump in velocity across the surface as $2\boldsymbol{\psi} = \boldsymbol{v}^{(o)} - \boldsymbol{v}^{(i)}$, and the eigenvalue is determined by noting that $\boldsymbol{v}^{(i)} = \boldsymbol{v}^{(o)}(\lambda - 1)/(\lambda + 1)$. We obtain for the three eigenvector/eigenvalue pairs:

$$\lambda^{(12)} = \gamma_0'(a^2 + b^2) - 1, \quad \psi^{(12)} = \boldsymbol{E}^{(12)} \cdot \boldsymbol{x} - \left(\frac{a^2 - b^2}{a^2 + b^2}\right) E_{12}\boldsymbol{\delta}_3 \times \boldsymbol{x},$$

$$\lambda^{(13)} = \beta_0'(a^2 + c^2) - 1, \quad \psi^{(13)} = \boldsymbol{E}^{(13)} \cdot \boldsymbol{x} - \left(\frac{c^2 - a^2}{a^2 + c^2}\right) E_{13}\boldsymbol{\delta}_2 \times \boldsymbol{x},$$

$$\lambda^{(23)} = \alpha_0'(b^2 + c^2) - 1, \quad \psi^{(23)} = \boldsymbol{E}^{(23)} \cdot \boldsymbol{x} - \left(\frac{b^2 - c^2}{b^2 + c^2}\right) E_{23}\boldsymbol{\delta}_1 \times \boldsymbol{x}. \tag{4.12}$$

In the above equation, a, b, c are the semi-axes of the ellipsoid, while γ_0', α_0', and β_0' are elliptic integrals. The elliptic integral $\gamma_0' = \int_0^\infty dt/((a^2 + t)(b^2 + t)\Delta(t))$, where $\Delta(t) = \sqrt{(a^2 + t)(b^2 + t)(c^2 + t)}$. The other elliptic integrals are obtained by permutation of the semi-axes a, b, c.

All three eigenvalues above are equal to $\lambda = -1/5$ for the degenerate case of the sphere, $a = b = c$. Fig. 4.1(a-c) shows the eigenfunctions associated with the flows $E^{(12)}$, $E^{(23)}$, and $E^{(13)}$ for a prolate ellipsoid ($a = 4$, $b = c = 1$). For an oblate ellipsoid ($a = b = 4$, $c = 1$), the eigenfunctions are shown in Fig. 4.1(f-h).

Next, we consider a diagonal rate-of-strain field

$$\boldsymbol{E}^\infty = \begin{pmatrix} E_{11} & 0 & 0 \\ 0 & E_{22} & 0 \\ 0 & 0 & E_{33} \end{pmatrix}, \ E_{11} + E_{22} + E_{33} = 0. \tag{4.13}$$

To determine the two eigenvectors/eigenvalue pairs associated with this field, we solve the disturbance flow field around a torque-free ellipsoid with continuous traction across its surface for arbitrary E_{11} and E_{22}. If we make the inner and outer velocities at the surface of the ellipsoid collinear, i.e., $\boldsymbol{v}^{(i)} = \kappa\boldsymbol{v}^{(o)} = \boldsymbol{v}^{(o)}(\lambda{-}1)/(\lambda + 1)$, this will yield an eigenvalue problem. There will be two eigenvalues λ, and each will be associated with an admissible pair (E_{11}, E_{22}) up to a scaling constant (which allows one to compute the eigenvector ψ). We state the results below:
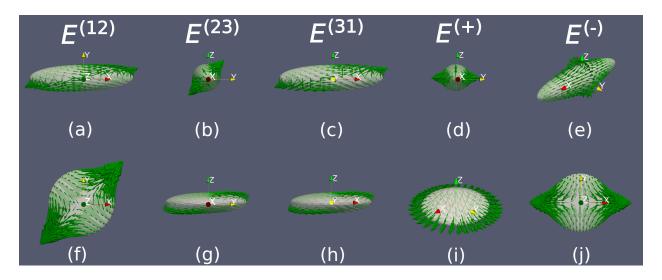
Figure 4.1. Linear ROS eigenfunctions where sub-figures (a) – (e) are for an $a = 4, b = 1, c = 1$ prolate spheroid while sub-figures (f) – (j) are for a $a = 4, b = 4, c = 1$ oblate spheroid. Flows $E^{(12)}$, $E^{(23)}$, and $E^{(31)}$ are planar off-diagonal flows. The first three columns of figures show 2D plots of the off-diagonal flows. Note the orientation difference between (a) and (c), similarly for (g) and (h). (a) and (c) resemble a simple shear flow, the eigenfunctions approach simple shear flow with increasing particle aspect ratio of the spheroids; the same applies for (g) and (h). The $E^{(+)}$ and $E^{(-)}$ flows are planar extension and uniaxial extension for spheroids.

$$\kappa^{\pm} = \left(\frac{\lambda - 1}{\lambda + 1}\right)^{\pm} = 1 - \frac{2}{3d}(\alpha_0'' + \beta_0'' + \gamma_0'') \pm \frac{2}{3d}\left[(\alpha_0'' - \beta_0'')^2 + (\beta_0'' - \gamma_0'')^2 + (\gamma_0'' - \alpha_0'')^2\right]^{1/2},$$

where

$$d = \alpha_0''\beta_0'' + \beta_0''\gamma_0'' + \gamma_0''\alpha_0'', \quad \gamma_0'' = \int_0^{\infty} \frac{t\,dt}{(a^2 + t)(b^2 + t)\Delta(t)}, \tag{4.14}$$

Similar to what was discussed before, the other elliptic integrals, α_0'' and β_0'', are defined by cyclic permutation of the semi-axes. We denote the values of (E_{11}, E_{22}, E_{33}) associated with eigenvalues $\lambda^{\pm}$ as $E^{(+)}$ and $E^{(-)}$, respectively. In Fig. 4.1(d,e), we plot flows associated with $E^{(+)}$ and $E^{(-)}$ for a prolate ellipsoid ($a = 4$, $b = c = 1$). For the oblate ellipsoid ($a = b = 4$, $c = 1$), the two flows associated with $E^{(+)}$ and $E^{(-)}$ are displayed in Fig. 4.1(i,j).

Ellipsoid in Quadratic Flow Field $-$ 3×3 **System**

A force-free, torque-free ellipsoid submerged in a viscous quadratic flow field $\boldsymbol{v}^\infty = \boldsymbol{H} : \boldsymbol{x}\boldsymbol{x}$ is now considered, where the origin of the coordinate system is chosen to be the particle's center of mass. Note that the third order tensor H_{ijk} possesses 15 independent variables, and the disturbance velocity generated by this quadratic field for a rigid ellipsoid is discussed in Kim and Arunachalam [140] as a function of P_j and P_{jkl} – i.e., the strengths of force and quadrupole moments.

Due to particle symmetry, the general ambient quadratic flow field can be divided into four decoupled systems [140]: one 3×3 and three 5×5 systems, where the 5×5 systems have three redundant equations in order to have 15 independent components. In this work, we focus on the eigenvalues and eigenfunctions of the 3×3 system, while one can refer to [1], [119], [141], [142] for the 5×5 systems.

The ambient field of the 3×3 system involves three independent variables

$$v_1^\infty = \mathcal{H}_1 x_2 x_3, \quad v_2^\infty = \mathcal{H}_2 x_1 x_3, \quad v_3^\infty = \mathcal{H}_3 x_1 x_2. \tag{4.15}$$

where

$$\mathcal{H}_1 = H_{123} + H_{132}, \quad \mathcal{H}_2 = H_{213} + H_{231}, \quad \mathcal{H}_3 = H_{312} + H_{321}, \tag{4.16}$$

In Kim and Arunachalam, the disturbance velocity for this field is related to the quadrupole moments $(P_{123} + P_{132})$, $(P_{213} + P_{231})$, and $(P_{312} + P_{321})$. By determining the flow velocity at the particle surface, the relationship between H_{ijk} and P_{ijk} is found to be

$$\mathcal{H}_1 = \mathcal{A}_1 \left(K_{23} + a^2 K_{123} \right) + \mathcal{A}_2 \left(-K_{13} + b^2 K_{123} \right) + \mathcal{A}_3 \left(-K_{12} + c^2 K_{123} \right),$$
$$\mathcal{H}_2 = \mathcal{A}_1 \left(-K_{23} + a^2 K_{123} \right) + \mathcal{A}_2 \left(K_{13} + b^2 K_{123} \right) + \mathcal{A}_3 \left(-K_{12} + c^2 K_{123} \right),$$
$$\mathcal{H}_3 = \mathcal{A}_1 \left(-K_{23} + a^2 K_{123} \right) + \mathcal{A}_2 \left(-K_{13} + b^2 K_{123} \right) + \mathcal{A}_3 \left(K_{12} + c^2 K_{123} \right), \tag{4.17}$$

where

$$\mathcal{A}_1 = \frac{15}{32\pi\mu}\left(P_{123} + P_{132}\right), \quad \mathcal{A}_2 = \frac{15}{32\pi\mu}\left(P_{213} + P_{231}\right), \quad \mathcal{A}_3 = \frac{15}{32\pi\mu}\left(P_{312} + P_{321}\right). \quad (4.18)$$

In the above equations, K_{ij} and K_{ijk} are elliptic integrals defined in reference [1], [141] and are related to the elliptic integrals α, β, and γ from the rate-of-strain problem.

To determine the eigenvector/eigenvalue pairs, one needs an additional relationship between the quadrupole moments $(\mathcal{A}_1, \mathcal{A}_2, \mathcal{A}_3)$ and the velocity moments $(\mathcal{H}_1, \mathcal{H}_2, \mathcal{H}_3)$. To do this, we will set the velocity field inside the surface of the ellipsoid to $\boldsymbol{v}^{(i)} = \kappa\boldsymbol{v}^{(o)}$, where $\kappa = (\lambda{-}1)/(\lambda+1)$ is related to the eigenvalue λ, and $\boldsymbol{v}^{(o)}$ is the disturbance velocity field on the surface. We will then equate the traction inside the surface to the traction outside the surface from the disturbance field, which yields the relationship [1]:

$$\frac{4\mathcal{A}_1}{abc} = (1 - \kappa)\left[(b^2 + c^2)\mathcal{H}_1 + c^2\mathcal{H}_2 + b^2\mathcal{H}_3\right],$$
$$\frac{4\mathcal{A}_2}{abc} = (1 - \kappa)\left[c^2\mathcal{H}_1 + (a^2 + c^2)\mathcal{H}_2 + a^2\mathcal{H}_3\right],$$
$$\frac{4\mathcal{A}_3}{abc} = (1 - \kappa)\left[b^2\mathcal{H}_1 + a^2\mathcal{H}_2 + (a^2 + b^2)\mathcal{H}_3\right], \quad (4.19)$$

Eq. (4.17) and Eq. (4.19) now allow us to determine the eigenvalues λ, which are related to κ by $\kappa = (\lambda - 1)/(\lambda + 1)$. By substituting $\mathcal{A}_i$ in terms of $\mathcal{H}_i$ using Eq. (4.17), an equation of the form $B_{ij}\mathcal{H}_j = 0$ is found. For a nontrivial solution to exist, $\det(B_{ij}) = 0$, and the roots of the resulting cubic equation are solved to determine three eigenvalues λ and the associated eigenfunctions ψ. We denote the velocity moments $(\mathcal{H}_1, \mathcal{H}_2, \mathcal{H}_3)$ associated with the three eigenvalues by $Q^{(1)}, Q^{(2)}$ and $Q^{(3)}$, respectively. Fig. 4.2(a-c) show plots of the eigenfunctions associated with $Q^{(1)}, Q^{(2)}$ and $Q^{(3)}$ for a prolate ellipsoid ($a = 4$, $b = c = 1$), where $Q^{(1)}$ corresponds to the largest eigenvalue and $Q^{(3)}$ to the least eigenvalue. For the oblate particle ($a = b = 4$, $c = 1$), the corresponding eigenfunctions are shown in Fig. 4.2(d-f).
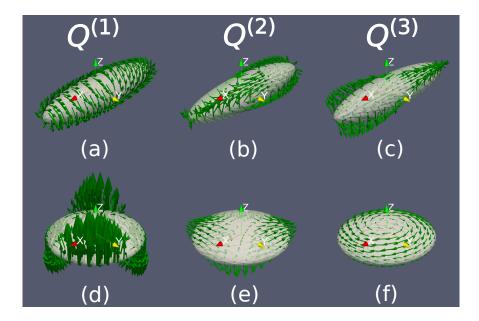
Figure 4.2. Streamlines for quadratic order eigenfunctions where sub-figures (a) – (c) are for $a = 4, b = 1, c = 1$ prolate spheroid while sub-figures (d) – (e) are for $a = 4, b = 4, c = 1$ oblate spheroid. $\boldsymbol{Q}^{(1)}$: Quadratic eigenfunction corresponding to the largest eigenvalue of the 3x3 system. $\boldsymbol{Q}^{(2)}$: Quadratic eigenfunction corresponding to the middle eigenvalue of the 3x3 system. $\boldsymbol{Q}^{(3)}$: Quadratic eigenfunction corresponding to the least eigenvalue of the 3x3 system.

4.3.3 Numerical representation of double layer operator for ellipsoids

In this section, we will discretize the double layer operator in Eq. (4.6) using the boundary-element method (BEM). We will then compare the eigensolutions of this discretized operator to the analytical solutions, to benchmark the numerical accuracy of BEM for highly elongated ellipsoidal particles in different flow types. Details of the numerical representation are given below along with notation for the different parameterizations studied.

Numerical Details

Meshing:

We represent the ellipsoidal particle with an unstructured triangular mesh. The elements are either flat triangles with 3 nodes (linear geometric interpolation) or curved triangles with 6 nodes (quadratic geometric interpolation). Higher order geometric parameterizations (cu-

bic or higher) could lead to further improvements in practice, but are rarely implemented due to coding complexity. We generate the surface mesh by taking a hard-coded icosahedron mesh, subdividing the mesh to a desired number of triangles (via geodesic subdivision), and projecting the vertices onto a unit sphere. The curved (quadratic) meshes are created by adding vertices to the middle of mesh edges after the geodesic subdivision step. It is important that the mid-edge vertices are also projected onto the unit sphere, otherwise the higher order interpolation will not be of much benefit. We then apply a scaling transformation to move the mesh vertices to the desired ellipsoidal surface (Fig. 4.3).

We use this icosahedron subdivision method because it is simple to implement and is commonly used in the literature [35], [143]. However the method has clear pitfalls, such as how the scaling transformation applied will produce highly stretched triangles at higher particle aspect ratios. Additionally, the surface normal vector is not enforced to be continuous across the elements. Other simplistic meshing methods also have clear deficiencies [144], [145], such as having to deal with the singularities at the geometric poles of an ellipsoid when using a structured mesh. This paper will illustrate how a common meshing procedure can lead to unintuitive errors.

Parametric interpolation:

To discretize the double layer operator in Eq. (4.6), one can apply sets of interpolation and weighting functions over the mesh. A commonly applied method in the finite element literature is to use the same functions for both the interpolation over elements and the weighting for residual minimization, known as the Galerkin method [146]. However even though the Galerkin method has better accuracy for the same number of unknowns, the collocation method is more commonly used in the BEM literature [143]. This is mainly due to the fact that the Galerkin method requires evaluating a double surface integral, while the collocation method only requires a single surface integral. We will be using the collocation

method in this study. The interpolation functions generally chosen are piecewise polynomials up to quadratic order [143] such that a density $\boldsymbol{q}$ is approximated over the surface as

$$q_i(\xi, \eta) = \sum_{n=1}^{\text{nodes}} \phi_n(\xi, \eta) \hat{q}_i^{(n)}, \qquad (4.20)$$

where ϕ are the interpolation functions that depend on the parametric position (ξ, η) and $\hat{\boldsymbol{q}}^{(n)}$ is the value of $\boldsymbol{q}$ at node n. We consider piecewise-constant and piecewise-linear interpolation of the double layer densities. For the piecewise-constant density we use the element centroids as nodes, while the mesh vertices are used as nodes for the piecewise-linear density.

Quadrature and singularity subtraction:

To evaluate the surface integrals over the mesh elements we use six-point Gauss-Legendre quadrature, which is sufficient for accurately evaluating over quadratic elements [147]. For integrals over singular elements, we use the singularity subtraction method detailed in [46]. Specifically, we use the $\lambda = -1$ eigenvalue solution that is valid over any closed surface to remove the singularity

$$\frac{1}{4\pi} \int_D^{PV} q_i(\boldsymbol{x}) T_{ijk}(\boldsymbol{x}, \boldsymbol{x}_0) n_k(\boldsymbol{x}) \, dS(\boldsymbol{x}) =$$
$$\frac{1}{4\pi} \int_D^{PV} (q_i(\boldsymbol{x}) - q_i(\boldsymbol{x}_0)) T_{ijk}(\boldsymbol{x}, \boldsymbol{x}_0) n_k(\boldsymbol{x}) \, dS(\boldsymbol{x}) - q_i(\boldsymbol{x}_0) \delta_{ij}. \qquad (4.21)$$

where PV represents the principal value of the integral. Our current implementation does not make any distinction for nearly singular integrals because the ellipsoidal meshes and parameterizations tested do not have nearly singular node pairs.

Notation

The boundary-element collocation scheme creates a discretized version of the double layer operator $\mathcal{K}$ and the double layer density $\boldsymbol{q}(\boldsymbol{x})$ on the ellipsoid surface. From here on out, we will denote by symbols with a hat over them as the discretized versions over N nodes, while symbols without the hat represent the continuous counterparts. For example, the discretized
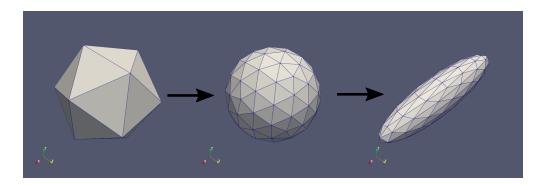
Figure 4.3. Icosahedron subdivision meshing procedure. From left to right: initial icosahedron mesh, subdivided mesh projected onto unit sphere, and scaling transformation applied to that mesh.

double layer density $\hat{\boldsymbol{q}}$ is a $3N \times 1$ vector of all nodal values on the ellipsoidal surface, i.e., $\hat{\boldsymbol{q}} = [\hat{\boldsymbol{q}}^{(1)}; \hat{\boldsymbol{q}}^{(2)}; \ldots; \hat{\boldsymbol{q}}^{(N)}]$ for all N nodes. The discretized version of $\mathcal{K}$ is $\hat{\boldsymbol{K}}$, which is an $3N \times 3N$ matrix such that $\hat{\boldsymbol{K}} \cdot \hat{\boldsymbol{q}}$ yields the approximate value of $\mathcal{K}\boldsymbol{q}$ on all N nodes of the surface. From a bookkeeping standpoint, the matrix $\hat{\boldsymbol{K}}$ can be decomposed into several 3×3 sub-blocks $\hat{\boldsymbol{K}}^{(nm)}$ $(n, m = 1, 2, \ldots N)$, where the (n, m) sub-block represents the influence of node m on the velocity at node n. We will test how well the eigensolutions of the discretized operator $\hat{\boldsymbol{K}}$ match those of the analytical solutions.

The notation we employ for the discretization types used in this study is shown in Table 4.1. For example, a discretization scheme that uses linear interpolation functions for the double-layer density and quadratic interpolation functions for the geometry would be denoted ld-qe. Additionally we list the ellipsoid semi-axis lengths as a string of three numbers with dashes, such that an oblate spheroid with ($a = 4$, $b = 4$, $c = 1$) would be 4-4-1.

Table 4.1. Shorthand for the discretization types.

cd	piecewise-constant density
ld	piecewise-linear density
le	linear elements (flat triangles)
qe	quadratic elements (curved triangles)

4.3.4 Determining error of discretized double layer operator

Global error – rigid body motion

One way we can test the accuracy of a discretization is to compute the rigid body motions of an ellipsoid in a specified external flow field and compare them with analytical solutions. The errors in this problem are global because rigid body motion is determined from averaging a computed velocity over an entire surface rather than knowing the solution at any given point. It is known that the boundary-element method produces satisfactory global error values with a relatively small number of elements [43]. To simulate the mobility problem, we use the completed double layer (CDL) method described in [43], [46] that removes the six $\lambda = -1$ eigenvalues corresponding to rigid body motion from the double layer operator. We are operating over a force- and torque-free particle, therefore the completed double layer operator is:

$$\mathcal{K}^c = \frac{1}{4\pi} \int_D^{PV} q_j(\boldsymbol{x}) T_{jik}(\boldsymbol{x}, \boldsymbol{x_0}) n_k(\boldsymbol{x})\, dS(\boldsymbol{x}) + V_i + \epsilon_{ijk}\Omega_j X_k. \tag{4.22}$$

where $\boldsymbol{V}$ and $\boldsymbol{\Omega}$ are the translational and rotational velocities respectively, formulated as functions of the double layer density ($\boldsymbol{q}$) as:

$$\boldsymbol{V} = -\frac{4\pi}{S_D} \int_D \boldsymbol{q}\, dS \tag{4.23}$$

$$\boldsymbol{\Omega} = -4\pi \sum_{m=1}^{3} \frac{1}{A_m} \boldsymbol{\omega}^{(m)} \left(\boldsymbol{\omega}^{(m)} \cdot \int_D \boldsymbol{X} \times \boldsymbol{q}\, dS \right). \tag{4.24}$$

In the above formulas, S_D is the surface area and $\boldsymbol{X}$ are the particle-centered coordinates. The terms A_m and $\boldsymbol{\omega}^{(m)}$ are the eigenvalues and normalized eigenvectors of the surface-based moment of inertia tensor $\boldsymbol{I}_{mom} = \int_D (X_k X_k \delta_{ij} - X_i X_j) dS$.

The completed double layer operator is discretized to a $3N \times 3N$ matrix $\hat{\boldsymbol{K}}^c$ over the N nodes on the ellipsoid, and then used in the following expression to solve for the double-layer density $\hat{\boldsymbol{q}}$ at each node:

$$(\hat{\boldsymbol{I}} + \hat{\boldsymbol{K}}^c) \cdot \hat{\boldsymbol{q}} = \hat{\boldsymbol{u}}^\infty \tag{4.25}$$

In the above formula, $\hat{\boldsymbol{I}}$ is the $3N \times 3N$ identity tensor and $\hat{\boldsymbol{u}}^\infty$ is the external flow vector evaluated at the nodes on the ellipsoid. We only test simple shear flow with the CDL method in this study. Once we determine the double layer density ($\hat{\boldsymbol{q}}$) at each node, we integrate over the surface using Eq. (4.23) and Eq. (4.24) to produce the translational and rotational velocities. The l_2 norms are then compared to those of the analytical solutions as follows.

$$E_V = \frac{||\boldsymbol{V}^{anal} - \boldsymbol{V}^{num}||}{||\boldsymbol{V}^{anal}||} \quad E_\Omega = \frac{||\boldsymbol{\Omega}^{anal} - \boldsymbol{\Omega}^{num}||}{||\boldsymbol{\Omega}^{anal}||} \tag{4.26}$$

where E_V and E_Ω are the translational or rotational velocity errors, with $\{\boldsymbol{V}^{anal}, \boldsymbol{\Omega}^{anal}\}$ being the analytical particle velocities, and $\{\boldsymbol{V}^{num}, \boldsymbol{\Omega}^{num}\}$ the numerical approximations.

Local nodal error − double layer operator

We will characterize the local errors in the discretized double layer operator $\hat{\boldsymbol{K}}$ by determining how closely it obeys known eigenvector/eigenvalue relationships at each nodal point in various flows. In this procedure, we take a known eigenvector $\boldsymbol{\psi}$ for the ellipsoidal particle and normalize it by its inner product based norm

$$\tilde{\boldsymbol{\psi}} = \frac{\boldsymbol{\psi}}{<\boldsymbol{\psi}, \boldsymbol{\psi}>^{1/2}} \quad <\boldsymbol{\psi}, \boldsymbol{\psi}> = \frac{1}{S_D} \int_D \boldsymbol{\psi} \cdot \boldsymbol{\psi} \, dS, \tag{4.27}$$

Once we complete this procedure, we will compute the normalized eigenvector at the N node positions on the ellipsoid surface to create a $3N \times 1$ vector of values $\hat{\boldsymbol{\psi}}$. We then matrix multiply the discretized double-layer matrix ($\hat{\boldsymbol{K}}$) with ($\hat{\boldsymbol{\psi}}$) and check the resultant output against the expected solution ($\lambda\hat{\boldsymbol{\psi}}$) at the nodal values $\hat{\boldsymbol{x}}$. This yields a $3N \times 1$ vector of errors at each nodal point.

$$\hat{\boldsymbol{\epsilon}} = \hat{\boldsymbol{K}} \cdot \hat{\boldsymbol{\psi}} - \lambda\hat{\boldsymbol{\psi}} \tag{4.28}$$

Because we are using a known eigenfunction of the double-layer operator, a perfect discretization of the operator should yield zero for the above expression.

We define the local error at a particular node to be

$$\epsilon^{(i)} = ||\hat{\boldsymbol{\epsilon}}^{(i)}||, \qquad (4.29)$$

where $\cdot^{(i)}$ means the i'th node. Later in this paper, we will plot the distribution of these errors over the ellipsoidal surface for various types of flows. We will also use the arithmetic mean and maximum of the local errors to get an idea of the distribution of local errors:

$$\epsilon_{\text{mean}} = \frac{\sum_i \epsilon^{(i)}}{N} \qquad (4.30)$$

$$\epsilon_{\text{max}} = \max(\epsilon^{(i)}) \qquad (4.31)$$

4.4 Results

4.4.1 Numerical error sources

There are several issues that limit the numerical accuracy of the boundary-element method (BEM) to consider in this study. Firstly, there are the effects of discretizing the system geometry that directly alters the geometric properties of the surface (e.g., surface area, curvature, etc.). The parameterization of the double layer density also needs to be considered (e.g., piecewise constant, piecewise linear, etc.). Other sources of error include the approximation error from evaluating the integrals, singular integral handling, and linear system solution procedure. Our implementation uses six point Gaussian quadrature to evaluate the integrals and handles the singular integrals using the singularity subtraction method, therefore errors from those sources should only make minor contributions. When testing the local errors, the analytical eigenfunctions are directly tested against the discretized double layer matrix, bypassing any numerical solution of the linear system. Therefore, this paper focuses on the errors from discretizing the geometry and double layer density, and finding how the parameterization and the meshing procedures can affect accuracy.

4.4.2 Mobility solution errors

Global rotational velocity error

We start our analysis by considering the error in computing the rotational velocity of a 4-1-1 prolate spheroid in a simple shear flow. The errors are plotted against the number of nodes for a given parameterization in Fig. 4.4 and the same errors are tabulated in Table 4.2. We plotted the errors against the number of nodes N because this is proportional to the number of unknowns for a given parameterization. We note that for the same mesh, the problem size is different for different parameterizations of the double layer density. For the piecewise-linear double layer density, the number of nodes is equal to the number of vertices on the mesh ($N = N_{ele}/2 + 2$). For the the piecewise-constant double layer density, the number of nodes is equal to the number of elements ($N = N_{ele}$). We note that one could examine errors against the number of elements, which would compare the parameterizations for a given mesh rather than for similar problem sizes.

From Fig. 4.4, we observe that the error in the rotational velocity converges at power-law rate with the number of nodes N, with an exponent -2 for the piecewise-linear density and -1 for the piecewise-constant density. Such power-law behavior is expected for these methods (called h-type in the literature) as the element spacing is reduced [148]. For the piecewise-constant density (cd-le and cd-qe), improving the geometry interpolation function from linear to quadratic improves the accuracy so that the quadratic mesh produces less than 1% error with 320 elements while the linear mesh is still at 1.21%. This effect is also seen for the piecewise-linear density (ld-le and ld-qe), leading to 1.211% error for ld-qe over the 80 element mesh. From a prior study by Chan, et al. [137], we know that increasing the geometry interpolation order can greatly improve the calculation accuracy of global error metrics.

On comparing the two density parameterization methods, the higher convergence rate for the piecewise-linear density is expected, as the higher order interpolation functions used should lead to more accurate results. Interestingly, we find that for a small number of elements the linear density, linear element (ld-le) parameterization performs worse than either the constant density, linear element (cd-le) or constant density, quadratic element (cd-

qe) parameterizations. For example, the ld-le parameterization produces a large rotational velocity error of $\approx 35\%$ with the 80 element mesh while the other parameterizations all have less than 5% error for the same mesh. Comparing the ld-le parameterization with 92 nodes to the similar 80 node cd-le parameterization, we see that the ld-le parameterization still has a higher relative error of 5.347% compared to the 4.790%.

We note that the error in the ld-qe parameterization behaves non-monotonically, as the error oscillates with number of nodes after reaching $\approx 0.05\%$ error. Our implementation likely has a source of error that becomes dominant after a certain level of mesh refinement and is not affected by increasing the number of elements further.
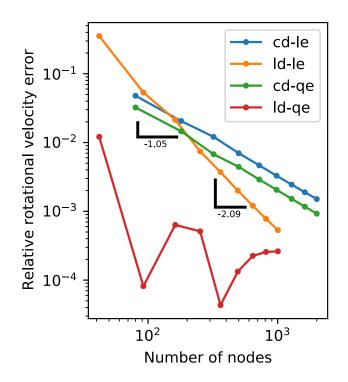
Figure 4.4. Relative error in computing the rotational velocity of a 4-1-1 prolate spheroid in shear flow $v_1^\infty = y, v_2^\infty = v_3^\infty = 0$.

4.4.3 Local errors for linear and quadratic eigenfunctions

Although global errors in translational and rotational velocity are generally small with the BEM method, we will show that this is not the case for local errors. This section will

Table 4.2. Relative error in rotational velocity solution (global error) for a 4-1-1 prolate spheroid in a simple shear flow.

number of elements	cd-le		ld-le		cd-qe		ld-qe	
	nodes	error	nodes	error	nodes	error	nodes	error
80	80	4.790%	42	35.350%	80	3.232%	42	1.211%
180	180	2.052%	92	5.347%	180	1.457%	92	0.008%
320	320	1.210%	162	2.132%	320	0.676%	162	0.063%
500	500	0.699%	252	0.745%	500	0.443%	252	0.051%
720	720	0.466%	362	0.371%	720	0.290%	362	0.004%
980	980	0.328%	492	0.200%	980	0.205%	492	0.013%
1280	1280	0.245%	642	0.121%	1280	0.152%	642	0.023%
1620	1620	0.183%	812	0.078%	1620	0.117%	812	0.026%
2000	2000	0.151%	1002	0.053%	2000	0.092%	1002	0.026%

examine the five rate-of-strain (ROS) and the three quadratic flow eigenfunctions discussed in sections 2.1-2.2, and quantify the local errors created by numerically discretizing the double layer operator. We will show data over a limited subset of flow types and ellipsoid shapes to illustrate the main trends discussed in this study. Further results are included in the supplementary data of this manuscript.
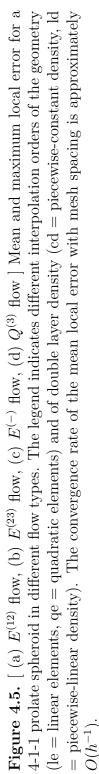
Prolate spheroids

For prolate spheroidal shapes, we will show results for the $E^{(12)}$, $E^{(23)}$, $E^{(-)}$, and $Q^{(3)}$ flows. We note that the flow pairs $E^{(12)}$ and $E^{(31)}$ are equivalent due to particle symmetry, as well as flow pairs $E^{(23)}$ and $E^{(+)}$. The flow $E^{(-)}$ corresponds to uniaxial extension and $Q^{(3)}$ is shown in Fig. 4.2.

4-1-1 ellipsoid:

From the mean local error data shown in Fig. 4.5, we observe that the convergence rate for all of the parameterizations approximately changes with mesh spacing as h^{-1}. For both the piecewise-constant (cd) and piecewise-linear (ld) density parameterizations, we see the mean and maximum local errors either stay the same or get significantly better when going from linear (le) to quadratic (qe) geometry interpolation (i.e., from flat triangles to curved

Figure 4.5. [(a) $E^{(12)}$ flow, (b) $E^{(23)}$ flow, (c) $E^{(-)}$ flow, (d) $Q^{(3)}$ flow] Mean and maximum local error for a 4-1-1 prolate spheroid in different flow types. The legend indicates different interpolation orders of the geometry (le = linear elements, qe = quadratic elements) and of double layer density (cd = piecewise-constant density, ld = piecewise-linear density). The convergence rate of the mean local error with mesh spacing is approximately $\mathcal{O}(h^{-1})$.

| (a) | (b) | (c) | (d) |

Figure 4.6. [(a) cd-le, (b) ld-le, (c) cd-qe, (d) ld-qe] Local errors for a 4-1-1 spheroid in an $E^{(12)}$ flow with an 180 element mesh. We examine different interpolation orders of the geometry (le = linear elements, qe = quadratic elements) and of double layer density (cd = piecewise-constant density, ld = piecewise-linear density). The local errors are represented by colors that scale linearly from 0 (blue) to 0.11 (red).

triangles). This result is expected, as the quadratic geometry interpolation should approximate the spheroid shape more accurately. On the other hand, subfigures Fig. 4.5(a), (b), and (d) show an interesting result – the linear density, linear element (ld-le) parameterization performs either similarly or significantly worse than the constant density, linear element (cd-le) parameterization. For example, the ld-le parameterization for the $E^{(12)}$ flow has significantly higher maximum local errors than the cd-le parameterization. We similarly observe no benefit from the ld-le parameterization in comparison to the cd-le parameterization for the $E^{(23)}$ and $Q^{(3)}$ flows.

One would intuitively expect a piecewise-linear density to perform better than a piecewise-constant density because of the higher order interpolation functions, but the results above suggest otherwise. To understand the origin of these observations in more detail, Fig. 4.6 shows the local errors for an 180 element mesh in a $E^{(12)}$ flow. We observe that ld-le parameterization exhibits large local errors near the poles of the particle, whereas the errors for the cd-le case are not as large. The reason for this is that the ld-le parameterization places nodes at the vertices of the mesh, and hence has nodes lying exactly at the particle's poles that are not well-resolved geometrically. The cd-le parameterization however places nodes at the mesh triangle centroids, and hence avoids having nodes exactly at the poles. On the other hand, the linear density parameterizations do perform significantly better than the constant

density ones in the $E^{(-)}$ flow. Referring back to Fig. 4.1, we observe that the $E^{(-)}$ flow has low magnitude velocities near the poles of the particle. Therefore for the $E^{(-)}$ flow, the ld-le parameterization will not be as affected by the poor node placement at the particle poles; so we recover the expected behavior of the linear order interpolation performing better than constant order. We note that for higher order geometric interpolation (i.e., ld-qe), the high local errors at the poles are no longer present as the curved triangles can now accurately capture the geometry there.

10-1-1 ellipsoid:

Increasing the aspect ratio of the prolate spheroid to 10, we find that the error trends for the parameterizations change significantly (Fig. 4.7). Firstly for the $E^{(12)}$ and $Q^{(3)}$ flow types, quadratic geometry (qe) interpolation (i.e., curved triangles) does not appreciably benefit the mean local error for either the piecewise-constant (cd) or piecewise-linear (ld) density parameterizations. There are even cases where the linear density, quadratic element (ld-qe) parameterization performs worse than the linear density, linear element (ld-le) parameterization ($E^{(23)}$ and $E^{(-)}$). Secondly, the piecewise-linear density (ld) parameterizations consistently perform better than the piecewise-constant density (cd) ones for mean local error.

Fig. 4.8 shows the distributions of local errors on these high aspect ratio particles. We see that the mesh consists of highly elongated elements that can provide a sparse discretization of the densities or a poor geometric representation of the surface. Examining the local error distributions, we find that there are large local errors both at the poles and among the most stretched elements that are along the equator. We observe that the high aspect ratio prolate geometry allows flat linear triangles to serve as mesh elements that mostly approximate the surface well, so the linear geometry interpolation (i.e., flat triangles) performs similarly or better than the quadratic interpolation (i.e., curved triangles). This effect is shown in Fig. 4.8, where little difference is seen in the local error distributions between the linear (le) and the quadratic (qe) element parameterizations. As for why the piecewise-linear densities (ld) perform better than the piecewise-constant densities (cd), the error distribu-
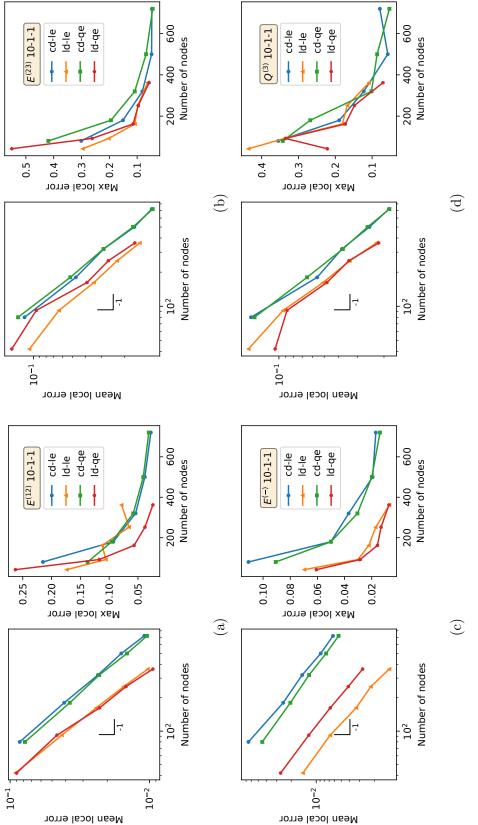
Figure 4.7. [(a) $E^{(12)}$ flow, (b) $E^{(23)}$ flow, (c) $E^{(-)}$ flow, (d) $Q^{(3)}$ flow] Mean and maximum local errors for a 10-1-1 prolate spheroid in different flow types. The legend indicates different interpolation orders of the geometry (le = linear elements, qe = quadratic elements) and of double layer density (cd = piecewise-constant density, ld = piecewise-linear density). The convergence rate of the mean local error with mesh spacing is approximately $\mathcal{O}(h^{-1})$.

(a)	(b)	(c)	(d)
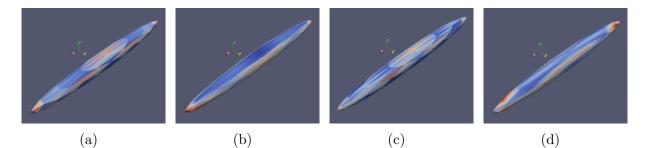
Figure 4.8. [(a) cd-le, (b) ld-le, (c) cd-qe, (d) ld-qe] Local errors for a 10-1-1 spheroid in an $E^{(12)}$ flow with an 180 element mesh. We examine different interpolation orders of the geometry (le = linear elements, qe = quadratic elements) and of double layer density (cd = piecewise-constant density, ld = piecewise-linear density). The local errors values are represented by a linear color scale from 0 (blue) to 0.12 (red).
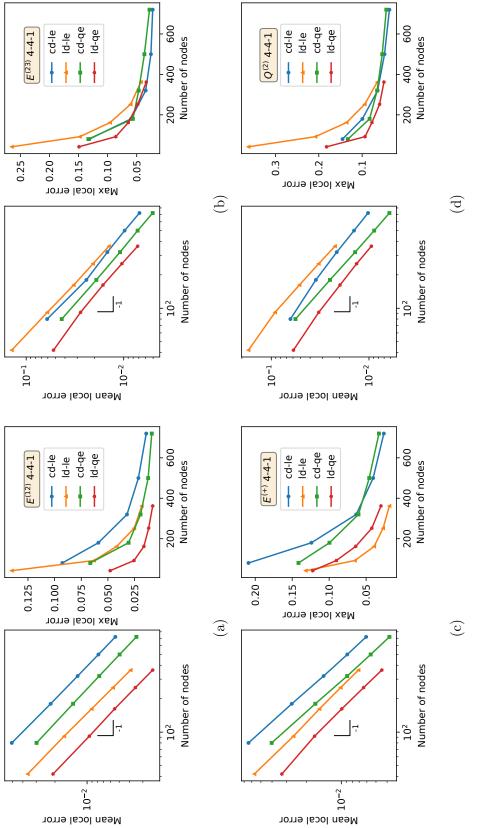
tions show that the piecewise-constant density parameterizations can have large local errors over highly elongated elements. The ld-le parameterization still has large local errors at the particle poles, but this effect is now balanced against the elongated element errors for piecewise-constant densities. Therefore improved accuracy is expected with the higher order interpolation functions.
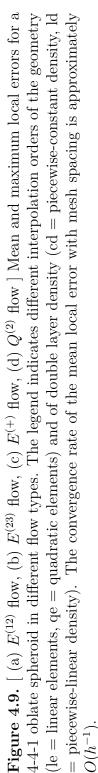
Oblate spheroids

For the oblate spheroidal shapes, we will show results for the $E^{(12)}$, $E^{(23)}$, $E^{(+)}$, and $Q^{(2)}$ flows. Note that the flows $E^{(23)}$ and $E^{(31)}$ are equivalent due to particle symmetry, as well as are $E^{(12)}$ and $E^{(-)}$. The flow $E^{(+)}$ corresponds to uniaxial extension and $Q^{(2)}$ is chosen to be consistent with the choice of $Q^{(3)}$ for the prolate spheroid.

4-4-1 ellipsoid:

Like the results observed for the 4-1-1 prolate spheroid case, the 4-4-1 oblate spheroid also generally sees improvement in the mean local error with quadratic geometry (qe) interpolation over the linear geometry (le) interpolation (i.e., curved triangles compared to flat triangles) (Fig. 4.9). We also observe that the linear density, linear element (ld-le) parameterization performs worse than the constant density, linear element (cd-le) parameterization

Figure 4.9. [(a) $E^{(12)}$ flow, (b) $E^{(23)}$ flow, (c) $E^{(+)}$ flow, (d) $Q^{(2)}$ flow] Mean and maximum local errors for a 4-4-1 oblate spheroid in different flow types. The legend indicates different interpolation orders of the geometry (le = linear elements, qe = quadratic elements) and of double layer density (cd = piecewise-constant density, ld = piecewise-linear density). The convergence rate of the mean local error with mesh spacing is approximately $\mathcal{O}(h^{-1})$.

113

(a)	(b)	(c)	(d)

Figure 4.10. [(a) cd-le, (b) ld-le, (c) cd-qe, (d) ld-qe] Local error heatmaps for the 4-4-1 oblate spheroid with 180 elements in the $E^{(23)}$ flow. We examine different interpolation orders of the geometry (le = linear elements, qe = quadratic elements) and of double layer density (cd = piecewise-constant density, ld = piecewise-linear density). The colors scale linearly with local error from 0 to 0.15; errors larger than or equal to 0.15 are shown as dark red.

for the $E^{(23)}$ and $Q^{(2)}$ flows. As shown in Fig. 4.10, the entire rim region of the disc-like shape has high curvature and is subsequently poorly discretized by the linear elements. The ld-le parameterization has regions of high error at different parts of the rim region depending on the flow type.

10-10-1 ellipsoid:

Moving to the aspect ratio 10 oblate spheroid shape (10-10-1), we find that the quadratic geometry (qe) interpolation does not benefit the accuracy of the simulations significantly (Fig. 4.11). The oblate geometry is mostly flat, as seen in Fig. 4.12, so the same geometry considerations as in the 10-1-1 ellipsoid case apply: the flat linear elements already represent the surface well. The quadratic elements can perform worse than the linear elements for the maximum local error at points near the rim of the oblate shape. Additionally, the piecewise-linear (ld) density parameterization performs significantly better than the piecewise-constant (cd) density parameterization for this shape due to the reasons discussed previously. The geometry closely resembles a flat disc for this particle shape, so it is expected that the piecewise-linear density interpolations lead to better accuracy.

114
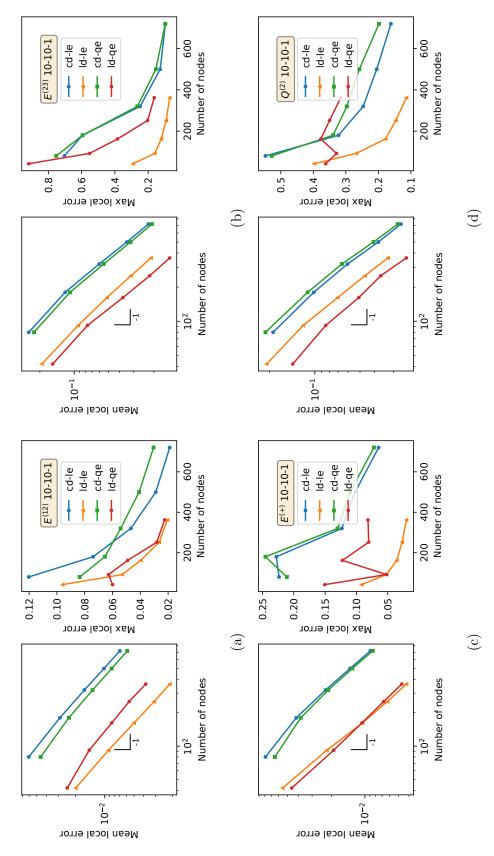
Figure 4.11. [(a) $E^{(12)}$ flow, (b) $E^{(23)}$ flow, (c) $E^{(+)}$ flow, (d) $Q^{(2)}$ flow] Mean and maximum local errors for a 10-10-1 oblate spheroid in different flow types. The legend indicates different interpolation orders of the geometry (le = linear elements, qe = quadratic elements) and of double layer density (cd = piecewise-constant density, ld = piecewise-linear density). The convergence rate of the mean local error scales with mesh spacing approximately as $O(h^{-1})$.

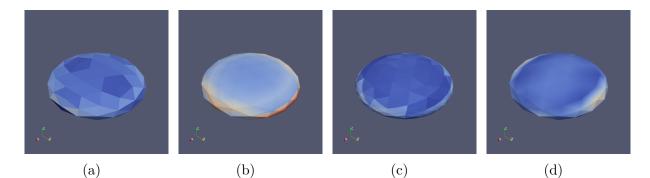|			
(a)	(b)	(c)	(d)
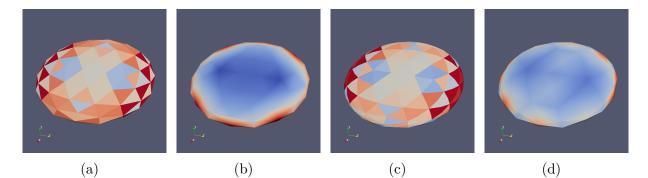
Figure 4.12. [(a) cd-le, (b) ld-le, (c) cd-qe, (d) ld-qe] Local error heatmaps for the 10-10-1 oblate spheroid with 180 elements in the $E^{(+)}$ flow. We examine different interpolation orders of the geometry (le = linear elements, qe = quadratic elements) and of double layer density (cd = piecewise-constant density, ld = piecewise-linear density). The colors scale linearly with local error from 0 to 0.05; errors larger than or equal to 0.05 are shown as dark red.

4.5   Discussion

From the analysis presented here, we have figured out several interesting effects that discretization can have in a BEM implementation. For the ellipsoid shapes considered in this study, many of the local errors arise at the poles of prolate particles and at the rim region of oblate particles. To reduce these local errors, one can locally refine the mesh or use higher order geometry interpolation in the regions. Additionally there is error introduced for mesh elements that are highly elongated, which we observe is particularly pronounced for high aspect ratio particles with piecewise-constant density parameterizations. For the different parameterizations tested, we firstly found that local errors converge at a similar rate of approximately $O(N^{-1})$ by the number of nodes N. Increasing the geometry interpolation order from linear (le) to quadratic (qe) improves the simulation accuracy if the quadratic elements can better represent the desired surface. If the surface is already quite flat to begin with, the addition of quadratic elements will either not improve the local errors significantly or possibly can lead even to worse performance for certain flow types. On the other hand, changing the parameterization of the double layer density from piecewise-constant (cd) to piecewise-linear (ld) has less intuitive results and can sometimes lead to worse accuracy. For certain flow and shape combinations, the piecewise-linear density parameterization produced worse

errors at points where the mesh vertices poorly discretized the target surface shape, such as at the poles of the prolate spheroid as well as at the rim of the oblate spheroid. In these cases, the piecewise-constant density parameterization avoided the large errors because the nodes are located at the centroids of the mesh triangle rather than at the vertices. For other cases, like that of the 10-10-1 oblate spheroid or 10-1-1 prolate spheroid, the piecewise-linear densities performed better than the piecewise-constant densities, due to the fact that the errors at the poles or rim of the particle for the piecewise-linear densities were compensated by more accurate results in the highly elongated elements near the particle equator. In all, this study suggests that local errors converge with mesh refinement, while improving the interpolation orders for the geometry and double layer density does not necessarily reduce errors, as improvement in error depends on the specific mesh geometry and flow type.

4.6 Conclusions

In this study we examined how the discretization of a surface affects the accuracy of the boundary-element method (BEM) for curved 3D geometries. We discretized the Stokes flow double-layer operator over an ellipsoid, and compared the eigenvalues and eigenfunctions of this discretized operator to analytical solutions for different linear and quadratic flow fields. This process allowed us to quantify local errors in the boundary-element method for a wide range of particle aspect ratios, for different meshing representations of the geometry, and interpolations of the double layer density.

The simplistic mesh generation used in this study highlights several discretization pitfalls. Our findings support the notion that additional mesh refinement is generally needed in areas where the surface geometry changes rapidly and also when the elements are highly elongated. We generally find that the local errors are improved ion increasing the geometric interpolation order from linear to quadratic (i.e.,from flat to curved triangles), unless the local system geometry is already well described by the linear elements. Therefore for lower aspect ratio spheroids, one sees quadratic elements perform better than linear elements. As the aspect ratio becomes larger, however, the elements become highly stretched and flattened, which reduces the advantages of quadratic elements. The effects of the double layer density

117

parameterization can have widely different trends depending on the system geometry and flow type. At lower particle aspect ratios, we find cases where piecewise-constant densities can outperform piecewise-linear densities when errors from poor mesh discretization dominate. In other cases, the expected result that the piecewise-linear densities outperformed the piecewise-constant densities was observed. To choose the correct parameterization for the double layer densities, one will have to test a specific use case and determine the minimum interpolation order needed for that system.

4.7 Acknowledgements

4.8 Data Availability Statement

The data that support the findings of this study are available from the corresponding author upon reasonable request.

5. CONCLUSIONS

5.1 Concluding remarks

In this thesis we have studied the dynamics of vesicles in more complex flows and examined how discretization affects the accuracy of the boundary element method. We started with looking at the shape stability of osmotically deflated vesicles in extensional flows with a vorticity component. In the study, we examined vesicles of viscosity ratio 0.01 to 5.0 and reduced volume from 0.6 to 0.70; finding that the critical capillary number can be inferred from the purely extensional flow results for up to moderate amounts of vorticity in the flow. As the flow type becomes close to a shear flow, a shape deviation appears that decreases the tension along the vesicle leading to a higher critical capillary number. This study informs future experimental studies that can have breakup of cell-like particles and provides insight into why the shape of vesicles does not become unstable in purely shear flows.

We also presented a project that considers the dynamics of quasispherical vesicles in large amplitude oscillatory extension. The microfluidic experiments and numerical simulations show there to be three dynamical regimes resulting from a competition between the flow frequency and the flow strength. We find that the vesicle can deform asymmetrically within a strain rate cycle even at steady state, resulting in interesting effects on the bulk suspension rheology. From a bigger picture perspective, this fundamental study is a first step into the transient dynamics of cell-like particles in time-dependent flows.

Finally we examined how discretization affects the numerics of the simulation method used throughout the previous projects. Using the analytical solutions for the double layer operator of an ellipsoid in linear and quadratic flows, we find several non-intuitive discretization errors. For example, depending on the aspect ratio of the particle and the meshing method, increasing the interpolation order of the double layer density from piecewise constant to piecewise linear can produce worse local errors. Factors such as the meshing near high curvature regions, the number of highly stretched elements, and the flatness of the particle geometry lead to the observed results. Overall, this study reinforces the need for rigorous error testing of numerical simulations using the boundary element method and highlights some non-intuitive error sources.

5.2 Directions for future research

5.2.1 Vesicle dynamics in oscillatory shear

A straightforward addition to the literature would be a study on vesicle dynamics in oscillatory shear. As mentioned in the previous chapters, vesicles undergo interesting rotational dynamics in steady shear flow, so an oscillatory shear study could examine how those dynamics might affect the rheology of a cell-like suspension. We expect that the vesicle dynamics in oscillatory shear will have even more interesting dynamics than those observed in extensional flows. Of particular interest would be how the tank-treading/tumbling/vacillating-breathing dynamics are affected the oscillatory flow frequency. With completed studies on vesicle dynamics in oscillatory shear and extension, we will have a much deeper picture into the nonlinear rheology of cell-like dispersions. For the simulations, one would need to add an oscillatory shear external flow and a base shear rate. All other formulation and numerics would be the same as those shown in the previous chapters.

5.2.2 Multicomponent vesicle dynamics

The vesicle research presented in this thesis has examined the dynamics of single component lipid membranes in mixed flows and oscillatory extension. While single component lipid membranes are commonly created experimentally, in biological contexts vesicles often have multiple membrane components consisting of different lipid species, cholesterol, and possibly proteins. As a step in improving our understanding of these complex membranes, we can examine vesicles with multiple lipid phases. These multicomponent lipid membranes will experience phase separation, which plays a key role in biological processes such as vesicle budding, fusion in cells, or the formation of lipid rafts [53], [149]–[151]. A common ternary mixture used to for synthetic multicomponent vesicles is unsaturated DOPC lipid (1,2-dioleoyl-sn-glycero-3-phosphocholine), saturated DPPC lipid (dipalmitoylphosphatidylcholine), and cholesterol [152]. Previous literature on multicomponent vesicles have examined their equilibrium configurations [152]–[154], with some three-dimensional numerical work on their dynamics in steady shear flow [155]. There is a gap in the literature on how non-

equilibrium conditions in physiological flows or microfluidic processing affect the dynamics of these vesicles. How the flow affects the thermodynamics and the kinetics of the domain formation is also not well understood.

We have started designing numerical simulations and constructing microfluidic experiments to examine the dynamics of multicomponent vesicles in flow. Here we briefly describe the additions to the original boundary element vesicle model presented to handle the multicomponent case. A more complete description of the formulation can be found in [156]. To model a multicomponent vesicle, one must have dynamical equations that solve for the vesicle shape as well as the membrane concentration field. Two new energy terms are added to the membrane free energy functional, the phase-field energy and Gaussian curvature energy. The phase-field energy is a free energy contribution in terms of the membrane concentration field that takes into account the energy between the phases and the line tension. The Gaussian curvature can now have a non-zero energy contribution if the phases have different Gaussian curvatures. Solving the system will require solving original BEM equations for the velocity field over the vesicle surface, along with a convection-diffusion equation for the membrane components. Note that the membrane components move along gradients of chemical potentials from the membrane free energy. This project will provide the first set of quantitative studies on the dynamics of multicomponent vesicles in microfluidic automated flow control and direct boundary element simulations.

REFERENCES

[1] C. P. Martin, S. Wang, and S. Kim, "Surface tractions on an ellipsoid in stokes flow: Quadratic ambient fields," *Physics of Fluids*, vol. 31, no. 2, p. 021 209, 2019.

[2] S. Yang, A. Ündar, and J. D. Zahn, "A microfluidic device for continuous, real time blood plasma separation," *Lab on a Chip*, vol. 6, no. 7, pp. 871–880, 2006.

[3] Z. T. F. Yu, K. M. Aw Yong, and J. Fu, "Microfluidic blood cell sorting: Now and beyond," *Small*, vol. 10, no. 9, pp. 1687–1703, 2014.

[4] G. Du, Q. Fang, and J. M. den Toonder, "Microfluidics for cell-based high throughput screening platforms—a review," *Analytica chimica acta*, vol. 903, pp. 36–50, 2016.

[5] A. T. Santoso, X. Deng, J.-H. Lee, *et al.*, "Microfluidic cell-phoresis enabling high-throughput analysis of red blood cell deformability and biophysical screening of antimalarial drugs," *Lab on a Chip*, vol. 15, no. 23, pp. 4451–4460, 2015.

[6] A. A. S. Bhagat, H. W. Hou, L. D. Li, C. T. Lim, and J. Han, "Pinched flow coupled shear-modulated inertial microfluidics for high-throughput rare blood cell separation," *Lab on a Chip*, vol. 11, no. 11, pp. 1870–1878, 2011.

[7] R. Dimova and C. Marques, *The Giant Vesicle Book*. CRC Press, 2019.

[8] J. B. Freund, "Numerical simulation of flowing blood cells," *Annual review of fluid mechanics*, vol. 46, pp. 67–95, 2014.

[9] D. Barthes-Biesel, "Motion and deformation of elastic capsules and vesicles in flow," *Annual Review of fluid mechanics*, vol. 48, pp. 25–52, 2016.

[10] D. Boal, *Mechanics of the cell Cambridge*. UK: Cambridge University Press, 2002.

[11] V. Noireaux and A. Libchaber, "A vesicle bioreactor as a step toward an artificial cell assembly," *Proceedings of the National Academy of Sciences*, vol. 101, no. 51, pp. 17 669–17 674, 2004.

[12] E. M. Johnson-Chavarria, U. Agrawal, M. Tanyeri, T. E. Kuhlman, and C. M. Schroeder, "Automated single cell microbioreactor for monitoring intracellular dynamics and cell growth in free solution," *Lab on a Chip*, vol. 14, no. 15, pp. 2688–2697, 2014.

[13] S.-i. M. Nomura, K. Tsumoto, T. Hamada, K. Akiyoshi, Y. Nakatani, and K. Yoshikawa, "Gene expression within cell-sized lipid vesicles," *ChemBioChem*, vol. 4, no. 11, pp. 1172–1175, 2003.

[14] H. Saito, Y. Kato, M. Le Berre, *et al.*, "Time-resolved tracking of a minimum gene expression system reconstituted in giant liposomes," *ChemBioChem*, vol. 10, no. 10, pp. 1640–1643, 2009.

[15] W. Helfrich, "Elastic properties of lipid bilayers: Theory and possible experiments," *Zeitschrift für Naturforschung C*, vol. 28, pp. 693–703, 1973.

[16] D. Abreu, M. Levant, V. Steinberg, and U. Seifert, "Fluid vesicles in flow," *Advances in colloid and interface science*, vol. 208, pp. 129–141, 2014.

[17] J. Henriksen and J. Ipsen, "Measurement of membrane elasticity by micro-pipette aspiration," *The European Physical Journal E*, vol. 14, no. 2, pp. 149–167, 2004, ISSN: 1292-8941.

[18] H. Deuling and W. Helfrich, "The curvature elasticity of fluid membranes: A catalogue of vesicle shapes," *Journal de Physique*, vol. 37, no. 11, pp. 1335–45, 1976. DOI: 10.1051/jphys:01976003701101335500.

[19] U. Seifert, "Configurations of fluid membranes and vesicles," *Advances in Physics*, vol. 46, no. 1, pp. 13–137, 1997, ISSN: 0001-8732.

[20] C. Misbah, "Vacillating breathing and tumbling of vesicles under shear flow," *Physical review letters*, vol. 96, no. 2, p. 028 104, 2006.

[21] M.-A. Mader, V. Vitkova, M. Abkarian, A. Viallat, and T. Podgorski, "Dynamics of viscous vesicles in shear flow," *The European Physical Journal E*, vol. 19, no. 4, pp. 389–397, 2006.

[22] P. M. Vlahovska and R. S. Gracia, "Dynamics of a viscous vesicle in linear flows," *Phys. Rev. E.*, 2007.

[23] J. Deschamps, V. Kantsler, E. Segre, and V. Steinberg, "Dynamics of a vesicle in general flow," *Proceedings of the National Academy of Sciences*, vol. 106, no. 28, pp. 11 444–11 447, 2009, ISSN: 0027-8424. DOI: 10.1073/pnas.0902657106. eprint: http://www.pnas.org/content/106/28/11444.full.pdf. [Online]. Available: http://www.pnas.org/content/106/28/11444.

[24] V. Kantsler and V. Steinberg, "Orientation and dynamics of a vesicle in tank-treading motion in shear flow," *Phys. Rev. Lett.*, vol. 95, p. 258 101, 25 2005. DOI: 10.1103/PhysRevLett.95.258101.

[25] V. Kantsler and V. Steinberg, "Transition to tumbling and two regimes of tumbling motion of a vesicle in shear flow," *Phys. Rev. Lett.*, vol. 96, p. 036 001, 3 2006. DOI: 10.1103/PhysRevLett.96.036001.

[26] V. Lebedev, K. Turitsyn, and S. Vergeles, "Dynamics of nearly spherical vesicles in an external flow," *Physical review letters*, vol. 99, no. 21, p. 218 101, 2007.

[27] G. Danker, T. Biben, T. Podgorski, C. Verdier, and C. Misbah, "Dynamics and rheology of a dilute suspension of vesicles: Higher-order theory," *Physical Review E*, vol. 76, no. 4, p. 041 905, 2007.

[28] A. Farutin, T. Biben, and C. Misbah, "Analytical progress in the theory of vesicles under linear flow," *Phys. Rev. E*, vol. 81, p. 061 904, 6 2010. DOI: 10.1103/PhysRevE.81.061904.

[29] P. M. Vlahovska, T. Podgorski, and C. Misbah, "Vesicles and red blood cells in flow: From individual dynamics to rheology," *Comptes rendus - Physique*, vol. 10, no. 8, pp. 775–789, 2009, ISSN: 1631-0705.

[30] V. Kantsler, E. Segre, and V. Steinberg, "Dynamics of interacting vesicles and rheology of vesicle suspension in shear flow," *EPL (Europhysics Letters)*, vol. 82, no. 5, 2008, ISSN: 0295-5075.

[31] V. Narsimhan, A. Spann, and E. Shaqfeh, "The mechanism of shape instability for a vesicle in extensional flow," *Journal of Fluid Mechanics*, vol. 750, pp. 144–190, 2014. DOI: 10.1017/jfm.2014.248.

[32] V. Narsimhan, A. Spann, and E. Shaqfeh, "Pearling, wrinkling, and buckling of vesicles in elongational flows," *Journal of Fluid Mechanics*, vol. 777, pp. 1–26, 2015. DOI: 10.1017/jfm.2015.345.

[33] D. Kumar, C. M. Richter, and C. M. Schroeder, "Conformational dynamics and phase behavior of lipid vesicles in a precisely controlled extensional flow," *Soft Matter*, vol. 16, no. 2, pp. 337–347, 2020.

[34] J. B. Dahl, V. Narsimhan, B. Gouveia, S. Kumar, E. S. Shaqfeh, and S. J. Muller, "Experimental observation of the asymmetric instability of intermediate-reduced-volume vesicles in extensional flow," *Soft Matter*, vol. 12, no. 16, pp. 3787–3796, 2016.

[35] A. P. Spann, H. Zhao, and E. S. G. Shaqfeh, "Loop subdivision surface boundary integral method simulations of vesicles at low reduced volume ratio in shear and extensional flow," *Physics of Fluids*, vol. 26, no. 3, p. 031 902, 2014. DOI: 10.1063/1.4869307. eprint: https://doi.org/10.1063/1.4869307.

[36] D. Kumar, C. M. Richter, and C. M. Schroeder, "Double-mode relaxation of highly deformed anisotropic vesicles," *Physical Review E*, vol. 102, no. 1, p. 010 605, 2020.

[37] W. Rawicz, K. Olbrich, T. McIntosh, D. Needham, and E. Evans, "Effect of chain length and unsaturation on elasticity of lipid bilayers," *Biophysical Journal*, vol. 79, no. 1, pp. 328–339, 2000, ISSN: 0006-3495. DOI: 10.1016/S0006-3495(00)76295-3. [Online]. Available: http://www.sciencedirect.com/science/article/pii/S0006349500762953.

[38] H. Noguchi and G. Gompper, "Dynamics of fluid vesicles in shear flow: Effect of membrane viscosity and thermal fluctuations," *Physical Review E*, vol. 72, no. 1, p. 011 901, 2005.

[39] C. S. Peskin, "The immersed boundary method," *Acta Numerica*, vol. 11, pp. 479–517, 2002. DOI: 10.1017/S0962492902000077.

[40] Y. Kim and M.-C. Lai, "Simulating the dynamics of inextensible vesicles by the penalty immersed boundary method," *Journal of Computational Physics*, vol. 229, no. 12, pp. 4840–4853, 2010.

[41] G. Tryggvason, B. Bunner, A. Esmaeeli, *et al.*, "A front-tracking method for the computations of multiphase flow," *Journal of computational physics*, vol. 169, no. 2, pp. 708–759, 2001.

[42] A. Yazdani and P. Bagchi, "Three-dimensional numerical simulation of vesicle dynamics using a front-tracking method," *Physical Review E*, vol. 85, no. 5, p. 056 308, 2012.

[43] Pozrikidis, *Boundary integral and singularity methods for linearized viscous flow*. Cambridge University Press, 1992.

[44] F. Cirak, M. Ortiz, and P. Schröder, "Subdivision surfaces: A new paradigm for thin-shell finite-element analysis," *International Journal for Numerical Methods in Engineering*, vol. 47, no. 12, pp. 2039–2072, 2000.

[45] S. Mousavi and N. Sukumar, "Generalized duffy transformation for integrating vertex singularities," *Computational Mechanics*, vol. 45, no. 2-3, p. 127, 2010.

[46] S. Kim and S. J. Karrila, *Microhydrodynamics: principles and selected applications*. Courier Corporation, 1991.

[47] H. Zhao and E. S. Shaqfeh, "The dynamics of a non-dilute vesicle suspension in a simple shear flow," *Journal of Fluid Mechanics*, vol. 725, pp. 709–731, 2013. DOI: 10.1017/jfm.2013.207.

[48] C. Lin and V. Narsimhan, "Shape stability of deflated vesicles in general linear flows," *Physical Review Fluids*, vol. 4, no. 12, p. 123 606, 2019.

[49] M. I. Angelova and D. S. Dimitrov, "Liposome electroformation," *Faraday discussions of the Chemical Society*, vol. 81, pp. 303–311, 1986.

[50] R. Dimova, S. Aranda, N. Bezlyepkina, V. Nikolov, K. A. Riske, and R. Lipowsky, "A practical guide to giant vesicles. probing the membrane nanoregime via optical microscopy," *Journal of Physics: Condensed Matter*, vol. 18, no. 28, S1151, 2006. [Online]. Available: http://stacks.iop.org/0953-8984/18/i=28/a=S04.

[51] B. Kaoui, G. Biros, and C. Misbah, "Why do red blood cells have asymmetric shapes even in a symmetric flow?" *Phys. Rev. Lett.*, vol. 103, p. 188 101, 18 2009. DOI: 10.1103/PhysRevLett.103.188101.

[52] M. Abkarian and A. Viallat, "Vesicles and red blood cells in shear flow," *Soft Matter*, vol. 4, no. 4, pp. 653–657, 2008.

[53] B. Alberts, A. Johnson, J. Lewis, and et al., *Molecular Biology of the Cell*, fourth. Garland Science, 2002.

[54] C. Settembre, A. Fraldi, D. L. Medina, and A. Ballabio, "Signals for the lysosome: A control center for cellular clearance and energy metabolism," *Nat Rev Mol Cell Biol*, vol. 14, no. 5, pp. 283–296, 2013, 23609508[pmid], ISSN: 1471-0072. DOI: 10.1038/nrm3565. [Online]. Available: http://www.ncbi.nlm.nih.gov/pmc/articles/PMC4387238/.

[55] G. Raposo and W. Stoorvogel, "Extracellular vesicles: Exosomes, microvesicles, and friends," *The Journal of Cell Biology*, vol. 200, no. 4, pp. 373–383, 2013, ISSN: 0021-9525. DOI: 10.1083/jcb.201211138. eprint: http://jcb.rupress.org/content/200/4/373.full.pdf. [Online]. Available: http://jcb.rupress.org/content/200/4/373.

[56] G. Gregoriadis, "Engineering liposomes for drug delivery: Progress and problems," *Trends in Biotechnology*, vol. 13, no. 12, pp. 527–537, 1995, ISSN: 0167-7799. DOI: 10.1016/S0167-7799(00)89017-4. [Online]. Available: http://www.sciencedirect.com/science/article/pii/S0167779900890174.

[57] R. Muzzalupo and L. Tavano, "Niosomal drug delivery for transdermal targeting: Recent advances," *Research and reports in transdermal drug delivery*, vol. 4, pp. 23–33, 2015.

[58] M. Karlsson, M. Davidson, R. Karlsson, *et al.*, "Biomimetic nanoscale reactors and networks," *Annual Review of Physical Chemistry*, vol. 55, no. 1, pp. 613–649, 2004, PMID: 15117264. DOI: 10.1146/annurev.physchem.55.091602.094319. eprint: https://doi.org/10.1146/annurev.physchem.55.091602.094319.

[59] K. Khairy and J. Howard, "Minimum-energy vesicle and cell shapes calculated using spherical harmonics parameterization," *Soft Matter*, vol. 7, no. 5, pp. 2138–2143, 2011.

[60] V. Kantsler, E. Segre, and V. Steinberg, "Critical dynamics of vesicle stretching transition in elongational flow," *Phys. Rev. Lett.*, vol. 101, no. 4, 2008, ISSN: 0031-9007.

[61] J. Spjut, "Trapping, deformation, and dynamics of phospholipid vesicles.," Ph.D. dissertation, University of California, Berkeley, 2010.

[62] J. Deschamps, V. Kantsler, and V. Steinberg, "Phase diagram of single vesicle dynamical states in shear flow," *Phys. Rev. Lett.*, vol. 102, p. 118 105, 11 2009. DOI: 10.1103/PhysRev Lett.102.118105.

[63] D. Barthes-Biesel and A. Acrivos, "Deformation and burst of a liquid droplet freely suspended in a linear shear field," *Journal of Fluid Mechanics*, vol. 61, no. 1, pp. 1–22, 1973.

[64] B. Bentley and L. G. Leal, "An experimental investigation of drop deformation and breakup in steady, two-dimensional linear flows," *Journal of Fluid Mechanics*, vol. 167, pp. 241–283, 1986.

[65] H. Zhao and E. S. G. Shaqfeh, "The dynamics of a vesicle in simple shear flow," *Journal of Fluid Mechanics*, vol. 674, pp. 578–604, 2011, ISSN: 0022-1120.

[66] G. Boedec, M. Leonetti, and M. Jaeger, "3d vesicle dynamics simulations with a linearly triangulated surface," *Journal of Computational Physics*, vol. 230, no. 4, pp. 1020–1034, 2011, ISSN: 0021-9991. DOI: 10.1016/j.jcp.2010.10.021. [Online]. Available: http://www.sciencedirect.com/science/article/pii/S0021999110005772.

[67] H.-G. Dobereiner, O. Selchow, and R. Lipowsky, "Spontaneous curvature of fluid vesicles induced by trans-bilayer sugar asymmetry," *European Biophysics Journal*, vol. 28, no. 2, pp. 174–178, 1999, ISSN: 0175-7571.

[68] L. Bagatolli and P. S. Kumar, "Phase behavior of multicomponent membranes: Experimental and computational techniques," *Soft Matter*, vol. 5, no. 17, pp. 3234–3248, 2009.

[69] H. Zhao and E. S. G. Shaqfeh, "The shape stability of a lipid vesicle in a uniaxial extensional flow," *Journal of Fluid Mechanics*, vol. 719, pp. 345–361, 2013. DOI: 10.1017/jfm.2013.10.

[70] M. Loewenberg and E. Hinch, "Numerical simulation of a concentrated emulsion in shear flow," *Journal of Fluid Mechanics*, vol. 321, pp. 395–419, 1996.

[71] A. Moreira and M. Y. Santos, "Concave hull: A k-nearest neighbours approach for the computation of the region occupied by a set of points," 2007.

[72] H. Karam and J. Bellinger, "Deformation and breakup of liquid droplets in a simple shear field," *Industrial & Engineering Chemistry Fundamentals*, vol. 7, no. 4, pp. 576–581, 1968.

[73] H. A. Stone, "Dynamics of drop deformation and breakup in viscous fluids," *Annual Review of Fluid Mechanics*, vol. 26, no. 1, pp. 65–102, 1994, ISSN: 0066-4189.

[74] S. R. Keller and R. Skalak, "Motion of a tank-treading ellipsoidal particle in a shear flow," *Journal of Fluid Mechanics*, vol. 120, pp. 27–47, 1982.

[75] C. Lin, D. Kumar, C. M. Richter, S. Wang, C. M. Schroeder, and V. Narsimhan, "Vesicle dynamics in large amplitude oscillatory extensional flow," *Journal of Fluid Mechanics*, vol. 929, A43, 2021. DOI: 10.1017/jfm.2021.885.

[76] S.-L. Huang and R. C. MacDonald, "Acoustically active liposomes for drug encapsulation and ultrasound-triggered release," *Biochimica et Biophysica Acta (BBA)-Biomembranes*, vol. 1665, no. 1-2, pp. 134–141, 2004.

[77] H. Zhou, B. B. Gabilondo, W. Losert, and W. van de Water, "Stretching and relaxation of vesicles," *Physical Review E*, vol. 83, no. 1, p. 011 905, 2011.

[78] M. Yu, R. B. Lira, K. A. Riske, R. Dimova, and H. Lin, "Ellipsoidal relaxation of deformed vesicles," *Physical review letters*, vol. 115, no. 12, p. 128 303, 2015.

[79] N. Callens, C. Minetti, G. Coupier, *et al.*, "Hydrodynamic lift of vesicles under shear flow in microgravity," *EPL (Europhysics Letters)*, vol. 83, no. 2, p. 24 002, 2008. [Online]. Available: http://stacks.iop.org/0295-5075/83/i=2/a=24002.

[80] T. Podgorski, N. Callens, C. Minetti, G. Coupier, F. Dubois, and C. Misbah, "Dynamics of vesicle suspensions in shear flow between walls," *Microgravity Science and Technology*, vol. 23, no. 2, pp. 263–270, 2011, ISSN: 0938-0108.

[81] H. Zhao, A. P. Spann, and E. S. G. Shaqfeh, "The dynamics of a vesicle in a wall-bound shear flow," *Physics of Fluids*, vol. 23, no. 12, 2011, ISSN: 1070-6631.

[82] V. Vitkova, M.-A. Mader, B. Polack, C. Misbah, and T. Podgorski, "Micro-macro link in rheology of erythrocyte and vesicle suspensions," *Biophysical Journal*, vol. 95, no. 6, pp. L33–L35, 2008, ISSN: 0006-3495.

[83] N. J. Zabusky, E. Segre, J. Deschamps, V. Kantsler, and V. Steinberg, "Dynamics of vesicles in shear and rotational flows: Modal dynamics and phase diagram," *Physics of Fluids*, vol. 23, no. 4, 2011, ISSN: 1070-6631.

[84] M. Levant, J. Deschamps, E. Afik, and V. Steinberg, "Characteristic spatial scale of vesicle pair interactions in a plane linear flow," *Phys. Rev. E*, vol. 85, p. 056 306, 5 2012. DOI: 10.1103/PhysRevE.85.056306.

[85] D. Abreu and U. Seifert, "Noisy nonlinear dynamics of vesicles in flow," *Phys. Rev. Lett.*, vol. 110, no. 23, 2013, ISSN: 0031-9007.

[86] L. G. Leal, *Laminar flow and convective transport processes: scaling principles and asymptotic analysis*. Butterworth-Heinemann Boston: 1992.

[87] A. Shenoy, C. V. Rao, and C. M. Schroeder, "Stokes trap for multiplexed particle manipulation and assembly using fluidics," *Proceedings of the National Academy of Sciences*, vol. 113, no. 15, pp. 3976–3981, 2016, ISSN: 0027-8424. DOI: 10.1073/pnas.1525162113. eprint: http://www.pnas.org/content/113/15/3976.full.pdf. [Online]. Available: http://www.pnas.org/content/113/15/3976.

[88] A. Shenoy, D. Kumar, S. Hilgenfeldt, and C. M. Schroeder, "Flow topology during multiplexed particle manipulation using a stokes trap," *Physical Review Applied*, vol. 12, no. 5, p. 054 010, 2019.

[89] D. Kumar, A. Shenoy, J. Deutsch, and C. M. Schroeder, "Automation and flow control for particle manipulation," *Current Opinion in Chemical Engineering*, vol. 29, pp. 1–8, 2020.

[90] D. Kumar, A. Shenoy, S. Li, and C. M. Schroeder, "Orientation control and nonlinear trajectory tracking of colloidal particles using microfluidics," *Physical Review Fluids*, vol. 4, no. 11, p. 114 203, 2019.

[91] A. Shenoy, M. Tanyeri, and C. M. Schroeder, "Characterizing the performance of the hydrodynamic trap using a control-based approach," *Microfluidics and Nanofluidics*, vol. 18, no. 5-6, pp. 1055–1066, 2015.

[92] V. Kantsler, E. Segre, and V. Steinberg, "Vesicle dynamics in time-dependent elongation flow: Wrinkling instability," *Physical review letters*, vol. 99, no. 17, p. 178 102, 2007.

[93] P. Domachuk, K. Tsioris, F. G. Omenetto, and D. L. Kaplan, "Bio-microfluidics: Bio-materials and biomimetic designs," *Advanced materials*, vol. 22, no. 2, pp. 249–260, 2010.

[94] D. Lim, Y. Kamotani, B. Cho, J. Mazumder, and S. Takayama, "Fabrication of microfluidic mixers and artificial vasculatures using a high-brightness diode-pumped nd:yag laser direct write method," *Lab Chip*, vol. 3, pp. 318–323, 4 2003. DOI: 10.1039/B308452C.

[95] S. H. Bryngelson and J. B. Freund, "Non-modal floquet stability of capsules in large-amplitude oscillatory extensional flow," *European Journal of Mechanics-B/Fluids*, vol. 77, pp. 171–176, 2019.

[96] M. I. Angelova, S. Soléau, P. Méléard, F. Faucon, and P. Bothorel, "Preparation of giant vesicles by external ac electric fields. kinetics and applications," in *Trends in Colloid and Interface Science VI*, C. Helm, M. Lösche, and H. Möhwald, Eds., Darmstadt: Steinkopff, 1992, pp. 127–131, ISBN: 978-3-7985-1680-9.

[97] Y. Zhou and C. M. Schroeder, "Transient and average unsteady dynamics of single polymers in large-amplitude oscillatory extension," *Macromolecules*, vol. 49, no. 20, pp. 8018–8030, 2016.

[98] Y. Zhou and C. M. Schroeder, "Single polymer dynamics under large amplitude oscillatory extension," *Physical Review Fluids*, vol. 1, no. 5, p. 053 301, 2016.

[99] M. G. Duffy, "Quadrature over a pyramid or cube of integrands with a singularity at a vertex," *SIAM journal on Numerical Analysis*, vol. 19, no. 6, pp. 1260–1262, 1982.

[100] K. Turitsyn and S. Vergeles, "Wrinkling of vesicles during transient dynamics in elongational flow," *Physical review letters*, vol. 100, no. 2, p. 028 103, 2008.

[101] X. Li and K. Sarkar, "Drop dynamics in an oscillating extensional flow at finite reynolds numbers," *Physics of fluids*, vol. 17, no. 2, p. 027 103, 2005.

[102] X. Li and K. Sarkar, "Numerical investigation of the rheology of a dilute emulsion of drops in an oscillating extensional flow," *Journal of non-newtonian fluid mechanics*, vol. 128, no. 2-3, pp. 71–82, 2005.

[103] G. Danker, C. Verdier, and C. Misbah, "Rheology and dynamics of vesicle suspension in comparison with droplet emulsion," *Journal of Non-Newtonian Fluid Mechanics*, vol. 152, no. 1, pp. 156–167, 2008, 4th International workshop on Nonequilibrium Theromdynamics and Complex Fluids, ISSN: 0377-0257. DOI: 10.1016/j.jnnfm.2007.07.005. [Online]. Available: http://www.sciencedirect.com/science/article/pii/S0377025707001620.

[104] A. Farutin and C. Misbah, "Rheology of vesicle suspensions under combined steady and oscillating shear flows," *Journal of fluid mechanics*, vol. 700, p. 362, 2012.

[105] K. Hyun, M. Wilhelm, C. O. Klein, *et al.*, "A review of nonlinear oscillatory shear tests: Analysis and application of large amplitude oscillatory shear (laos)," *Progress in Polymer Science*, vol. 36, no. 12, pp. 1697–1753, 2011.

[106] M. Wilhelm, "Fourier-transform rheology," *Macromolecular materials and engineering*, vol. 287, no. 2, pp. 83–105, 2002.

[107] Y. Y. Avital and O. Farago, "Small membranes under negative surface tension," *The Journal of chemical physics*, vol. 142, no. 12, 03B619_1, 2015.

[108] A. Sakashita, N. Urakami, P. Ziherl, and M. Imai, "Three-dimensional analysis of lipid vesicle transformations," *Soft Matter*, vol. 8, no. 33, pp. 8569–8581, 2012.

[109] P. Ziherl and S. Svetina, "Nonaxisymmetric phospholipid vesicles: Rackets, boomerangs, and starfish," *EPL (Europhysics Letters)*, vol. 70, no. 5, p. 690, 2005.

[110] A. Kodama, M. Morandi, R. Ebihara, *et al.*, "Migration of deformable vesicles induced by ionic stimuli," *Langmuir*, vol. 34, no. 38, pp. 11 484–11 494, 2018.

[111] A. Farutin and C. Misbah, "Squaring, parity breaking, and s tumbling of vesicles under shear flow," *Physical review letters*, vol. 109, no. 24, p. 248 106, 2012.

[112] C. Lin, S. Wang, V. Narsimhan, and S. Kim, "Surface discretization considerations for the boundary-element method applied to three-dimensional ellipsoidal particles in stokes flow," *Physics of Fluids*, vol. 33, no. 11, p. 113 106, 2021.

[113] J. Vincent, N. Phan-Thien, and T. Tran-Cong, "Sedimentation of multiple particles of arbitrary shape," *Journal of rheology*, vol. 35, no. 1, pp. 1–27, 1991.

[114] T. Y. Hou, J. S. Lowengrub, and M. J. Shelley, "Boundary integral methods for multicomponent fluids and multiphase materials," *Journal of Computational Physics*, vol. 169, no. 2, pp. 302–362, 2001.

[115] C. Sorgentone, A.-K. Tornberg, and P. M. Vlahovska, "A 3d boundary integral method for the electrohydrodynamics of surfactant-covered drops," *Journal of Computational Physics*, vol. 389, pp. 111–127, 2019.

[116] J. R. Gissinger, A. Z. Zinchenko, and R. H. Davis, "Drop squeezing between arbitrary smooth obstacles," *Journal of Fluid Mechanics*, vol. 908, 2021.

[117] M. S. Ingber, S. Feng, A. L. Graham, and H. Brenner, "The analysis of self-diffusion and migration of rough spheres in nonlinear shear flow using a traction-corrected boundary element method," *Journal of Fluid Mechanics*, vol. 598, p. 267, 2008.

[118] W. Yan, E. Corona, D. Malhotra, S. Veerapaneni, and M. Shelley, "A scalable computational platform for particulate stokes suspensions," *Journal of Computational Physics*, vol. 416, p. 109 524, 2020.

[119] C.-W. Tai, S. Wang, and V. Narsimhan, "Cross-stream migration of non-spherical particles in a second-order fluid–theories of particle dynamics in arbitrary quadratic flows," *J. Fluid Mech*, vol. 895, no. A6, 2020.

[120] A. Z. Zinchenko and R. H. Davis, "Motion of deformable drops through porous media," *Annual Review of Fluid Mechanics*, vol. 49, pp. 71–90, 2017.

[121] V. Cristini and Y.-C. Tan, "Theory and numerical simulation of droplet dynamics in complex flows—a review," *Lab on a Chip*, vol. 4, no. 4, pp. 257–264, 2004.

[122] S. L. Anna, "Droplets and bubbles in microfluidic devices," *Annual Review of Fluid Mechanics*, vol. 48, pp. 285–309, 2016.

[123] S.-Y. Park and P. Dimitrakopoulos, "Transient dynamics of an elastic capsule in a microfluidic constriction," *Soft matter*, vol. 9, no. 37, pp. 8844–8855, 2013.

[124] A. Koolivand and P. Dimitrakopoulos, "Motion of an elastic capsule in a trapezoidal microchannel under stokes flow conditions," *Polymers*, vol. 12, no. 5, p. 1144, 2020.

[125] A. Rahimian, I. Lashuk, S. Veerapaneni, *et al.*, "Petascale direct numerical simulation of blood flow on 200k cores and heterogeneous architectures," in *SC'10: Proceedings of the 2010 ACM/IEEE International Conference for High Performance Computing, Networking, Storage and Analysis*, IEEE, 2010, pp. 1–11.

[126] S. K. Veerapaneni, A. Rahimian, G. Biros, and D. Zorin, "A fast algorithm for simulating vesicle flows in three dimensions," *Journal of Computational Physics*, vol. 230, no. 14, pp. 5610–5634, 2011.

[127] G. C. Hsiao and W. L. Wendland, *Boundary integral equations*. Springer, 2008.

[128] Q. Huang and T. Cruse, "Some notes on singular integral techniques in boundary element analysis," *International journal for numerical methods in engineering*, vol. 36, no. 15, pp. 2643–2659, 1993.

[129] D. N. Arnold and W. L. Wendland, "On the asymptotic convergence of collocation methods," *Mathematics of Computation*, vol. 41, no. 164, pp. 349–381, 1983.

[130] G. Muldowney and J. J. Higdon, "A spectral boundary element approach to three-dimensional stokes flow," *Journal of Fluid Mechanics*, vol. 298, pp. 167–192, 1995.

[131] C. Pozrikidis, "A spectral-element method for particulate stokes flow," *Journal of Computational Physics*, vol. 156, no. 2, pp. 360–381, 1999.

[132] L. Heltai, M. Arroyo, and A. DeSimone, "Nonsingular isogeometric boundary element method for stokes flows in 3d," *Computer Methods in Applied Mechanics and Engineering*, vol. 268, pp. 514–539, 2014.

[133] G. Beer, B. Marussig, and C. Duenser, *The Isogeometric Boundary Element Method*. Springer, 2020.

[134] K. Ata and M. Sahin, "An integral equation approach for the solution of the stokes flow with hermite surfaces," *Engineering Analysis with Boundary Elements*, vol. 96, pp. 14–22, 2018.

[135] M. Ingber and A. Mammoli, "A comparison of integral formulations for the analysis of low reynolds number flows," *Engineering analysis with boundary elements*, vol. 23, no. 4, pp. 307–315, 1999.

[136] M. S. Ingber and A. K. Mitra, "Grid optimization for the boundary element method," *International journal for numerical methods in engineering*, vol. 23, no. 11, pp. 2121–2136, 1986.

[137] C. Y. Chan, A. N. Beris, and S. G. Advani, "Second-order boundary element method calculations of hydrodynamic interactions between particles in close proximity," *International journal for numerical methods in fluids*, vol. 14, no. 9, pp. 1063–1086, 1992.

[138] H. Power and G. Miranda, "Second kind integral equation formulation of stokes' flows past a particle of arbitrary shape," *SIAM Journal on Applied Mathematics*, vol. 47, no. 4, pp. 689–698, 1987.

[139] F.-K. Hebeker, "Efficient boundary element methods for three-dimensional exterior viscous flows," *Numerical Methods for Partial Differential Equations*, vol. 2, no. 4, pp. 273–297, 1986.

[140] S. Kim and P. Arunachalam, "The general solution for an ellipsoid in low-reynolds-number flow," *Journal of Fluid Mechanics*, vol. 178, pp. 535–547, 1987.

[141] S. Wang, C. P. Martin, and S. Kim, "Improper integrals as a puzzle for creeping flow around an ellipsoid," *Physics of Fluids*, vol. 31, no. 2, p. 021 101, 2019.

[142] S. Wang, C.-W. Tai, and V. Narsimhan, "Dynamics of spheroids in an unbound quadratic flow of a general second-order fluid," *Physics of Fluids*, vol. 32, no. 11, p. 113 106, 2020.

[143] C. Pozrikidis, *A practical guide to boundary element methods with the software library BEMLIB*. CRC Press, 2002.

[144] D. Bommes, B. Lévy, N. Pietroni, C. Silva, M. Tarini, and D. Zorin, "State of the art in quad meshing," *Computer Graphics Forum*, 2012.

[145] P. Ning and J. Bloomenthal, "An evaluation of implicit surface tilers," *IEEE Computer Graphics and Applications*, vol. 13, no. 6, pp. 33–41, 1993.

[146] P. G. Ciarlet, *The finite element method for elliptic problems*. SIAM, 2002.

[147] S. Amini and S. M. Kirkup, "Solution of helmholtz equation in the exterior domain by elementary boundary integral methods," *Journal of Computational Physics*, vol. 118, no. 2, pp. 208–221, 1995.

[148] P. Juhl, "A note on the convergence of the direct collocation boundary element method," *Journal of Sound and Vibration*, vol. 212, no. 4, pp. 703–719, 1998.

[149] D. Pantazatos and R. MacDonald, "Directly observed membrane fusion between oppositely charged phospholipid bilayers," *The Journal of membrane biology*, vol. 170, no. 1, pp. 27–38, 1999.

[150] S. Svetina, "Vesicle budding and the origin of cellular life," *ChemPhysChem*, vol. 10, no. 16, pp. 2769–2776, 2009.

[151] E. Sezgin, I. Levental, S. Mayor, and C. Eggeling, "The mystery of membrane organization: Composition, regulation and roles of lipid rafts," *Nature reviews Molecular cell biology*, vol. 18, no. 6, pp. 361–374, 2017.

[152] S. L. Veatch and S. L. Keller, "Separation of liquid phases in giant vesicles of ternary mixtures of phospholipids and cholesterol," *Biophysical journal*, vol. 85, no. 5, pp. 3074–3083, 2003.

[153] F. Jülicher and R. Lipowsky, "Shape transformations of vesicles with intramembrane domains," *Physical Review E*, vol. 53, no. 3, p. 2670, 1996.

[154] T. Baumgart, S. T. Hess, and W. W. Webb, "Imaging coexisting fluid domains in biomembrane models coupling curvature and line tension," *Nature*, vol. 425, no. 6960, pp. 821–824, 2003.

[155] P. Gera and D. Salac, "Modeling of multicomponent three-dimensional vesicles," *Computers & Fluids*, vol. 172, pp. 362–383, 2018.

[156] P. Gera, *Hydrodynamics of Multicomponent Vesicles*. State University of New York at Buffalo, 2017.